NTNU – Trondheim
Norwegian University of
Science and Technology

Blast Loaded Aluminium Plates

Experiments and numerical simulations

Hilde Olaug Stakvik Eide
Emil Arne Melby

Civil and Environmental Engineering
Submission date: June 2013
Supervisor: Tore Børvik, KT
Co-supervisor: Vegard Aune, KT

Norwegian University of Science and Technology
Department of Structural Engineering

Department of Structural Engineering
Faculty of Engineering Science and Technology
NTNU- Norwegian University of Science and Technology

ACCESSIBILITY

Open

MASTER THESIS 2013

SUBJECT AREA:	DATE:	NO. OF PAGES:
Mechanical Engineering	31.05.2013	12 + 107 + 19

TITLE:

Blast loaded aluminium plates
Eksplosjonslast på aluminiumsplater

BY:

Hilde Stakvik Eide and
Emil Arne Melby

SUMMARY:

This thesis is written at the Structural Impact Laboratory (SIMLab) in collaboration with the Norwegian Defence Estates Agency (NDEA).

Light and flexible protective constructions in aluminium could be subjected to a blast load. In this thesis this effect was studied through experiments and numerical simulations on aluminium plates of the type 1050A - H14. The effect of fragmentation was idealized with predrilled holes.

Numerical simulations in LS-DYNA were used to validate the load curves obtained from the experiments. The load curves were obtained through pressure transducers that were placed on ¼ of the aluminium plate, and the numerical analysis showed that these values were not representative for the loading that occurred on the entire plate. The aluminium plates penetrated by fragments showed similar capacity as the plates without diamond-shaped holes and slits.

Analysis with the finite element software IMPETUS Afea indicates that the geometry of the charge and the number of particles used in the simulation affects the magnitude of the blast load in a significant way.

Experiments with the gas gun at SIMLab shows excellent repeatability, but the pressure and impulse it caused did not emulate a real explosion. Thus, the experimental setup needs to be modified in order to get more insight into the problem.

RESPONSIBLE TEACHER: Tore Børvik

SUPERVISOR(S): Tore Børvik and Vegard Aune

CARRIED OUT AT: Norwegian University of Science and Technology (NTNU)

Institutt for konstruksjonsteknikk

FAKULTET FOR INGENIØRVITENSKAP OG TEKNOLOGI

NTNU – Norges teknisk-naturvitenskapelige universitet

MASTEROPPGAVE 2013

for

Hilde Stakvik Eide og Emil Arne Melby

Eksplosjonslast på aluminiumsplater

Blast loaded aluminium plates

Lette og fleksible beskyttelseskonstruksjoner i aluminium kan utsettes for eksplosjonslast og/eller en kombinasjon av fragment- og eksplosjonslast. I denne masteroppgaven skal dette studeres gjennom eksperimentelle forsøk og numeriske beregninger. Her vil fragment-belastningen være idealisert som en påført skade i form av maskinerte hull, mens eksplosjonslasten vil frambringes ved hjelp av en trykkluftskanon. Hovedformålet med studiet er å undersøke når man må ta hensyn til interaksjonseffekten av kombinerte laster i design og om den kombinerte lasten vil medfører ytterligere oppsprekking av beskyttelsen. Oppgaven vil i grove trekk bestå av et litteraturstudium, deltagelse på forsøk og behandling av data, samt numerisk simulering og validering av forsøkene med elementmetoden.

Oppgaven skal inneholde følgende aktiviteter:

1. Litteraturstudium: Eksplosjonslast; penetrasjon og perforering av metalliske materialer; fragmentering, ulike numeriske metoder og modeller; material- og bruddmodeller.
2. Laboratorieforsøk: en gasskanon ved SIMLab skal benyttes for å teste 1050A-H14 aluminiumsplater (både med og uten skade) mot simulert eksplosjonstrykk. Forsøkene skal instrumenteres så godt som mulig, og senere brukes til validering.
3. Materialforsøk: nødvendige materialdata fra egne eller andres materialforsøk skal framskaffes mtp kalibrering av egnet materialmodell for FE analyser.
4. Numeriske analyser: Ikke-lineære analyser av forsøkene skal utføres ved bruk av ulike numeriske metoder og forskjellige metoder for å simulere brudd skal sammenlignes.
5. Validering og rapportering: Simuleringene skal valideres mot forsøksdata.

Besvarelsen organiseres i henhold til gjeldende retningslinjer.
Veileder(e): Tore Børvik og Vegard Aune
Besvarelsen skal leveres til Institutt for konstruksjonsteknikk innen 14. juni 2013.
NTNU, 14. januar, 2013

Tore Børvik, faglærer

Acknowledgements

This thesis was written at the Structural Impact Laboratory (SIMLab) in collaboration with the Norwegian Defence Estates Agency (NDEA). SIMLab is located at the Department of Structural Engineering at the Norwegian University of Science and Technology (NTNU) and is a Centre for Research-based Innovation (CRI). SIMLab works on developing tools and numerical methods for product development of structures and material exposed to impact and explosions. Its partners include Hydro Aluminium, Statoil, SSAB Swedish steel, SINTEF, NDEA, Benteler Aluminum Systems, BMW and Audi.

The work on this thesis has been both challenging and educational. The opportunity to use the knowledge we have acquired during our time at NTNU on an exciting field has been a great experience. We have had the opportunity to both use advanced finite element software and perform relevant experiments ourselves.

We would like to thank our supervisor Professor Tore Børvik and PhDc Vegard Aune for their guidance and invaluable input on this thesis. They have contributed with weekly guidance and discussions. Additionally we would like to thank Egil Fagerholt, Dr.ing., for his guidance and help with DIC.

Special thanks are given to Lars Olovsson, Dr.ing., at IMPETUS Afea for his seminar on the IMPETUS Afea Solver and the Corpuscular method. He has also contributed with great insight on numerical problems and troubleshooting. Also, thanks are given to Trond Auestad from NTNU and Knut Ove Hauge from NDEA for assisting in setting up the experiments. We also appreciate the support given from Researcher David Morin regarding programming in Matlab.

Trondheim 05.06.2013

_____ _____

Emil Arne Melby Hilde Stakvik Eide

Abstract

Light and flexible protective constructions in aluminium could be subjected to a blast load. In this thesis the effect of blast loading on aluminium plates of the type 1050A – H14 was studied through experiments and numerical simulations. The effect of fragmentation was idealized with predrilled holes. The thesis was written at the Structural Impact Laboratory (SIMLab) at NTNU in collaboration with the Norwegian Defence Estates Agency (NDEA).

Tensile tests revealed a clearly anisotropic behavior of the 1050A – H14 material. However, preliminary studies indicated that the grain direction had a minimal impact on the plate deformation, and that the modified Johnson-Cook material model was a sufficient approach.

It was performed experiments with the gas gun at SIMLab to apply blast loading on aluminium plates. The gas gun showed excellent repeatability, but the pressure and impulse it caused did not emulate a real explosion. It seemed that the loading applied from the gas gun was asymmetric and varied over the plate. Thus, the experimental setup needs to be modified in order to get more insight into the problem. No fracture occurred in the gas gun experiments.

Numerical simulations in LS-DYNA were used to validate the load curves obtained from the experiments. The load curves was obtained through pressure transducers that were placed on ¼ of the aluminium plate, and the numerical analysis showed that these values were not representative for the loading that occurred on the entire plate. The aluminium plates with diamond shaped holes and slits showed similar capacity as the plates without holes for small loads. Digital Image Correlation (DIC) was used to describe the plate deformation, and proved to be an accurate method to compare the results from the numerical simulation in LS-DYNA to the gas gun experiments. Numerical analyses with the finite element software IMPETUS Afea was used to simulate blast loading with the use of the Corpuscular method. The results indicated that the geometry of the charge affected the magnitude of the blast load in a significant way. IMPETUS Afea seems to be not suited to simulate long-range blast loading.

Sammendrag

Lette og fleksible beskyttelseskonstruksjoner i aluminium kan utsettes for eksplosjonslast og/eller en kombinasjon av fragment- og eksplosjonslast. I denne avhandlingen ble det undersøkt, ved bruk av eksperimenter og numeriske simuleringer, hvilken effekt eksplosjonslast har på aluminiumsplater av typen 1050A - H14. Effekten av fragmentering ble idealisert som en påført skade i form av maskinerte hull. Avhandlingen er skrevet på Structural Impact Laboratory (SIMLab) ved NTNU i samarbeid med Forsvarsbygg (NDEA).

Strekktester gjennomført på materialet 1050A - H14 viste at materialet hadde en klar anisotrop oppførsel. Innledende studier viste derimot at fiberretningen hadde en minimal effekt på platedeformasjonen, og at den modifiserte Johnson-Cook materialmodellen kunne benyttes.

Det ble utført eksperimenter ved bruk av gasskanonen på SIMLab for å påføre eksplosjonslast på aluminiumsplater. Gasskanonen viste seg å være repeterbar, men trykk og impuls viste seg å ikke samsvare med en ekte eksplosjon. Lasten fra gasskanonen varierte over platen, og det virket som trykket ikke traff senter på platen. For å få ytterligere innsikt i problemet må antakeligvis det eksperimentelle oppsettet endres. Brudd ble ikke observert i noen eksperimentelle tester.

Numeriske simuleringer i LS-DYNA ble gjennomført for å etter-regne lastkurvene fra gasskanon-forsøkene. Lastkurven ble registrert gjennom trykkmålere som ble plassert på ¼ av aluminiumsplaten. Den numeriske analysen viste at disse verdiene ikke var representative for lastsituasjonen på hele platen. Aluminiumsplater med diamantformede hull og slisser hadde, ved små belastninger, tilsvarende kapasitet som platene uten hull. Digital Image Correlation (DIC) ble brukt til å registrere og beskrive platedeformasjonen, og viste seg å være en god metode for å sammenligne resultatene fra den numeriske simuleringen i LS-DYNA med gasskanon-eksperimentene. Numeriske analyser ble også gjennomført i IMPETUS Afea for å simulere eksplosjonslast ved bruk av en partikkelbasert metode. Resultatene viste blant annet at geometrien på den eksplosive ladningen hadde stor betydning på omfanget av eksplosjonslasten. IMPETUS Afea har vist seg å være uegnet til å simulere eksplosjonslast over lange avstander, men er adskillig bedre til å simulere eksplosjonslast over korte avstander.

Contents

1 Introduction and earlier work

Blast protection is an area that is highly relevant in many parts of modern infrastructure. Both military and civilian applications are prominent. Traditionally, concrete has been used as a blast protective structure. But concrete is heavy and unwieldy, so for non-stationary objects a more lightweight material is more suitable. Much work has been done on concrete in the past [1], but less work has been performed on lightweight materials such as aluminium and steel.

In this thesis, blast protection of thin aluminium plates is investigated. Although there is a synergetic effect of blast loading and fragments, the main weight of the experiments were conducted on plates without holes. The experiments were carried out on eight aluminium plates at the SIMLab laboratory at NTNU using a gas gun described in chapter 5 with different magnitude of loading. The results are presented herein. Digital Image Correlation (DIC) was used to capture the results. In addition to the experiments, finite element analyses were carried out in LS-DYNA and IMPETUS Afea to investigate the usefulness of different methods of blast load simulations. A trustworthy blast simulation method is needed to greatly decrease the cost of designing protective structures. A Lagrangian approach will be used. In IMPETUS Afea the emphasis will be placed on the Corpuscular method.

There have been several research articles and master thesis dealing with numerical methods of simulating blast loading, and a brief summary of earlier works done at SIMLab will be presented here:

The master thesis *Combined blast and fragment loading on plates* by Rakvåg [2] investigates the synergetic effects of blast loading and fragmentation using Arbitrary Lagrangian Eulerian analysis. He concludes that plates penetrated by fragments have a lower capacity when regarding blast loading. He also informs that this is neglected in design codes, such as TM 5-885-1 [3].

In the article *A particle-based approach to close range blast loading* by Olovsson et al. [4], a new approach to describe blast loading is suggested. This approach is referred to as the Corpuscular method. In this method the detonation products are modeled as a set of discrete particles following Maxwell kinetic molecular theory. The pressure loading on structures are represented as momentum transfer as particles impact the surface of the structure. This

method is less computational expensive compared to ALE simulation and it is numerical robust. This particle-based approach is used in the finite element program IMPETUS Afea.

The article *Response of structures to planar blast load – A finite element engineering approach* by Børvik [5] compares an experiment with 4000 kg of TNT at a standoff distance of 120m to numerical analyses. For this comparison three different methods were used: pure Lagrangian, coupled and uncoupled Eulerian – Lagrangian. The conclusion of the article is that structural flexibility reduces pressure loads from rigid references. This means that if the combination of loads and impulse are applied from ConWep [6] or similar blast calculators, the design will be conservative.

The following work has been carried out in this thesis to investigate the blast resistance of aluminium plates:

Chapter 2: Relevant theory of blast waves and their effects is presented, along with the numerical methods and theory behind the softwares being used in this thesis.
Chapter 3: A presentation of the material parameters and the material model that is being used.
Chapter 4: A preliminary study in which the numerical model is calibrated
Chapter 5: Experiments with the aluminium plates subjected to blast loading at SIMLab laboratories.
Chapter 6: Numerical analyses with LS-DYNA.
Chapter 7: Numerical analyses with IMPETUS Afea.

2 Theory

This chapter contains the theory relevant to the blast loading that occurs in this study. It also explains the difference between the Lagrangian and the Corpuscular method used in LS-DYNA and IMPETUS Afea. Furthermore there is included a recapitulation of the integration methods and equilibrium equations used for the numerical simulations.

2.1 Explosion

An explosion is often defined as a rapid increase in volume and release of energy in an extreme matter, usually with the generation of high temperatures and the release of gasses [7]. In nature most explosions arise from various volcanic processes, but in engineering context it is often used with chemical materials like TNT and dynamite.

Smith [8] divides explosions into three categories: physical, chemical and nuclear. Examples of a physical explosion include mixing two liquids at different temperatures or the failure of a cylinder containing compressed gas. In a nuclear explosion the released energy comes from the redistribution of protons and neutrons within the reacting substance. There are two types of nuclear reactions that has the capability to produce explosions, and that is fission and fusion. A chemical explosion comes from rapid oxidation of fuel elements and is called combustion. The oxygen needed for this reaction can also be found within the explosive compound, so air is not necessary.

What differentiates an explosive reaction from an ordinary combustion, like the burning of wood, is the speed of the reaction. The rapid release of heat will cause the gasses that are released from the explosive reaction to generate high pressure and expand. This is defined as the shock wave [9]. Additionally, explosions from charges of the same compound, weight and geometry do not necessarily give the same pressure and impulse characteristics [10].

Explosions can cause different effects that pose a threat to nearby structures, i.e. shock wave, fragmentation, thermal effects, cratering and ground shock. This thesis will focus mainly on the shock wave, but effects of fragmentation will also be examined.

2.1.1 Shock wave

A shock wave is a type of propagating disturbance. It has similarities to an ordinary wave in that it carries energy and can propagate through a medium [11]. The shock wave has an extremely short rise in pressure, temperature and density [12]. The blast wave from an explosion might not be a shock wave to begin with, but as the blast wave propagates away from the source it will "shock up". This means that the air is compressed at the front of the blast wave. The resulting shock wave moves faster than the speed of sound [13]. When a condensed high explosive material is detonated, almost 100% of the energy released is converted into a blast wave [8]. With a nuclear explosion only 50% of the energy is converted into a blast wave, the rest goes to thermal and other types of radiation [8].

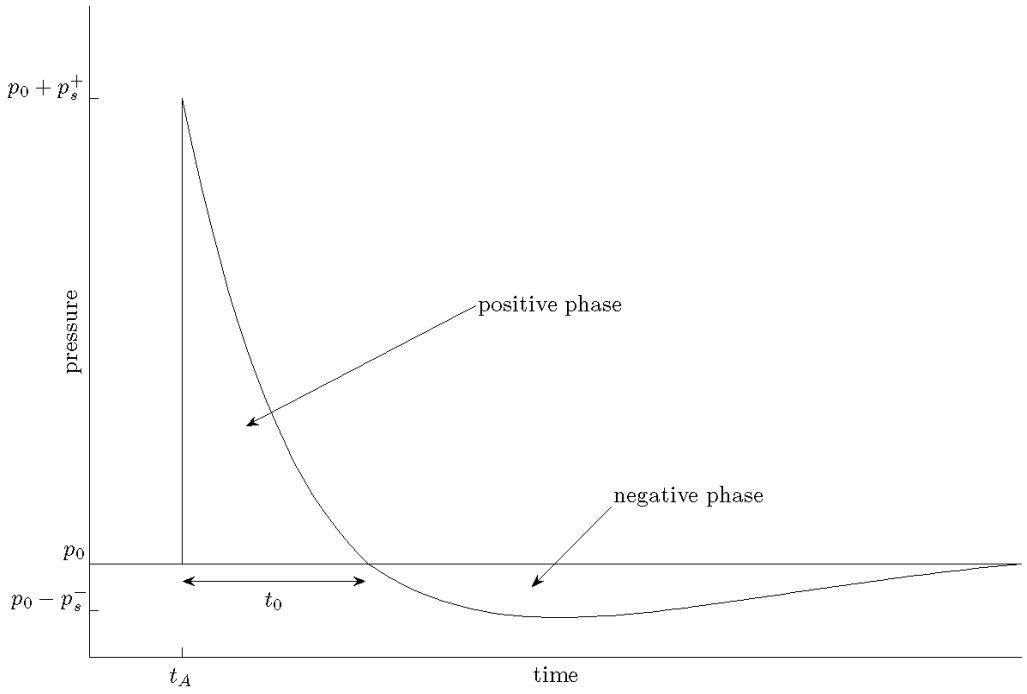

Figure 1: Ideal shock wave

An ideal shock wave, as seen in Figure 1, has a spherical source and takes place in a still homogeneous atmosphere. The shock wave has a rapid loading curve from the ambient pressure p_0 to the peak pressure $p_0 + P_s^+$ at the arrival time t_a. This is known as the

hydrostatic pressure, or the *Side-on* pressure. The pressure is called Side-on because it acts on a plane parallel to the direction of the shock wave. The Side-on pressure does not include the dynamic pressure. The pressure drops to the ambient pressure and then continues to drop beneath the ambient pressure, creating a negative phase. The negative phase is often neglected in pressure calculations, while the positive phase is described by the modified Friedlander equation [13]:

$$p(t) = p_0 + P_s^+(1-\frac{t}{t^+})e^{(-b\frac{t}{t^+})} \quad (2.1)$$

Where:
- $p(t)$: Overpressure
- p_0: Ambient pressure
- P_s^+: Peak hydrostatic overpressure
- t: Time, measured from arrival time of shock wave
- t^+: Length of positive phase
- b: Decay parameter

The dynamic pressure can be expressed as a function of the peak hydrostatic overpressure [14]:

$$q = \frac{P_s^{+2}}{2\gamma p_0 + (\gamma-1)P_s^+} \quad (2.2)$$

Where:
- q : Peak dynamic pressure
- $\gamma = \frac{C_p}{C_v}$
- C_p: Heat capacity at constant pressure
- C_v: Heat capacity at constant volume
- γ : Ratio between the heat capacity at constant pressure and the heat capacity at constant volume

It can also be expressed as a function of particle velocity u, and density ρ of the particles.

$$q = \frac{\rho u^2}{2} \quad (2.3)$$

The impulse i_s from the shock wave is calculated as an integration of the hydrostatic overpressure [15]:

$$i_s = \int_{t_A}^{t_A+t_0} p(t)dt \tag{2.4}$$

Another force that acts on a structure subjected to a shock wave is the reflected pressure. When a shock wave hits a structure, a pressure that is higher than the Side-on pressure occurs, as seen in Figure 2. This can be compared to when a wave of water hits the shore and splashes up. The initial water level is the hydrostatic pressure, and the wave is the reflected pressure. For an ideal gas the relationship between reflected pressure P_r, and the peak hydrostatic pressure P_s, could be described as [14]:

$$P_r = 2P_s + \frac{(\gamma+1)P_s{}^2}{(\gamma-1)P_s+2\gamma p_0} \tag{2.5}$$

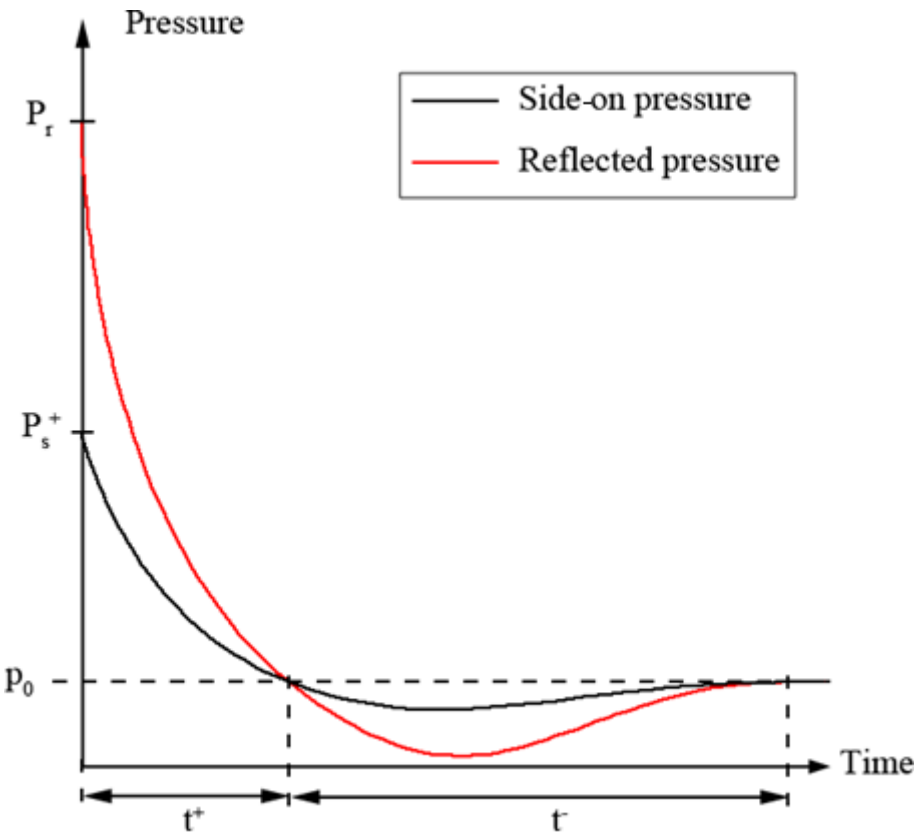

Figure 2: Reflected and Side-on pressure

The forces that act on a structure from a shock wave can then be summed up to be:

- Force from the hydrostatic pressure p
- Force from the dynamic pressure q
- Force from the reflected pressure P_r

2.1.2: Fluid Structure Interaction

The equations and methods used to calculate hydrostatic and reflected pressure in chapter 2.1.1 only holds true if the structure the pressure-wave hits is rigid. If it is taken into account that the structure is deformable and may breach, the impulse on the structure may be lower than if it were rigid [16]. In this thesis the aluminium plates will deform when the shock wave hits, leading to a lower impulse than that of a rigid wall. This happens because the plate acquires velocity which reduces the pressure that acts on the plate.

2.1.3. Failure modes

For clamped plates subjected to blast load there are three failure modes defined [17]:

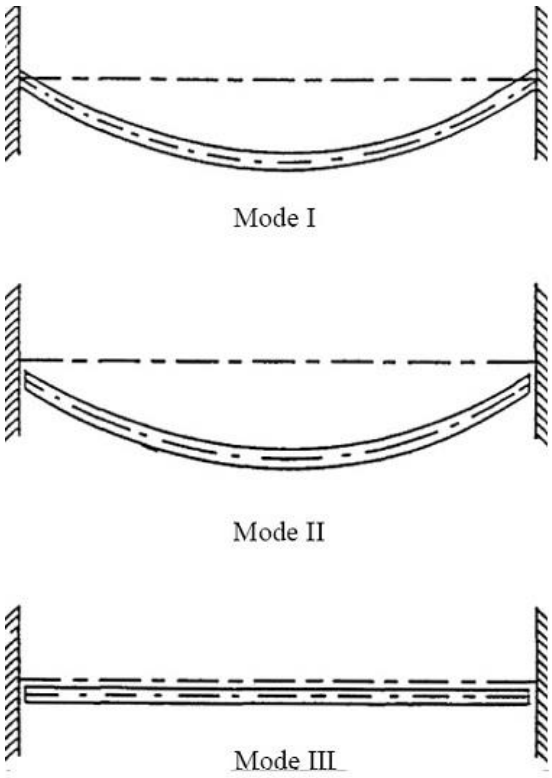

Figure 3: Failure modes for clamped plates subjected to blast load

The failure modes shown in Figure 3 are described as:

- Mode I: Large ductile deformation
- Mode II*: Partial tensile tearing
- Mode IIa: Complete tensile tearing with increasing deformation
- Mode IIb: Complete tensile tearing with decreasing deformation
- Mode III: Transverse shear

were mode II has several sub-modes.

The first mode occurs with the lowest impulse and the others occur in turn with rising impulse.

2.1.4 Fragments

When an explosion occurs it will often accelerate surrounding objects, like rock or tools. These objects are then known as fragments. Fragments can be divided into two categories: primary and secondary [18].

The primary fragments are fragments from the casing of the explosive, i.e. a metal container with TNT inside. These types of fragments could be seen as deliberate. The casings of explosives are often designed so that it shatters into many small pieces, with the exception of casings containing gaseous or liquid explosives which generate larger fragments.

The secondary fragments are created when the shock wave hits nearby objects, like rocks or debris. The shock wave could also tear secondary fragments of buildings.

The fragments could damage nearby buildings in several ways [19]:

- Perforation
- Embedment
- Ricochet

Perforation is when the fragment penetrates and passes through the object, embedment is when the fragment is stopped by the object and is stuck in it and ricochet is when the fragment is deflected by the object and continues in another direction.

The size and distribution of the fragments can be calculated by these formulas [20]:

$$N = \frac{1}{\pi S^3} \tag{2.7}$$

$$\frac{N_g(W)}{N} = e^{-\frac{W}{S}} \tag{2.8}$$

$$\frac{N_g(n)}{N} = \beta^{n-1} \tag{2.9}$$

Where	N:	Total number of fragments per unit volume
	$N_g(W)$:	Number of fragments per unit volume with width <W
	$N_g(n)$:	Number of fragments per unit volume with aspect ratio<n
	β:	Material dependent geometrical factor
	n:	Fragment aspect ratio
	S:	Strain rate and material property characteristic strip width
	W:	Width of the fragment strip

2.2 Numerical methods

LS-DYNA and IMPETUS Afea are both advanced general-purpose finite element codes and simulation software packages, able to do highly nonlinear dynamic finite element analyses. The solution methods in LS-DYNA and IMPETUS Afea are mainly based on explicit time integration, presented in the sub-section below [21][22].

Blast loading is a non-linear, dynamic problem, and in this thesis the Lagrangian approach is chosen. The Corpuscular method used in IMPETUS Afea is also described.

All out of the plane deformations are registered and measured with the Digital Image Correlation (DIC) software, which is a numerical post-processing program for images recorded in mechanical experiments using finite element equations [23].

2.2.1 Explicit time integration

Direct integration methods calculate the response history of the model by using a number of integration steps in time, separated by time increments Δt. The displacements may be evaluated for each time step. At the *n*th time step for a multi degree of freedom system, the equation of motion may be written as [24]:

$$[\mathbf{M}]\{\ddot{\mathbf{D}}\}_n + [\mathbf{C}]\{\dot{\mathbf{D}}\}_n + \{\mathbf{R^{int}}\}_n = \{\mathbf{R^{ext}}\}_n \quad (2.10)$$

Where:
- $[\mathbf{M}]$: Mass matrix
- $[\mathbf{C}]$: Damping matrix
- $\{\mathbf{R^{int}}\}$: Internal forces vector = $[\mathbf{K}]\{\mathbf{D}\}$ for a linear problem, where $[\mathbf{K}]$ is the stiffness matrix
- $\{\mathbf{D}\}$: Nodal degree of freedom
- $\{\dot{\mathbf{D}}\}$: Nodal point velocity
- $\{\ddot{\mathbf{D}}\}$: Nodal point acceleration

The difference expression of an explicit algorithm uses the general form [24]:

$$\{\mathbf{D}\}_{n+1} = f(\{\mathbf{D}\}_n, \{\dot{\mathbf{D}}\}_n, \{\ddot{\mathbf{D}}\}_n, \{\mathbf{D}\}_{n-1}, \dots) \tag{2.11}$$

The quantities on the right hand side of the equation are known values, and no equation solving is necessary. Equilibrium iterations are not necessary since convergence is not an issue. This means that the explicit equation solving is computationally inexpensive compared to implicit equation solving, since unknown values are obtained from information already known [25].

The principle of explicit time integration is shown in Figure 4 [26]:

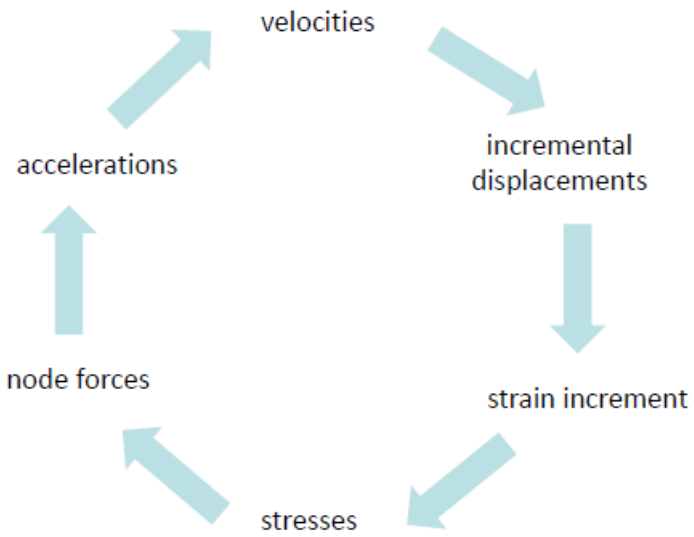

Figure 4: Explicit time integration loop.

The explicit integration method is conditionally stable, and requires that a minimum "critical" time step Δt_{cr} is not exceeded. Δt_{cr} is the minimum time a dilatational wave takes to travel across any element in the model. If the time step Δt, is larger than the distance between two adjacent nodes in an element, information may be lost and the calculations may become unstable and "blow up" [25].

$$\Delta t \leq \frac{2}{w_{max}} = \frac{L^e}{c} = \Delta t_{cr} \tag{2.12}$$

Where: w_{max}: Maximum natural frequency

L^e: Element length

c: Dilatational wave speed in the material

For a damped equation of motion Δt is described as [25]:

$$\Delta t \leq \frac{2}{w_{max}}\left(\sqrt{1+\xi^2}-\xi\right) \tag{2.13}$$

Where: ξ: Damping ratio

Since Δt_{cr} is quite small, the method requires many time steps, but by employing diagonal (lumped) mass and damping matrixes, each time step is executed quickly. The explicit method also requires less computer storage than an implicit method, and is the most efficient method for discontinuous nonlinearities, e.g. contact, buckling, failure etc. In blast and penetration problems where higher order modes dominate, and the total time span is in order of milliseconds, the explicit time integration is a preferred method [25].

2.2.2 Central Difference Method

LS-DYNA uses a modified version of the Central Difference Method to integrate the equations of motion [27]. The conventional Central Difference expressions are as follows [24]:

$$\left\{\dot{\mathbf{D}}\right\}_n = \frac{1}{2\Delta t}\left(\{\mathbf{D}\}_{n+1} - \{\mathbf{D}\}_{n-1}\right) \tag{2.14}$$

$$\left\{\ddot{\mathbf{D}}\right\}_n = \frac{1}{\Delta t^2}\left(\{\mathbf{D}\}_{n+1} - 2\{\mathbf{D}\}_n + \{\mathbf{D}\}_{n-1}\right) \tag{2.15}$$

Both equations are the result of subtracting or adding the Taylor series expansion of $\{\mathbf{D}\}_{n+1}$ and $\{\mathbf{D}\}_{n-1}$, neglecting higher order terms containing Δt to power higher than second order. The error is therefore proportional with Δt^2, which means that halving the time step should approximately quarter the error. A small Δt ensures adequate accuracy and is required for computationally stability. Combining the two equations (2.14) and (2.15) with the equation of motion, we get an expression of $\{\mathbf{D}\}_{n+1}$ [24]:

$$\left[\frac{1}{\Delta t^2}\mathbf{M}+\frac{1}{2\Delta t}\mathbf{C}\right]\{\mathbf{D}\}_{n+1}=\{\mathbf{R^{ext}}\}_n-\{\mathbf{R^{int}}\}_n+\frac{2}{\Delta t^2}[\mathbf{M}]\{\mathbf{D}\}_n-\left[\frac{1}{\Delta t^2}\mathbf{M}-\frac{1}{2\Delta t}\mathbf{C}\right]\{\mathbf{D}\}_{n-1} \quad (2.16)$$

The modified version of the Central Difference Method used in LS-DYNA is a half-step method, shown in Figure 5, where the actual geometry **X**, is used instead of the displacements **D** [28].

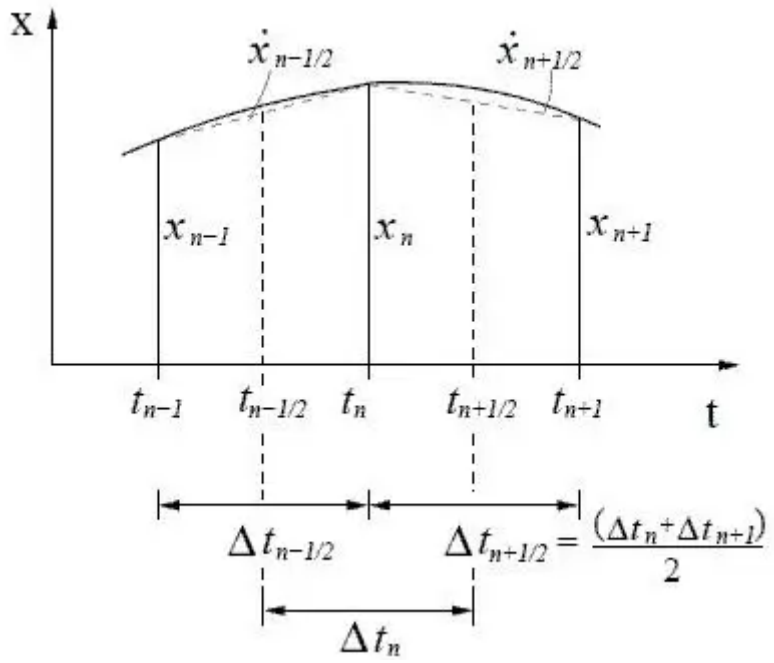

Figure 5: Half-step Central Difference Method

For the half-step method the difference expressions are [24]:

$$\{\dot{\mathbf{D}}\}_{n-1/2} = \frac{1}{\Delta t}\left(\{\mathbf{D}\}_n - \{\mathbf{D}\}_{n-1}\right) \tag{2.16}$$

$$\{\dot{\mathbf{D}}\}_{n+1/2} = \frac{1}{\Delta t}\left(\{\mathbf{D}\}_{n+1} - \{\mathbf{D}\}_n\right) \tag{2.17}$$

$$\{\ddot{\mathbf{D}}\}_n = \frac{1}{\Delta t}\left(\{\dot{\mathbf{D}}\}_{n+\frac{1}{2}} - \{\dot{\mathbf{D}}\}_{n-\frac{1}{2}}\right) = \frac{1}{\Delta t^2}\left(\{\mathbf{D}\}_{n+1} - 2\{\mathbf{D}\}_n + \{\dot{\mathbf{D}}\}_{n-1}\right) \tag{2.18}$$

For the equation of motion, when the velocity lagging by a half time step, the new expression for $\{\mathbf{D}\}_{n+1}$ is [24]:

$$\frac{1}{\Delta t^2}[\mathbf{M}]\{\mathbf{D}\}_{n+1} = \{\mathbf{R^{ext}}\}_n - \{\mathbf{R^{int}}\}_n + \frac{1}{\Delta t^2}[\mathbf{M}]\left(\{\mathbf{D}\}_n + \Delta t\{\dot{\mathbf{D}}\}_{n-\frac{1}{2}}\right) - [\mathbf{C}]\{\dot{\mathbf{D}}\}_{n-1/2} \tag{2.19}$$

It is evident that the first part of the expression is independent of damping. The stiffness matrix becomes diagonal which results in a less computational expensive calculation, but the method can only guarantee first order accuracy. In problems where light damping and small time steps are present, i.e. blast loading, the half-step method has about the same accuracy as the classical Central Difference Method [25].

2.2.3 Lagrangian FEA

The Lagrangian formulation is also known as the Material formulation, as the mesh moves and deforms with the material (Fig. 6). The nodes at the computational grid (mesh) are always at the same material point, and boundaries and interfaces remain coincident with element edges. Since the quadrature points move with the material, constitutive equations are evaluated at the same material point, and this is advantageous for history-dependent materials. Lagrangian meshes are therefore widely used in solid mechanics. A problem with the

Lagrangian formulation is related to large deformation, where the Lagrangian element may be similarly distorted. This may reduce the accuracy of the approximation, as the Jacobian determinants at quadrature points may become negative, resulting in negative mass and energy densities, causing problems for the calculation and its accuracy. Even though, the Lagrangian approach makes it a lot easier to model complex structures and contact conditions, as the constitutive equations are solved using material points [29].

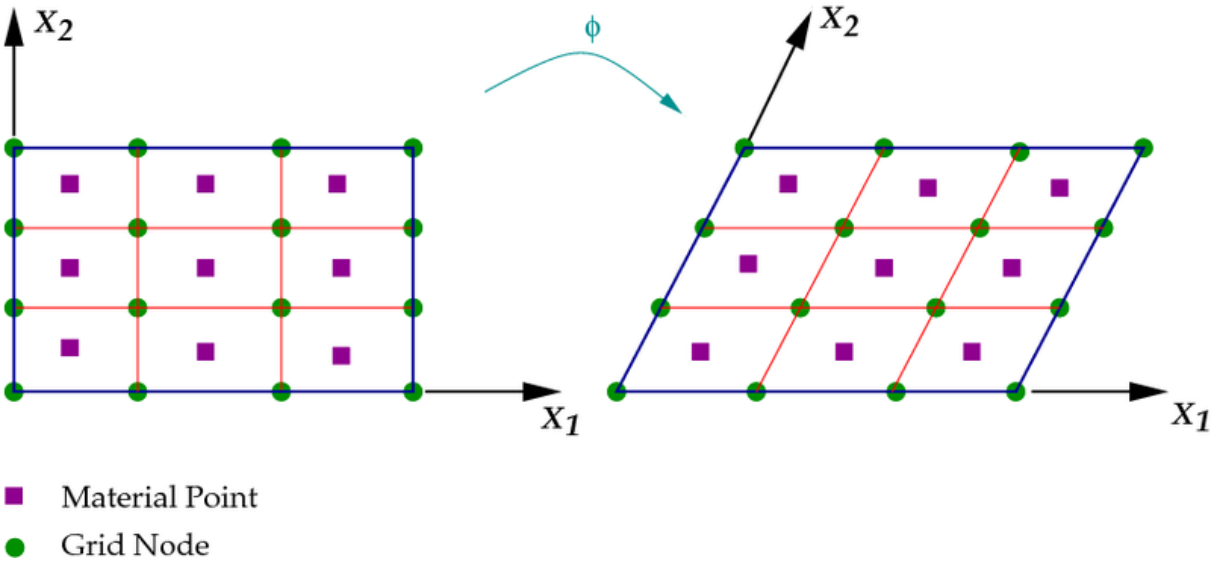

Figure 6: The Lagrangian formulation mesh [30].

2.2.4 Corpuscular method

The Corpuscular method for gas dynamics is originally developed for airbag deployment simulations in LS-DYNA. It is explained as a method of modeling gas molecules as rigid particles, to more easily describe a gas flow without using continuum formulations and by avoiding numerical difficulties concerning gas-fabric interactions. By using a purely Lagrangian approach, these contact treatments are simplified. The particle method is less computationally expensive, and a more robust approach compared to the Eulerian approaches. Studies have shown that the Corpuscular method is well suited to explain close-range blast loading compared to other methods [31][4].

The Corpuscular method is based on the kinetic molecular theory, derived by Maxwell in 1860, which is the study of gas molecules and their interaction [31]. Assumptions have to be made [4]:

- The molecules are viewed as rigid particles obeying Newton's laws of mechanics, where all interactions are perfectly elastic collisions.
- The distance between the molecules is large compared to the molecule size
- Molecules are in random motion
- Ideal gas behavior occurs

It is impossible to model every single molecule in a blast scenario, therefore each particle represent many molecules, typically 10^{15}-10^{20}. The pressure from a few large particles will give the same pressure as many small particles, since the pressure is an equation of the translational kinetic energy, as long as the root mean square velocity v_{rms}, is the same. For detonation products, one can expect a number of 10^{22}-10^{23} molecules for each gram, depending on the molecular weight. The radius of the particle has to be adjusted dynamically to obtain a reasonable mean-free path. A too small radius will give less ability to transfer pressure waves, while a too large radius makes the gas behavior deviate from the ideal gas law. All particles are assumed spherical, to simplify the contact condition [4].

The pressure *p*, is:

$$p = \frac{nMv_{rms}^2}{3V} = \frac{2W_k}{3V} = \frac{2}{3}w_k \tag{2.20}$$

Where:

n:	Number of molecules (mol)
M:	Molar mass
$v_{rms} = \sqrt{\frac{1}{N}\sum_{i=1}^{N}\lvert v_i\rvert^2}$:	Root mean square velocity
V:	Volume
W_k:	Total translational kinetic energy
w_k:	Total translational kinetic energy per unit volume

Combined with the ideal gas law $pV = nRT$, the expression for the root mean square velocity at thermal equilibrium becomes [4]:

$$v_{rms} = \sqrt{\frac{3RT}{M}} \tag{2.21}$$

Where: R: Universal gas constant

T: Temperature

w_k is a fraction $\xi(T)$of the specific internal energy *e*:

$$w_k = \xi e \tag{2.22}$$

Where: $$\xi = \frac{3}{2}\frac{c_p - c_v}{c_p} = \frac{3}{2}(\gamma - 1) \tag{2.23}$$

The theoretical upper limit for ξ is 1 and applies to mono-atomic gases which store 100 % of the internal energy as translational kinetic energy. For more complex molecules, more energy is stored as vibration and spin. In addition, ξ is never below 0, giving an upper and lower limit for γ:

$$1 < \gamma \leq \frac{5}{3} \tag{2.24}$$

Combining equation (2.20) and (2.23) a new expression for the pressure is established:

$$p = (\gamma - 1)e \tag{2.25}$$

To satisfy this equation (2.23) the spin and vibration energy of molecules in gases is just lumped to the particle, without assigning the particles any degrees of freedom [4].

In IMPETUS Afea, a velocity distribution function is needed to translate macroscopic properties, i.e. heat capacities, into particle data. With the assumption that the velocity distribution in different orthogonal directions is uncoupled, the Maxwell-Boltzmann distribution function of molecular velocity v, at thermal equilibrium is [31]:

$$f(|v|) = 4\pi \left(\frac{M}{2\pi RT}\right)^{\frac{3}{2}} |v|^2 exp\left(\frac{-M|v|^2}{2RT}\right) \tag{2.26}$$

2.2.5 LS-DYNA and IMPETUS Afea

Both LS-DYNA and IMPETUS Afea are nonlinear explicit finite element tools, capable of simulating large, real-world problems in 3D. IMPETUS Afea is exclusively based on volume elements, while LS-DYNA uses both shell - and volume elements. The Corpuscular method is implemented in LS-DYNA. The drawback of this method in LS-DYNA is that it might be noisy and diffusion is heavily exaggerated due to dispersion and the pressure waves are badly resolved [31]

The IMPETUS Afea code also implements the Corpuscular method in blast wave analyses. The IMPETUS Afea code is developed to predict large deformations of structures exposed to extreme loading conditions, without reducing the accuracy and the robustness [26].

In IMPETUS Afea only one contact condition is needed, and the finite element and contact calculation is carried out with double precision. In blast and penetration problems, the explicit time integration is an ideal method. IMPETUS Afea utilizes a unique higher order element technology, and the problem with spurious zero-energy modes is avoided [22].

Complex simulations with a huge amount of particles are CPU-expensive, but with the IMPETUS Afea code, the time of the analysis may be highly reduced, as the calculations are being carried out on the GPU [32].

2.2.6 Digital Image Correlation (DIC)

Digital Image Correlation (DIC) is a numerical post-processing algorithm for images recorded in mechanical experiments. The technique concerns the tracking of random patterns in series of digital images. By applying DIC, displacements in and out of the plane as well as strain fields may be measured. DIC has in the last decade become a well-established tool for measuring strain and displacements of a wide range of materials, due to its low-cost and easy-to-use features. Because of faster computational hardware and improved camera technology, i.e. increased recording and resolution rates, it is now possible to analyze large series of high-resolution images [23][33].

In this thesis, three-dimensional DIC is used to measure the out of plane deformations of aluminium plates subjected to blast load.

Digital images are in essence two-dimensional matrices, where each pixel is given a value, representing a specific color. In this study, 12-bits greyscale images were used, which means that each pixel is given a white-light intensity value ranging from 0 (black) to 4095 (white) [34].

By using a binocular stereovision system, consisting of two high-speed cameras, together with DIC, three-dimensional analyses are obtained. The principle is shown in Figure 7:

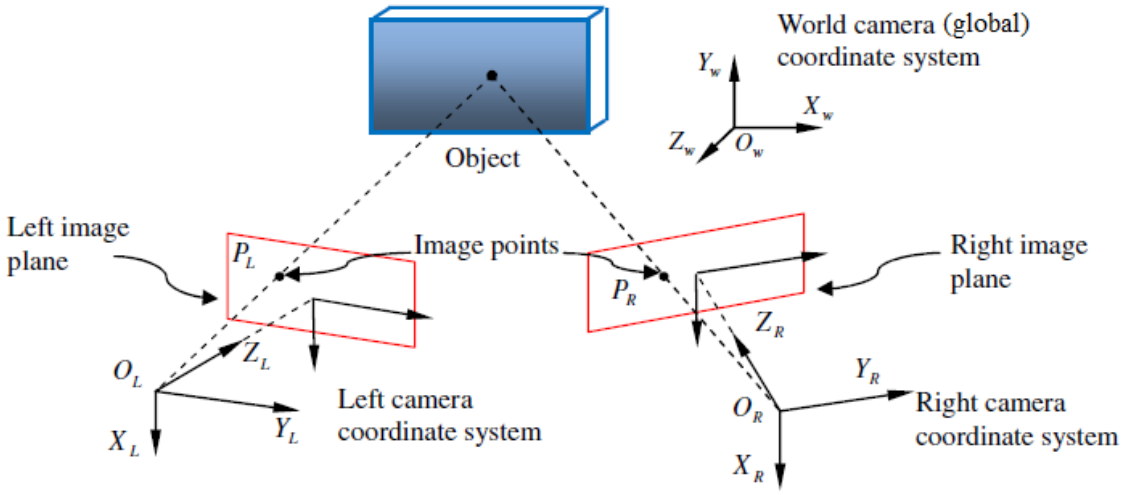

Figure 7: Principle sketch of 3D Digital Image Correlation (DIC) [35]

The DIC-approach requires high-speed cameras, which need to be calibrated prior to the experiments. A powerful light source is also preferable to light up the plate, for the cameras to be able to register the pattern correctly. Every recorded image during the experiment is capturing the geometry of the test specimen [23].

In the DIC-algorithm, the displacement is found by comparing an image of the specimen at current (deformed) state to an image of the specimen at a reference state (Fig. 8) [34].

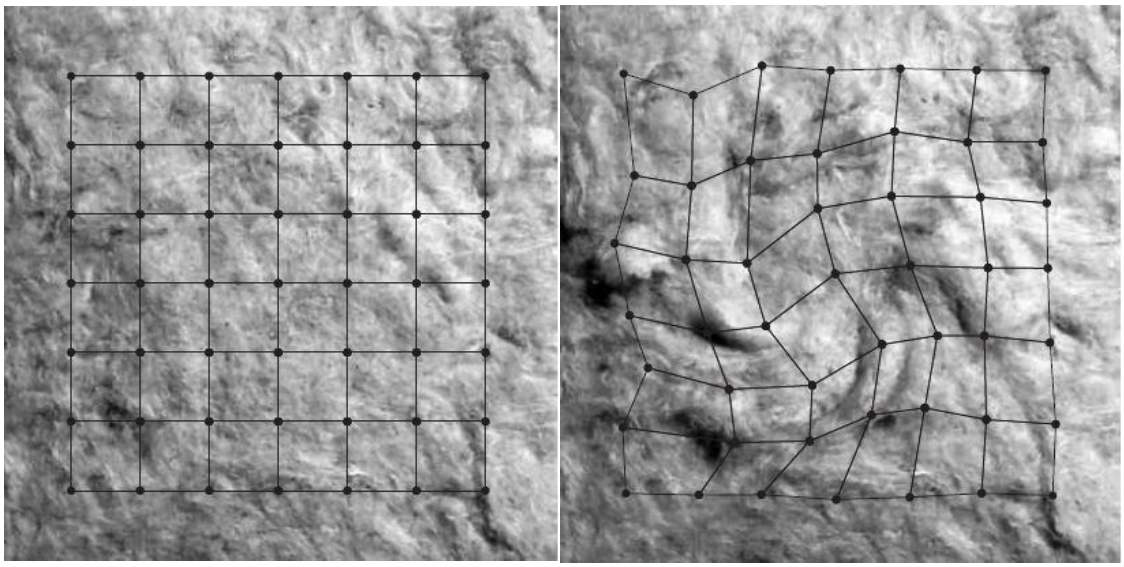

Figure 8: Finite element mesh in 2D – Left: Reference state. Right: Current (deformed) state [36]

The comparison of images can either be performed on a small subset of pixels containing the specific point of interest [37], or globally on a set of nodes contained in a "finite-element" mesh [38].

In this thesis the "finite-element" based DIC approach is being used. The nodal degrees of freedom in the mesh are optimized to minimize the difference in greyscale within the defined mesh [23].

The principle of the method is shown in Figure 9 [23]:

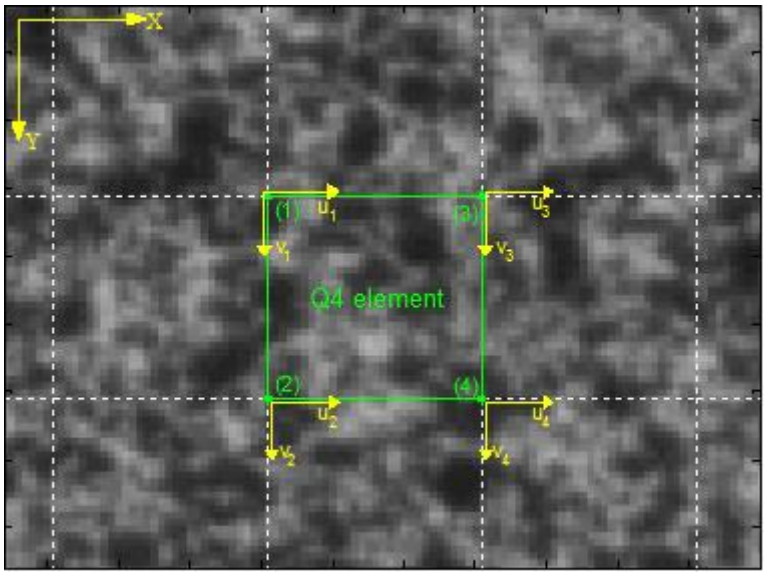

Figure 9: The nodes and the degrees of freedom (2D) of a Q4 element within a finite element mesh

The Q4 element shown in Figure 9 has four nodes, and in a 3D-analysis, when including the out of the plane displacements, the element has a total of 12 degrees of freedom. Each optimization parameter is subjected to measurement noise, which increases the measurement uncertainty, and should in general be kept at a minimum. For Q4 elements connected to neighboring elements within a "finite element" mesh, only three extra optimization parameters per element are required (one node), which reduces the number of optimization parameters [23].

In the "finite-element" method, the continuity of the displacement field across the element boundaries is preserved [23].

The displacement, described in a two-dimensional image coordinate system, may be written as a set of parameters [23]:

X=(X, Y) is the image coordinates in reference configuration
x=(x, y) is the image coordinates in the current configuration
u=**x**-**X** is the displacement in the 2D-image coordinate system

To establish the mathematical formulation of the "finite-element"-based DIC, the "conservation of optical flow" has to be assumed, i.e. [23]:

$$I_c = I_r \tag{2.27}$$

Where: I_c: Current (deformed) image
I_r: Reference image

The sum of squared greyscale differences between the current image and the reference image, integrated over a pixel region, is giving a correlation function *F* [23]:

$$F = \iint_{\Omega} [\Delta \boldsymbol{u} \cdot \boldsymbol{\nabla} I_r + I_c - I_r]^2 d\boldsymbol{X} \tag{2.28}$$

Where: Ω: Pixel region
$\Delta \boldsymbol{u}$: A small unknown displacement

The nodal displacements are found by iteratively solve a linear system of equations, i.e. equation (2.29). To obtain the accuracy of the solution, it is important that the known part of the displacement field $\boldsymbol{u}'$, is updated for each iteration. The global equation for an entire mesh of elements is defined as [23]:

$$\boldsymbol{M}\boldsymbol{a} = \boldsymbol{b} \tag{2.29}$$

Where: **M**: An assembly of all element contributions in $\boldsymbol{M}^e$

b: An assembly of all element contributions in $\boldsymbol{b}^e$

a: The value of $\Delta\boldsymbol{u}$ for all nodes in the mesh. After each iteration this is added to the value of $\boldsymbol{u}'$.

$$\boldsymbol{M}^e = \sum_{\Omega^e} N_m(\boldsymbol{X}) N_n(\boldsymbol{X}) \frac{\partial I_r(\boldsymbol{X})}{\partial X_\alpha} \frac{\partial I_r(\boldsymbol{X})}{\partial X_\beta} \tag{2.30}$$

$$\boldsymbol{b}^e = \sum_{\Omega^e} [I_r(\boldsymbol{X}) - I_c(\boldsymbol{x}')] N_m(\boldsymbol{X}) \frac{\partial I_r(\boldsymbol{X})}{\partial X_\alpha} \tag{2.31}$$

Where: $N_m(\boldsymbol{X}), N_n(\boldsymbol{X})$: Shape functions of the nodes with node numbers *m* and *n*

α, β: The coordinate axes

The global matrix **M** is sparse and symmetric, and this is exploited to make the calculations more efficient. Since **M** and **b** are assembled by element contribution, it is evident that a mesh containing a large number of elements will give a computationally expensive process. Since each node might be connected to several elements, and since the nodal contribution is the sum of the contribution from its connected neighbor elements, the assembly process has to be carried out in a serial manner. By assembling **M** and **b** from nodal contributions instead of element contribution, the process can be carried out in parallel [33].

When comparing a parallelized DIC-code to a serial DIC-code, the parallelized DIC-code was approximately five times as fast as the calculations of the serially implemented assembly of element contributions [39].

For a Q4-element, mapping from a normalized coordinate system (ξ,η) to the image coordinate system (X,Y) is given by [23]:

$$\boldsymbol{X} = \sum_{m=1}^{4} N_m(\xi, \eta)\boldsymbol{X}_m \tag{2.32}$$

Where: $\boldsymbol{X}_m$**:** Coordinates of the node *m*

This method makes it possible to apply any convex quadrilateral element shaped mesh, and to remove the rectangular shaped restriction on the Q4-element.

In the same way, the displacement of a random location $\boldsymbol{u}(\boldsymbol{X})$ inside an element is calculated as the weighted sum of the nodal displacements $\boldsymbol{u}_m$**,** when the weight factors are given by shape functions $N_m(\boldsymbol{X})$ [23]:

$$\boldsymbol{u}(\boldsymbol{X}) = \sum_m N_m(\boldsymbol{X})\boldsymbol{u}_m \tag{2.33}$$

A camera model is necessary to extract physical data from the image analyses, and to convert a two-dimensional image coordinate system into a three-dimensional coordinates in space. The camera model is a mathematical transformation model, and should convert the image coordinate system (u,v) (denoted in pixels), to the coordinate system (X,Y,Z) of the recorded test specimen (denoted in millimeters). The equations related to the 3D-camera model are described in detail by Fagerholt [40].

An advantage with the "finite-element"-based DIC is that the mesh easily can be adapted to fit complex specimen geometries. Another advantage is that the numerical techniques designed for the finite element method, such as mesh techniques and element shape functions, can directly be applied into the DIC algorithms [39].

A disadvantage of applying 3D-DIC, compared to 2D-DIC, is that it requires preparations in setup and calibration of the cameras. The image post-processing becomes also more extensive. However, 3D-DIC is required to register the out-of-plane measurements of the experiments in this thesis [39].

The success of the correlation is dependent on parameters such as the contrast and speckle size of the recorded grayscale pattern, element size, and the digitization level of the greyscale values. It is necessary that the element degrees of freedom are able to describe the

displacement field properly. Elements close to the boundaries of the mesh have larger measurement uncertainties than elements within the mesh, which may cause problems when dealing with discontinuous displacement fields, i.e. cracks [23].

To choose an ideal element size, it is necessary to find an appropriate compromise between small elements, which is more vulnerable to pixel noise, and large elements, which is less capable of describing the high gradient displacement fields [23]. In this thesis, an element size of 25x25 pixels was used.

2.3 Material model

When doing numerical simulations it is important to have a material model that correctly emulates the material behavior that occurs during the experiments. In this thesis the material model that is being used is the modified Johnson-Cook material model.

2.3.1 The modified Johnson and Cook material model

A material that is subjected to high strain rates and high temperature is described well by the Johnson-Cook material model [24]. In this thesis the material is subjected to both high and low velocity impact which can cause these material behaviors. The Johnson-Cook material model is developed for isotropic material behavior, but the material used in the experiments is assumed to show anisotropic behavior. However Grytten [41] suggests that low velocity impact and penetration problems can be reasonably well predicted using a simple isotropic material model, even though the material is anisotropic.

The equivalent stress σ_{eq}, in the original Johnson-Cook material model is expressed as:

$$\sigma_{eq} = [A + Bp^n]\left[1 + Cln\left(\frac{\dot{p}}{\dot{p}_0}\right)\right][1 - (T^*)^m] \qquad (2.34)$$

Where	*A, B, n, C* and *m*:	Material parameters
	p	Plastic strain
	$\dot{p}$:	Plastic strain rate
	$\dot{p}_0$:	Reference strain rate
	$T^* = (\frac{T-T_0}{T_m-T_0})$	
	T:	Temperature
	T_0:	Room temperature
	T_m:	Melting temperature

The equation consists of three parts that each accounts for a different physical phenomenon, in this case: Strain hardening, strain rate hardening and temperature softening.

To avoid the strain rate hardening term approaching minus infinity for small strain rates, the equation can be modified:

$$\sigma_{eq} = [A + B\rho^n]\left[1 + \left(\frac{\dot{\rho}}{\dot{\rho}_0}\right)\right]^C [1 - (T^*)^m] \tag{2.35}$$

This new equation is called the modified Johnson-Cook material model [24], and it accounts for: Von Mises yield criterion, the associated flow rule, linear thermo elasticity, non-linear isotropic strain hardening, strain rate hardening and temperature softening. Like the original Johnson-Cook material model the modified equation is developed for isotropic materials.

Different strain hardening models can be used with the Johnson-Cook material model, and in this thesis the extended Voce hardening rule is used [24]:

$$\sigma_{eq} = \sum_{i=1}^{2} Q_i(1 - \exp(-C_i p)) \tag{2.36}$$

Where Q_i: Adjustable constant material parameters

C_i: Adjustable constant material parameters

The updated material model is then:

$$\sigma_{eq} = [A + \sum_{i=1}^{2} Q_i(1 - \exp(-C_i p))]\left[1 + \left(\frac{\dot{\rho}}{\dot{\rho}_0}\right)\right]^C [1 - (T^*)^m] \tag{2.37}$$

A damage criterion is then needed to predict when fracture occurs. The Cockroft Latham damage criterion is used in this thesis. This damage criterion causes the fractures to be

dependent on both stresses and strains [24]. The damage criterion is also easily calculated using a uniaxial tension test.

$$\int_0^{\epsilon_f} \langle \sigma_1 \rangle d\varepsilon_{eq} = W \tag{2.38}$$

Where $\langle \sigma_1 \rangle = \begin{cases} \sigma_1 & when\ \sigma_1 \geq 0 \\ 0 & when\ \sigma_1 \leq 0 \end{cases}$

σ_1: Major principle stress

W: Material parameter

ε_f: Fracture strain

ε_{eq}: Equivalent plastic strain

The Cockroft Latham criterion, equation (2.38), states that damage accumulates until it reaches a critical value, $W = W_{cr}$. This occurs when $\varepsilon_{eq} = \varepsilon_f$. W_{cr} is then the area under the true stress/strain curve of the uniaxial tension test.

3 Material testing and calibration of the material model

A good material model is necessary in order to get correct results in the numerical study. Nine tension tests were performed on 1mm thin specimens of the aluminium alloy 1050A-H14, in three different directions, to identify the material properties.

3.1 Aluminium alloy 1050A-H14

The material that is being tested is the aluminium alloy 1050A-H14. It is manufactured by Impexmetal S.A./Huta Aluminium Konin in Poland. The aluminium alloy 1050 is known for excellent corrosion resistance, high ductility, highly reflective finish, and is preferred for general sheet metal work where moderate strength is required. It is typically used for food industry containers, chemical process plant equipment, architectural flashing and cable sheathing, among others [42].

The chemical composition of 1050A-H14 is shown in Table 1:

Table 1: Chemical composition 1050A-H14 [43]

Fe %	Si %	Cu %	Mg %	Mn %	Cr %	Ti %	Zn %
0.290	0.080	0.000	0.001	0.001	0.000	0.030	0.002

The temper H14 describes the degree of strain hardening, and indicates that the material represents a cold work half-hardened condition, not annealed after rolling [44][42].

3.2 Procedure

During the tension test, nine specimens with a given geometry (Fig. 10) and a thickness of 1mm were tested in the quasi-static regime. In order to check for anisotropy, the specimens were tested in three different orientations compared to the rolling direction; 0°, 45°, and 90°.

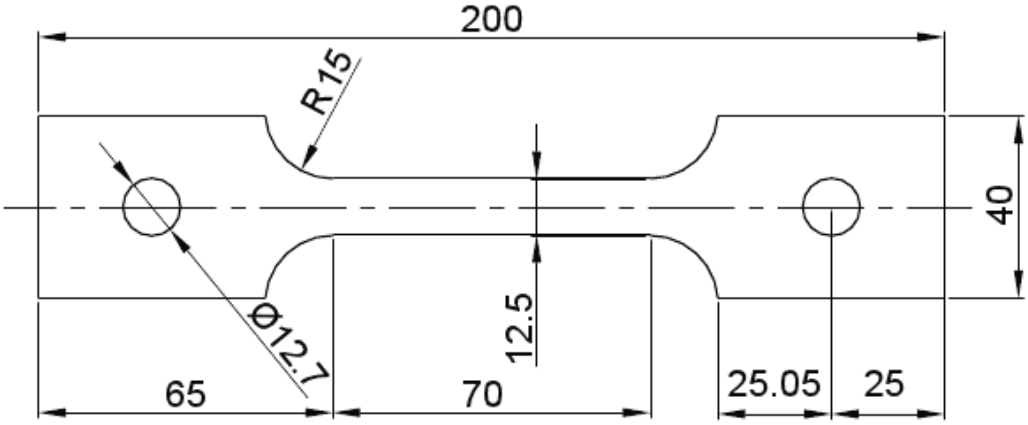

Figure 10: Specimen geometry

The tension tests were carried out in the servo-hydraulic Dartec M 1000 RK universal test machine (Fig. 11) at the SIMLab laboratories on NTNU. All specimens were stretched until fracture occurred. An axial force was applied to the upper bolt (Fig. 11) as a velocity set to 2.1 mm/min, giving a strain rate $\dot{\epsilon} = 5 * 10^{-4} s^{-1}$. A 40mm-extensometer was used to measure the elongation of the specimens until fracture. By recording elongation and force over time, it is possible to determine both engineering stress-strain as well as true stress-strain in the material.

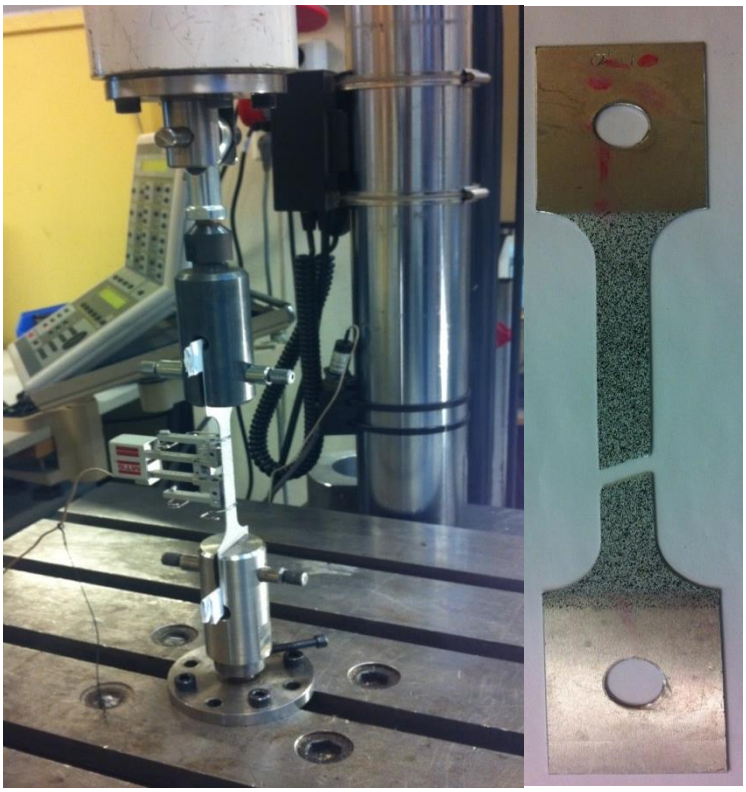

Figure 11: Dartec universal test machine – Material specimen number 1 (0°) after fracture

3.2.1 Stresses and strains

To calibrate the material model, some specific formulas need to be defined:

Engineering strain: $e = L/L_0$ (3.1)

Engineering stress: $s = F/A_0$ [MPa] (3.2)

Engineering stress and strain become inaccurate when deformation of the specimen is approaching necking [45].

True stress and strain have to be established:

True strain: $\varepsilon = \ln\frac{L}{L_0}$ (3.3)

True stress: $\sigma = s(1 + e)$ [MPa] (3.4)

An expression of the plastic strain is necessary to describe the hardening development of the material:

Plastic strain: $$\varepsilon^p = \varepsilon - (\frac{\sigma}{E}) \quad (3.5)$$

3.2.2 Necking

Necking occurs when the cross-sectional area of the material decreases by a greater proportion than the material strain hardens [46]. In a rectangular cross section, there are two forms of necking: *Diffuse* necking, which involves contraction in both the lateral and width directions, and *local* necking, where the specimen thins without further width contraction [47].

The formulas for true stress and strain are only valid until the tensile instability, and the results after necking are therefore being discarded. The criterion for necking is [45]:

$$\frac{\Delta\sigma}{\Delta\varepsilon} - \sigma = 0 \quad (3.6)$$

3.3 Results

The force-displacement plot of the different tests can be shown in Figure 12:

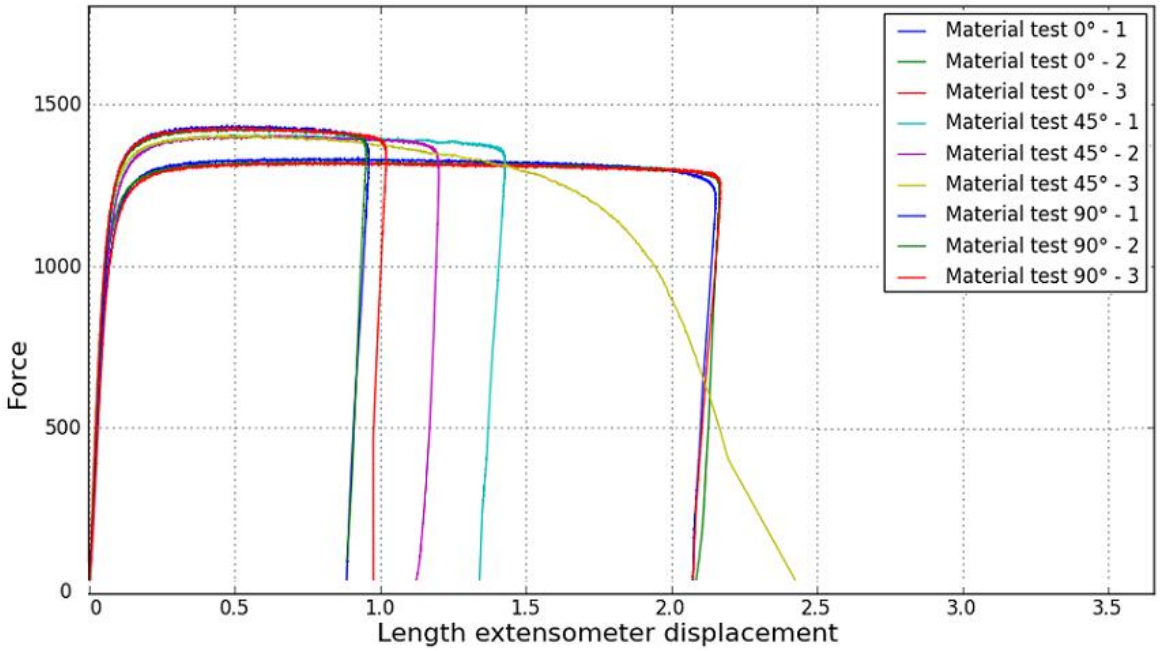

Figure 12: Force [N] - Displacement [mm] of material tests with different orientations

The true stress-plastic strain curve for both the 0° - and the 90° oriented material tests are shown in Figure 13:

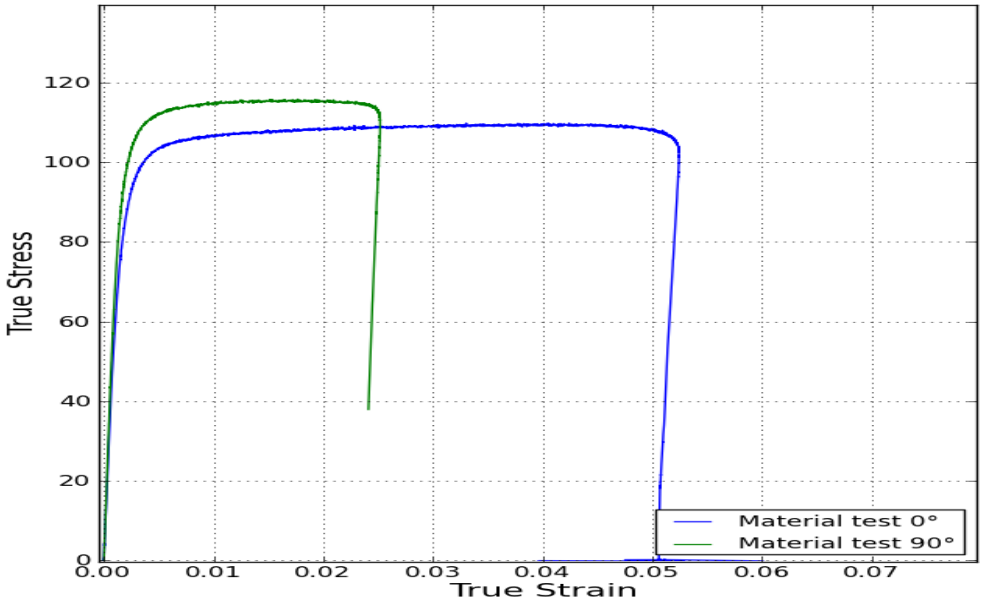

Figure 13: True stress [MPa] - True strain - 0° and 90° material test

The material model shows an anisotropic behavior. An orientation of 90° gives a larger stress tendency, and the 0° specimen has a more ductile tendency compared to the 90° specimen. The largest difference in response was between the orientations of 0° and 90°, so both of these directions are used for further calculations.

3.4 Calibration of material model

Due to the anisotropy of the material, both the stress-strain curves at 0° and 90° are used to calibrate the material model. The most substantial difference between the two specimen orientations seems to be the critical damage criterion W_{cr}.

To calibrate the strain hardening part of the modified Johnson-Cook material model, the Solver function in Excel and the calibration program MatPrePost was used. MatPrePost is developed at SIMLab NTNU and uses the force-displacement data from the tensile test to calibrate the material model [48].

The fitted curves can be seen in Figure 14, and the corresponding strain hardening parameters are:

0°: $Q_1 = 22.52 \quad C_1 = 1613.1 \quad Q_2 = 5.9553 \quad C_2 = 483.84 \quad A = 97MPa$

90°: $Q_1 = 17.733 \quad C_1 = 1825.2 \quad Q_2 = 8.1222 \quad C_2 = 209 \quad A = 106MPa$

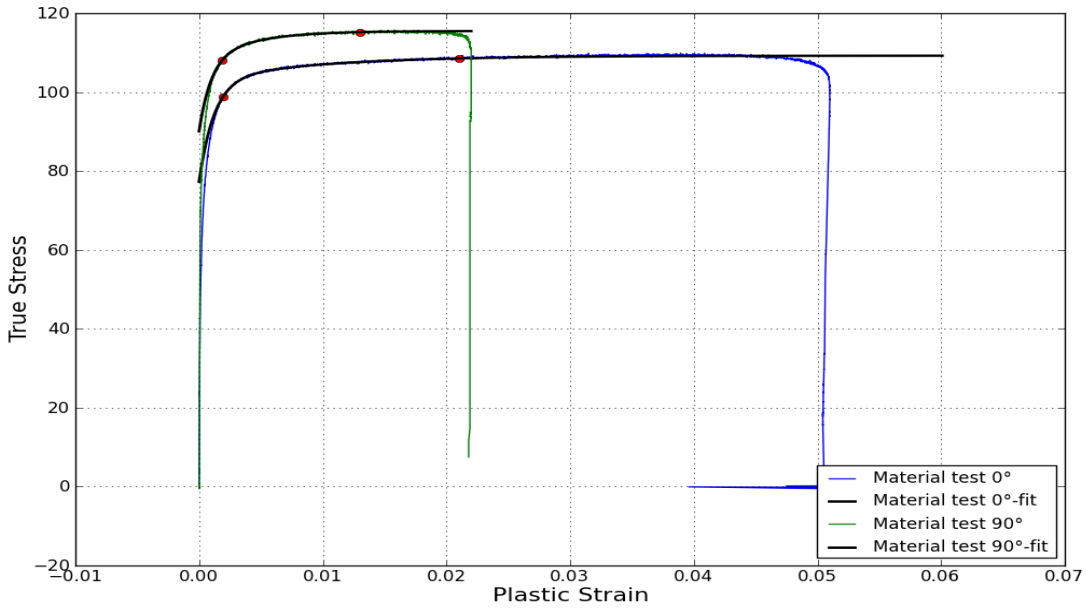

Figure 14: Fitted curves Voce

The strain rate parameter *C*, was acquired from datasheets [49].

The tensile tests were only performed during constant temperature, so the temperature softening parameter is assumed to be linear.

This gives the following material parameters used in the modified Johnson-Cook material model for specimen orientation 0° and 90°:

Table 2: Modified Johnson-Cook material model parameters for specimen direction 0° and 90°

		0°	**90°**
Poissons ratio	v	0.3	0.3
Mass density	$\rho\left[\frac{kg}{m^3}\right]$	2700	2700
Yield stress	$A[MPa]$	97	106
Voce hardening	$Q_1[MPa]$	22.52	17.733
	C_1	1613.1	1825.2
	$Q_2[MPa]$	5.9553	8.1222
	C_2	483.84	209
Strain rate sensitivity	C	0.0141	0.0141
Temperature softening	$T_0[K]$	293	293
and adiabatic heating	$T_m[K]$	922	922
	m	1	1
	$C_p[\frac{J}{kgK}]$	899	899
	χ	0.9	0.9
	$\alpha[K^{-1}]$	1.5×10^{-4}	1.5×10^{-4}

The critical damage parameter W_{cr} was found by modeling the test specimen in LS-DYNA with the material parameters that was provided by the Solver function in Excel and MatPrePost. The geometry of the test specimen was created in ABAQUS CAE on converted to LS-DYNA using a Matlab-script. The script can be found in the appendix. Both the test specimen and the bolts were modeled using shell elements. The element size was initially set to 4mm, but for increased accuracy in the area where the extensometer was placed the element size was set to 1mm (Fig. 15). For the rigid bolts the material card *MAT_RIGID was used. The material card *MAT_107 was used to input the modified Johnson-Cook material parameters to the test specimen. The keyword file can be found in the appendix.

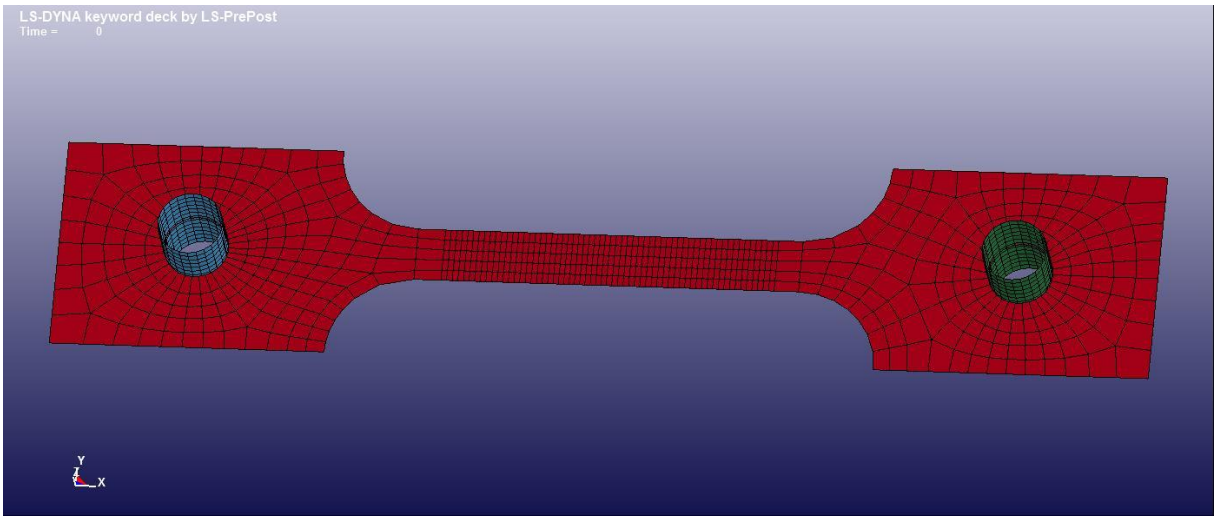

Figure 15: Tension model in LS-DYNA

The tensile test was then run in LS-DYNA and W_{cr} was plotted against the strain for both 0° and 90° (Fig. 16). For the test specimen at 0°, necking occurred at a strain of 0.045. The value of W_{cr} at this strain value is being used in further calculations, so $W_{cr}(0°) = 5.414$. For the test specimen at 90°, necking occurs at a strain value of 0.02, so $W_{cr}(90°) = 2.485$.

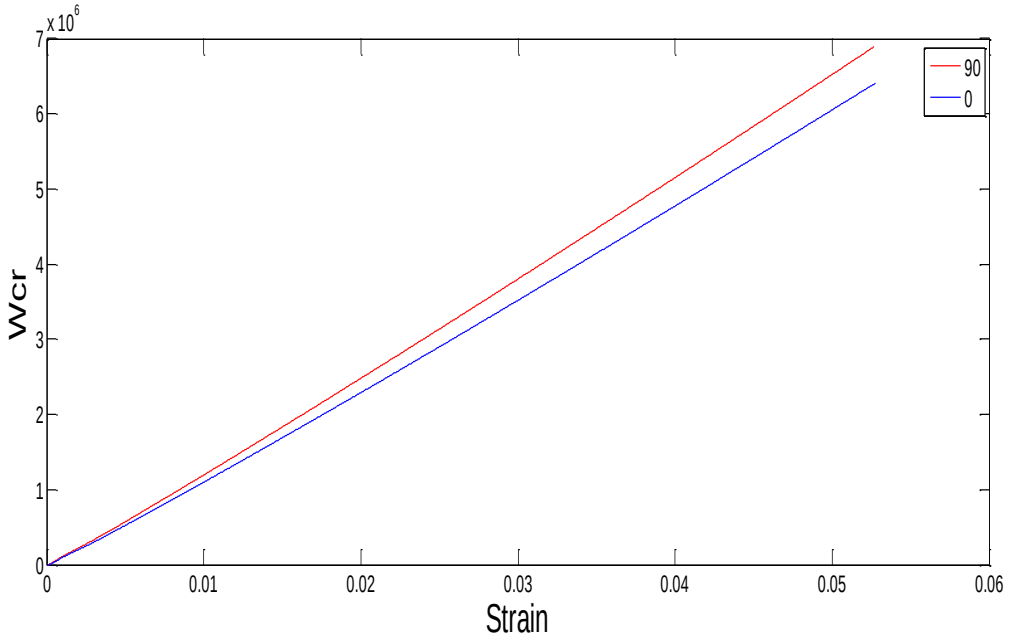

Figure 16: Wcr against strain for specimen orientations of 0° and 90°

3.5 Discussion

The tensile test showed that the material had anisotropic behavior, with the biggest difference in orientation being 0° and 90°. It is also shown that $W_{cr}(90°)$ is 45.9% of $W_{cr}(0°)$. Because of this substantial difference both material orientations were chosen for further analyses in the preliminary study in chapter 4. An alternative material model that accounts for anisotropy could be used instead of the modified Johnson-Cook material model, but since Grytten [41] suggests that impact and penetration problems could be reasonably well predicted using the Johnson-Cook material model, this material model is chosen.

Figure 12 shows that test 3 at 45° has a different displacement course than the rest of the test specimen. This is because that test specimen experienced necking at the center of the specimen, while the others necked at the bottom close to where the extensometer was fastened. This suggests that because the specimens are very thin, small variations over the thickness might give very different displacement results.

4 Preliminary Study

In order to predict what results the experiments in this thesis would give, a preliminary study was carried out. First a mesh sensitivity study was done to find the smallest mesh size needed to get accurate results, secondly the boundary conditions were examined to see how they affect the results.

At this point in the thesis the material data for 1050A - H14 was not yet available so the material data for 1050A - H24 was used instead (Tab. 3). H24 is a slightly higher tempered material than H14, but has overall similar capabilities [50].

Table 3: 1050A - H24 Johnson-Cook material parameters

A (GPa)	**B (GPa)**	**n**	**C**	$T_m(K)$	**m**	$C_p(\frac{J}{kgK})$
0.110	0.150	0.360	0.014	918.15	1	899

The numerical simulations in this thesis were carried out in both LS-DYNA and IMPETUS Afea, but in this preliminary study only LS-DYNA was used. All analyses are Lagrangian with various load curves. In order to reduce computational time and storage space used, the double symmetry of the test plates is used. The double symmetry does not significantly alter the results of the analysis [2].

Examples of keyword files used in these simulations are included in the appendix.

4.1 Mesh Sensitivity Study

The mesh sensitivity study will determine the element size used in the later analysis. The plate is modeled in a rigid frame and fastened with bolts, which is one of the boundary conditions that have been proposed for the actual experiments (Fig. 17).

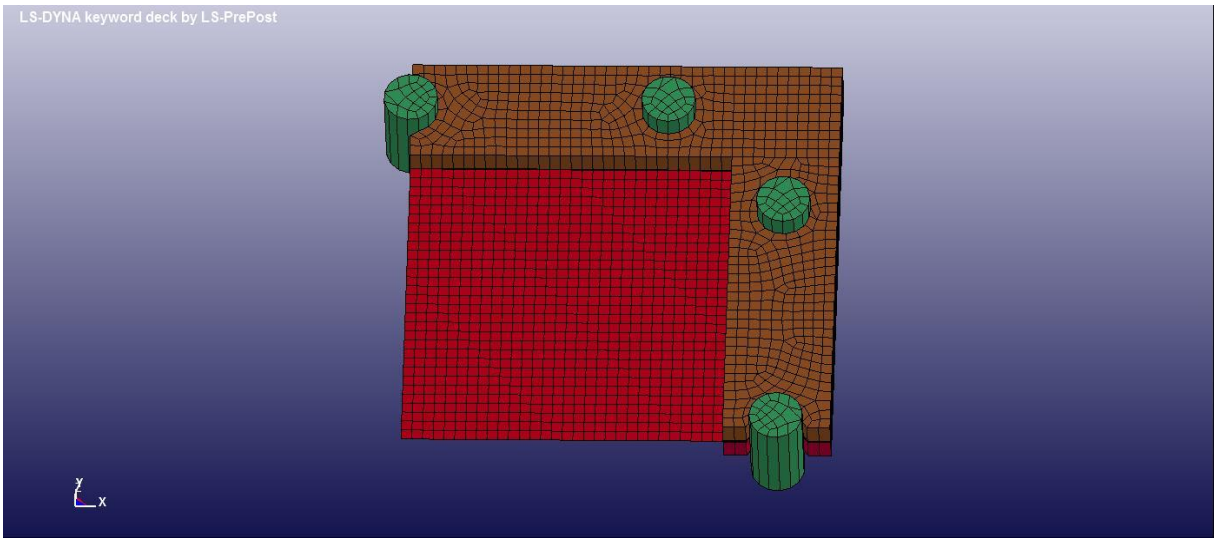

Figure 17: Bolted boundary condition

¼ of the plate was modeled with the geometry 200x200x1mm using shell elements and the material parameters was inputted using the *MAT_107 card. The material card with the parameters for 1050A - H24 is as follows:

Table 4: Material card *MAT_107 – 1050A-H24

*MAT_107
$ MID RO E PR BETA XSI CP ALPHA
1 2700.0000 7.1000+11 0.3000000 0.0000000 0.9000000 452.0000 1.2000-5
$ E0DOT Tr Tm T0 FLAG1 FLAG2
1.00000-3 293.00000 918.00000 293.00000 0.0000000 1.0000000
$ A B N C m
1.1000+8 1.5000+80 0,0014000 0.0000000 1.0000000
$ Q1 C1 Q2 C2
00000000 0000000 000000 000000
$ DC WC
1.0000000 7.3400+8
$ TC TAUC
829.0000 1.0000+20

The frame and the bolts were modeled using rigid volume elements and the material card used was *MAT_RIGID, constrained from moving in any direction.

The loading was applied by using the *DEFINE_CURVE card. Examples of the load curves that are being used can be found in the keyword files in the appendix. The pressure load is a bit larger than the ones that will be applied in the actual experiments, but it is assumed that the larger the deformations are the more mesh sensitive the model will be.

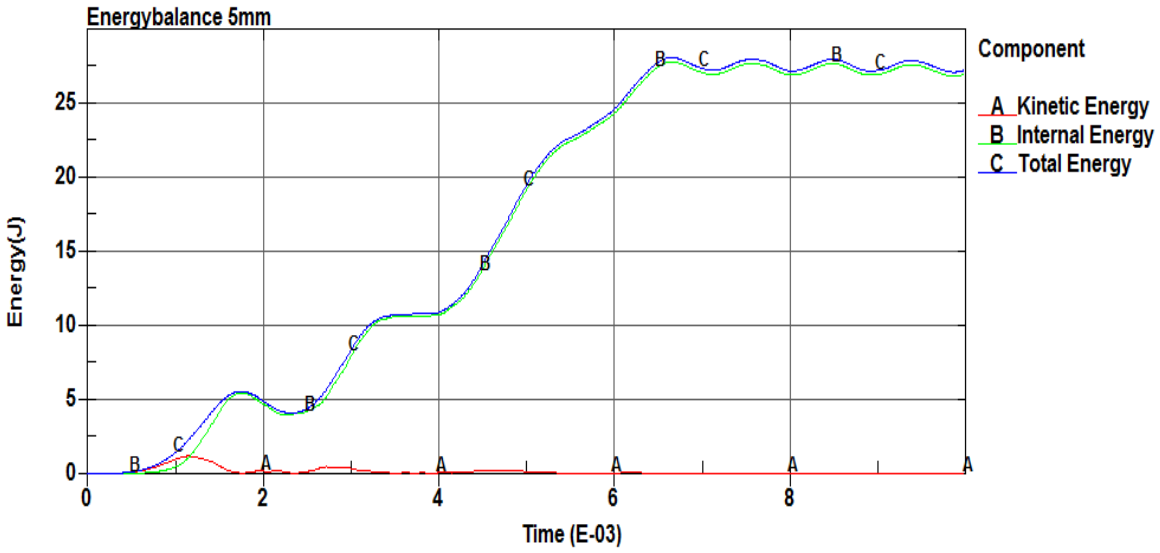

Figure 18: Energy balance 5mm

Figure 18 shows the energy balance of a simulation run with a 5mm element size. The kinetic energy, shown in red, is very low compared to the total energy. This indicates that the 5mm element size for this numerical model could be a reasonable choice for further simulations.

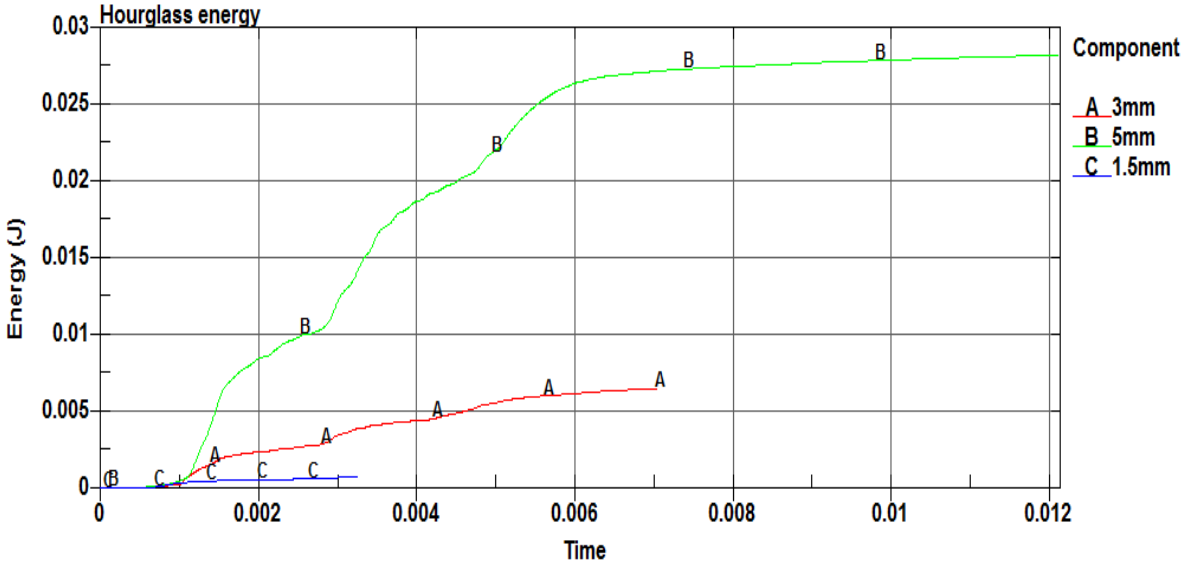

Figure 19: Hourglass energy

Figure 19 shows that smaller element size gives less hourglass energy, but even the 5mm mesh gives an hourglass energy of 0.1% of the total energy (Fig. 18) which is acceptable. The hourglass-energy seems to converge, and it is little to gain in terms of accuracy by reducing the element size further.

Table 5 shows the computation time for each element size simulated in the preliminary study. The time needed to finish the analysis increases dramatically with decreasing element size. Decreased element size also contributes to a similar increase in disk size needed to store the results. This supports the decision to use an element size of 5mm in the main numerical simulations.

Table 5: Elapsed time of the analyses

Element size (mm)	Number of processors	Computation time (hh:mm:ss)
5	2	0:17:42
3	2	0:26:01
1.5	2	0:57:31

4.1.1 Deformation

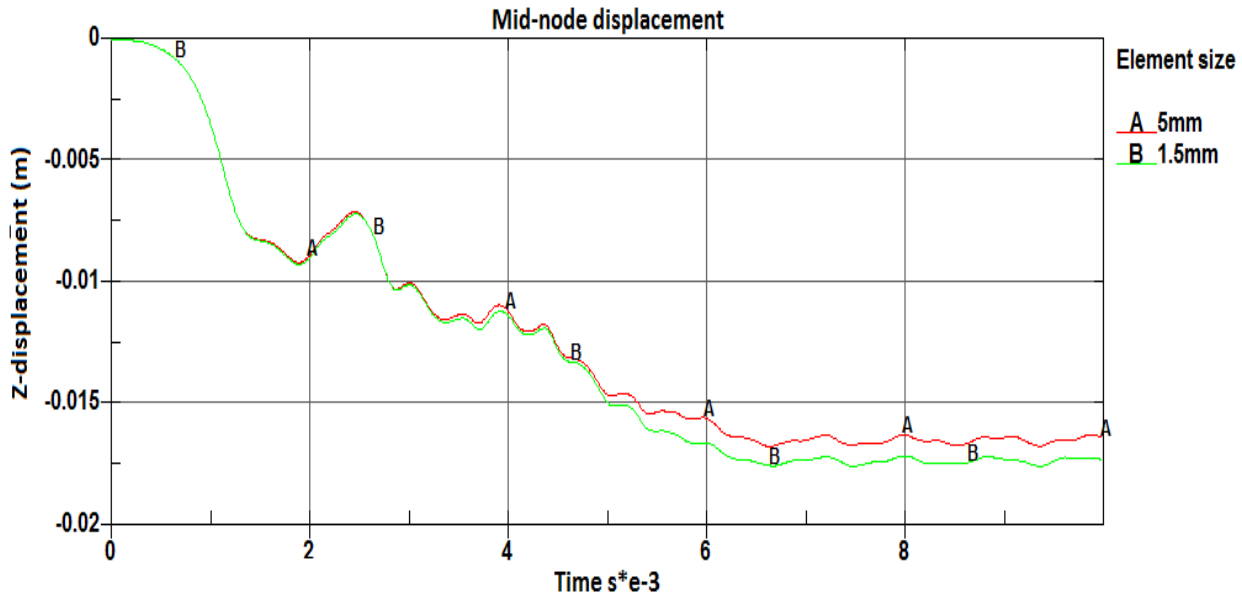

Figure 20: Mid-node displacement for 5mm and 1.5mm

Figure 20 shows the mid-node displacement for both meshes 5mm and 1.5mm. The two curves are very similar and show only a difference in displacement at the end of the loading of about 1mm, which is deemed sufficient for the experiments conducted in this thesis. For the numerical simulations in this thesis, an element size of 5mm should be sufficient because fracture is not predicted. However, should fractures occur in the plate test, a smaller element size should be considered.

4.2 Boundary conditions

In order to determine what type of boundary condition to use in the plate experiments, two types were simulated in LS-DYNA: Bolted, and with loose clamps in the corners. Bolted plate is shown in Figure 17, while the loose clamp boundary condition is shown below in Figure 21.

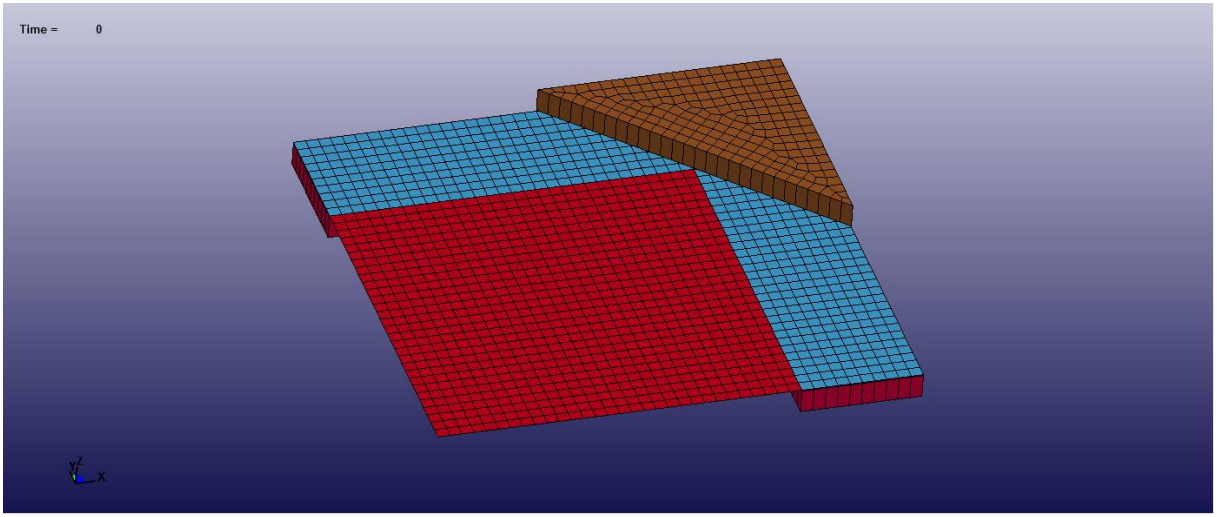

Figure 21: Plate placed in loose clamps

The loose clamp boundary condition is modeled by placing the aluminium plate on a rigid frame and placing a triangular steel piece over it in the corners only. The plate can glide frictionless between the frame and the steel piece. The frame and the steel piece is modeled as volume elements and the *MAT_RIGID card is used.

Both boundary conditions are being simulated with a load equivalent of 40 bar, and the load curve used in the *DEFINE_CURVE card is used from sensor 2 from Rakvåg [2].

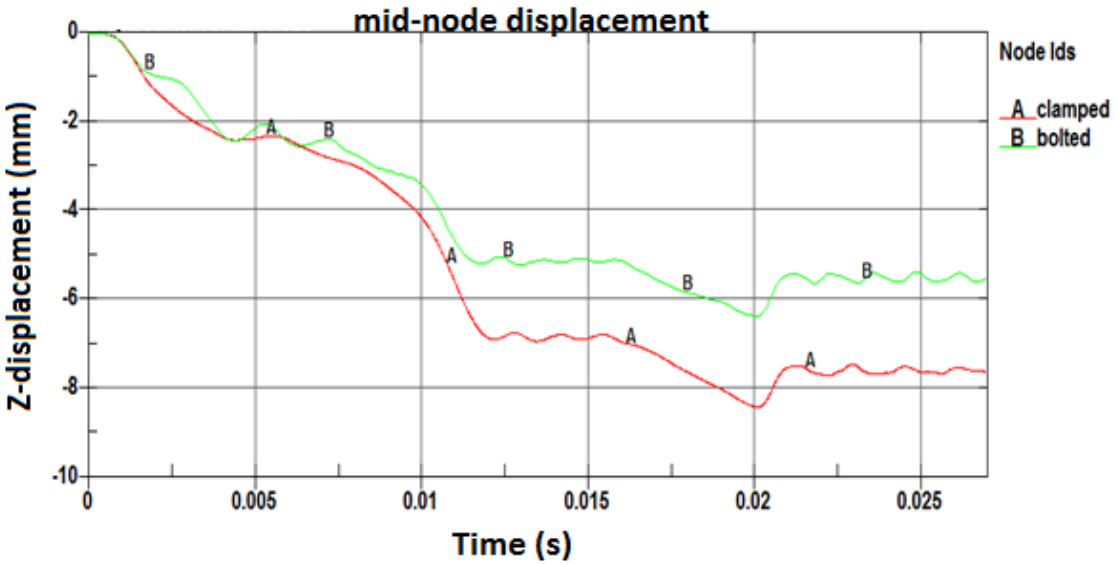

Figure 22: Displacement in mid-node for different boundary conditions

Figure 22 shows that the loose clamped plate has a larger mid-node displacement than the bolted plate. Considering that this is the result from a load equivalent of 40 bar, a bolted plate might not give significant plastic deformation if the pressure is reduced to 5 and 10 bar which are some of the loads proposed for the actual experiments. Should there only be small deformations in the actual experiments, switching from bolts to loose clamps should be considered.

4.3 Difference in specimen orientation

In order to determine how different the response of plate will be to the different specimen orientations, new simulations were run with the material values from chapter 3. The plate was modeled with the loose clamped boundary condition as shown in section 4.2, and with a mesh of 5mm. Also, the same load curve was used as in section 4.2. The simulation ran twice, once with the material parameters for specimen orientation of 0° and once with the material parameters for 90°.

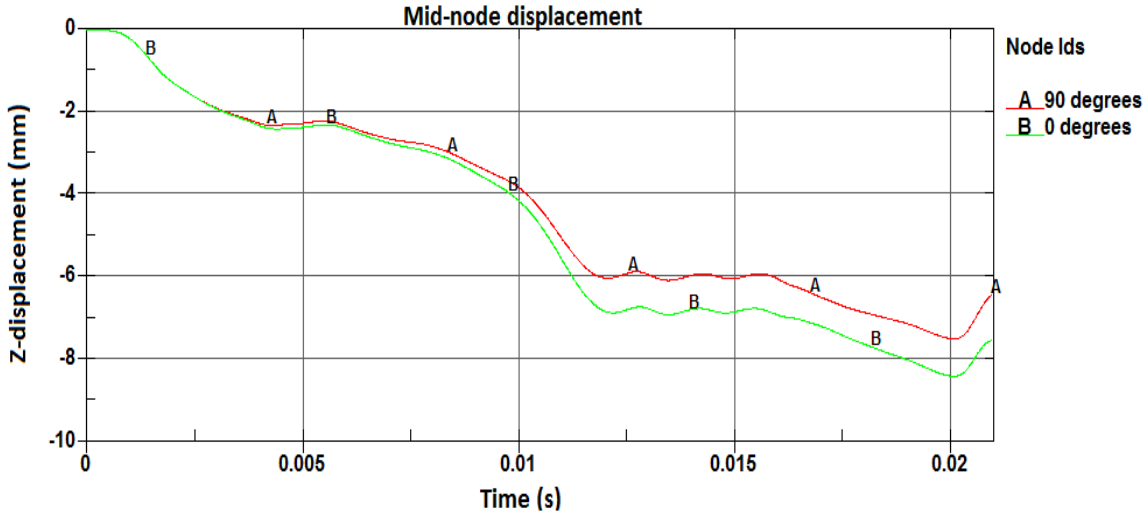

Figure 23: Mid-node displacement - 0° and 90°

Figure 23 shows the difference in mid-node displacement for 0° and 90°. The difference is about 1mm at the largest. Since these values show the material behavior in the strongest and weakest specimen orientation, it is probable that the real plate will show the behavior of something in between these two displacement histories. This difference is not substantial for

the experiments conducted in this thesis, so only the material parameters for 0° is used for further simulations.

4.4 Discussion

As seen in Figure 20, decreasing the element size beyond 5mm does not significantly alter the results. It does however greatly increase computation time, which makes 5mm a good choice for further simulations.

The numerical simulation indicates that the bolted boundary condition yields smaller deformations than the loose clamped boundary condition. In the actual experiment it is expected that the difference in deformation between the two alternatives will be bigger as the bolted boundary condition will also induce friction forces as the bolts tighten the steel frame to the aluminium plate.

The material test and tensile indicates that specimen orientation might have a large influence on the deformation of the plate, but as shown in section 4.3 the difference is small. W_{cr} might have been an issue if the loading was bigger and there was a risk of fracturing, but while using the load curve from Rakvåg [2] the material shows no signs of fracture. It is unlikely that the loading in the experiments conducted in this thesis will be substantially larger than the load from Rakvåg's 40 bar experiment [2]. It is expected that the numerical simulations from this preliminary study will give a good indication of the results from the actual experiment, depending on the boundary conditions.

5 Plate testing

The purpose of the laboratory experiments is to simulate blast loading on test specimens, to investigate the synergetic effect of both blast loading and fragmentations on thin aluminium plates. The plates that were subjected to the blast loading were of the dimension 400x400x1mm and aluminium alloy 1050A - H14 (Fig. 24). Also two plates with holes shaped as diamonds and slits were tested (Fig. 25).

Figure 24: 1050A-H14 plate

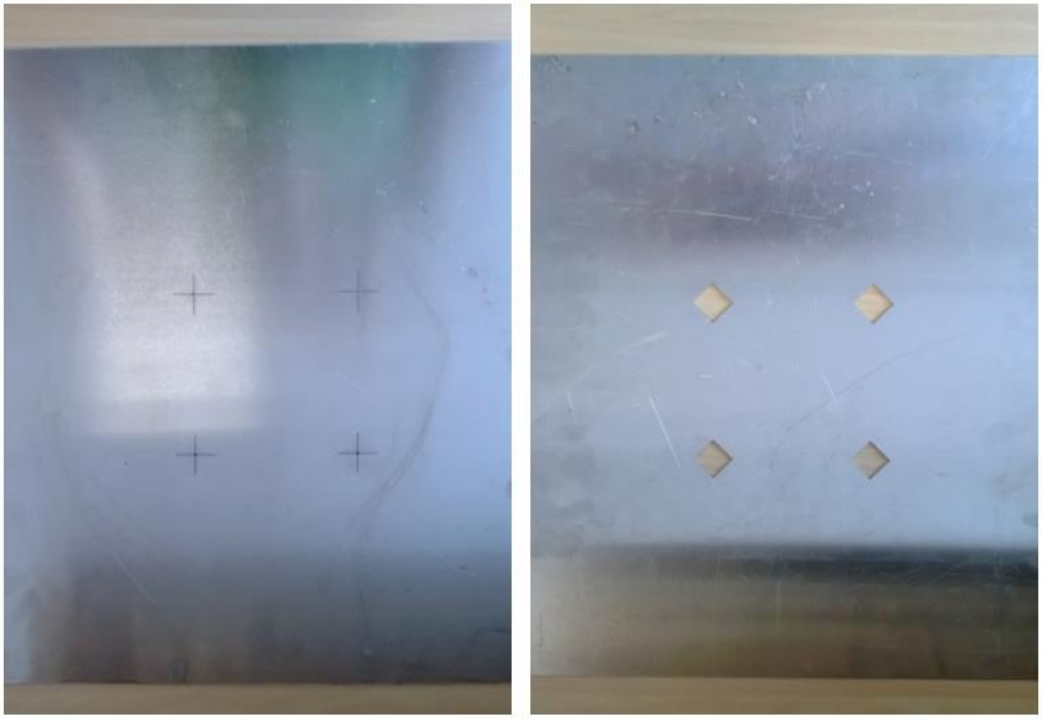

Figure 25: Aluminium plate with slits (left) and diamond-shaped holes (right)

5.1 Procedure

The laboratory experiments were performed in the SIMLab laboratories in NTNU. A compressed gas gun, originally intended for ballistic impact studies, was used. The main components of the gas gun are a 200 bar pressure tank, a firing unit for compressed gas, a 10 meter long smooth barrel of caliber 50 mm, and a closed 16 m^3 impact chamber (Fig. 26) [51].

The pressure in the pressure tank is denoted in bar, while the pressure that is measured by plate sensors in the impact chamber is denoted in kPa. It is known that 1 bar =100kPa ≈0.98692atm [52].

An illustration of the test rig is shown in Figure 26:

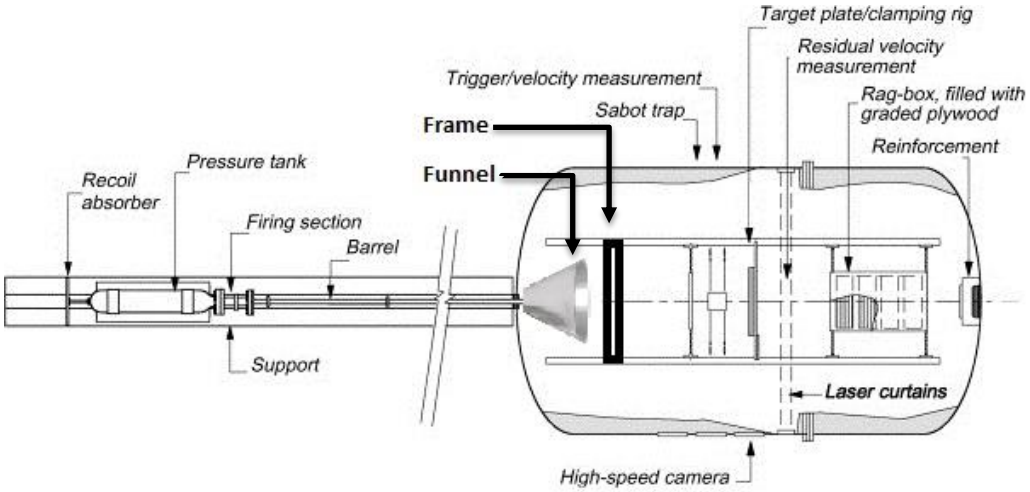

Figure 26: Schematic drawing of the test rig with modifications [53]

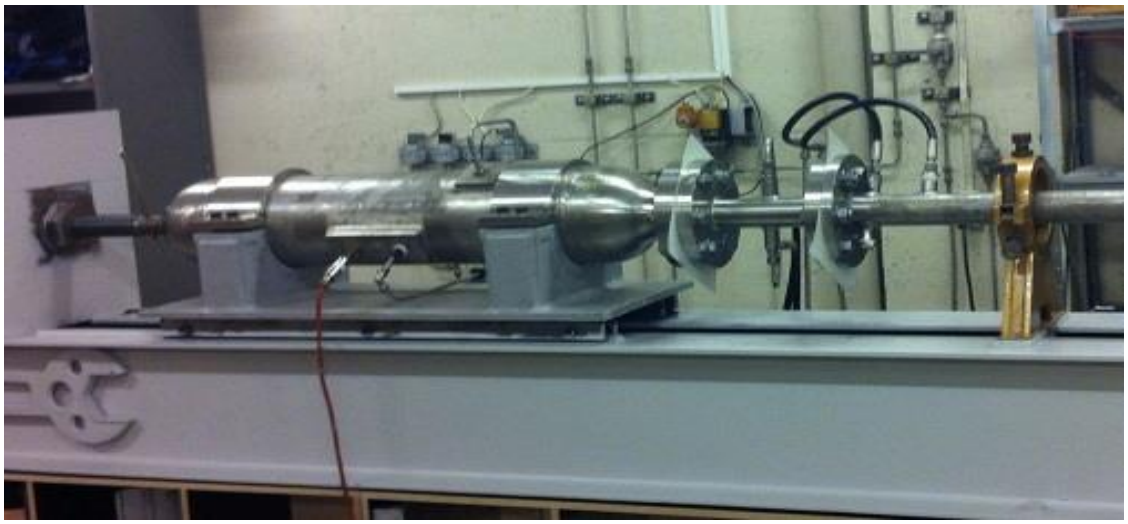

Figure 27: Pressure tank and firing section with membranes

The way the gun is operated is that the pressure tank is filled to the desired pressure, and the firing section is filled to half that pressure. A membrane is separating the pressure tank and the firing section, and another membrane separates the firing section and the barrel (Fig. 27).

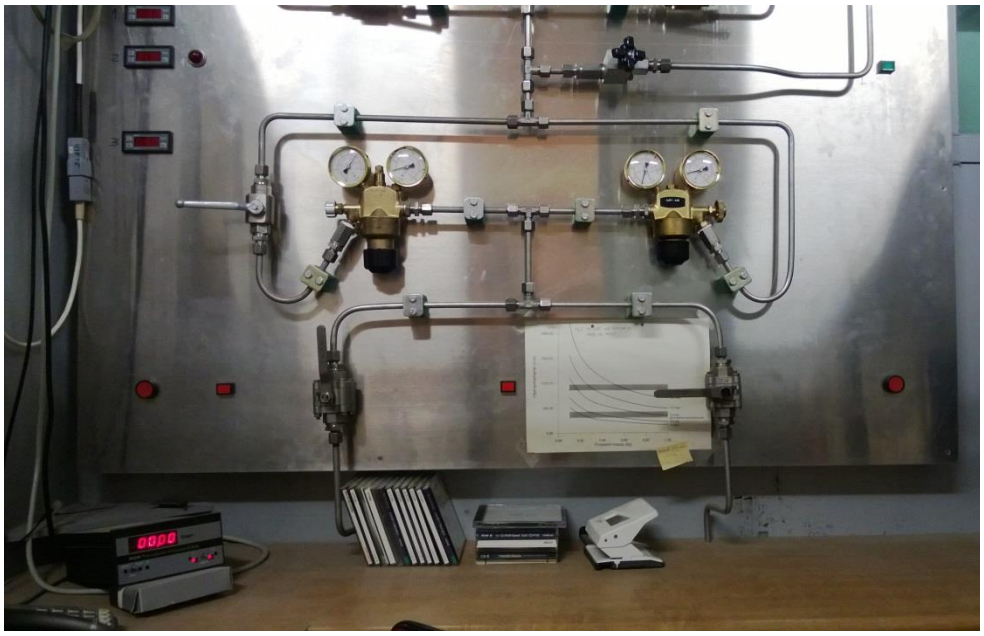

Figure 28: Manually firing mechanism

The membranes have a specific pressure capacity, so when the air in the firing section is emptied fast, the pressure gradient gets doubled and the membranes yield. This firing mechanism (Fig. 28) is a good way to control the yielding of the membranes and the exact magnitude of the pressure fired at the test specimen. The accuracy is dependent of the person operating the firing mechanism.

5.1.1 Calibration of pressure tank

To establish a correct numerical model of the experiments, it is important to know how large the pressure applied to the plate inside the impact chamber is. Since the experiments are based on pressure load, it is necessary to know whether the load has been reduced through the pipe or not. A rigid steel plate, equipped with 11 pressure transducer sensors (Fig. 29), was placed in the frame. Sensor number 5, 10, 12, 14, and 16 were not being used.

Figure 29: Arrangement of pressure transducers

The transducers used are Kulite XT-190 50 psi (3.5 bar), and the data was run through a Dewetron Strain Gage Amplifier and sampled in a National Instruments PXI-6123 Data Acquisition Card [2]. The instrumentation frame was operated by Knut Ove Hauge, from the Norwegian Defence Estate Agency.

The pressure tank was calibrated for pressures ranging from 5 to 30 bar. The calibration procedure was as follows:

1) 2 tests - 5 bar
2) 2 tests - 10 bar
3) 2 tests - 15 bar
4) 2 tests - 20 bar
5) 1 test - 30 bar
6) 2 tests – using only the firing section ≈10 bar
7) 1 test – using only the pressure tank≈10 bar
8) 1 test – using both the pressure tank and firing section (1 membrane) ≈10 bar

The purpose of test 6-8 was to investigate how the combination of the firing section and pressure tank affected the response of the pressure load.

The Dewetron amplifier has a built in 100 kHz low pass filter [54]. In addition to the low pass filter, a 2.order Butterworth filter with a 100 Hz cut off frequency has been used in Matlab.

Filtration will remove some information, but this is necessary to capture the tendency of the noisy raw data. The script used for filtration is shown in the appendix.

The comparison between raw data and filtered data, for sensor 1 and sensor 6 with a pressure load of 20 bar, are presented in Figure 30:

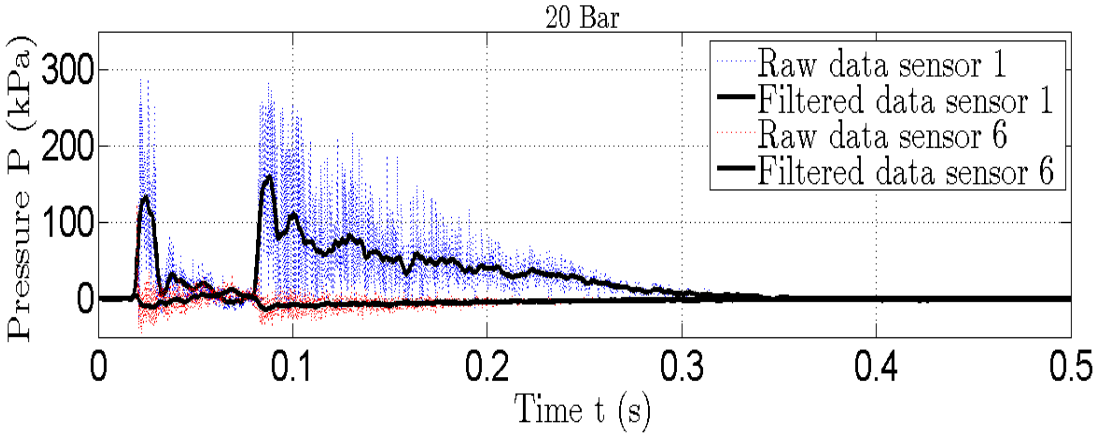

Figure 30: Raw data and filtered data for 20 Bar

The filtered data seems to be a sufficient approach to the raw data, and will be used from now on in this thesis.

To verify the repeatability of the gas gun, two tests were performed for each loading, except for the 30 bar test. The results are shown in Figure 31:

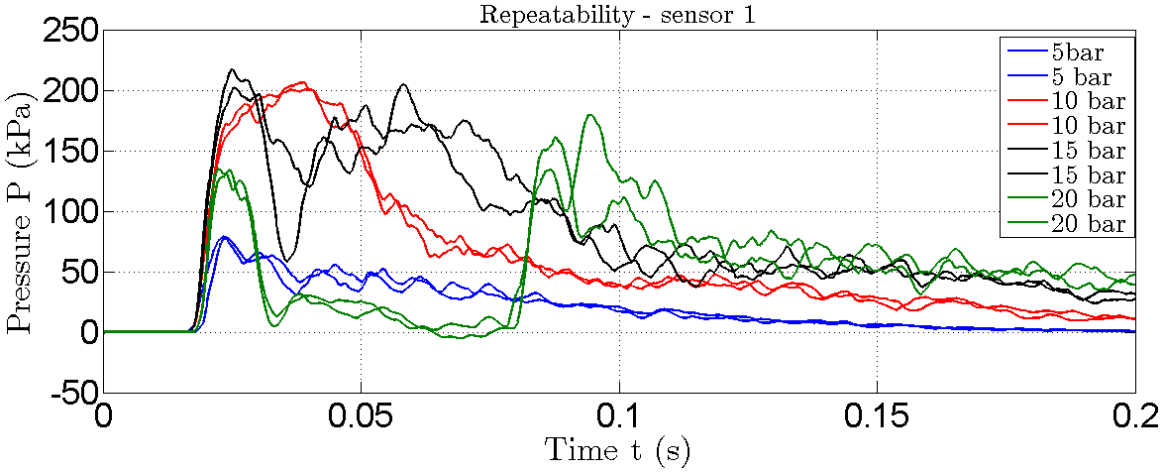

Figure 31: Repeatability of gas gun - sensor 1

There are a few small differences between the 15 bar tests at about 0.04 seconds, and between the 20 bar tests at about 0.1 seconds. Except from that, the repeatability of the test is deemed good. For sensor 6, the repeatability is shown in Figure 32:

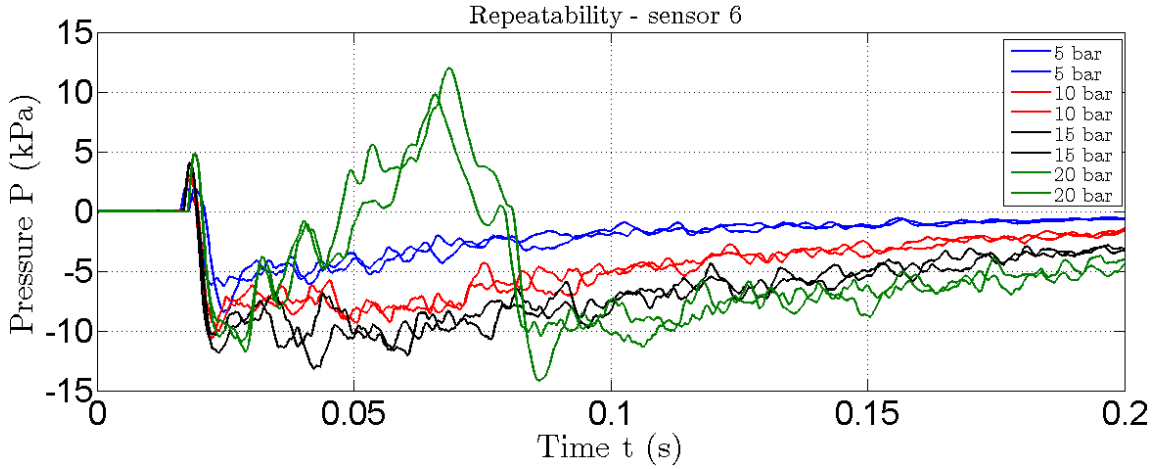

Figure 32: Repeatability of gas gun - sensor 6

Also for sensor 6, the pressures have similar response during the calibration, and the repeatability of the gas gun can be characterized as good.

The small differences that occur may be caused by several factors, i.e. small variations over the thickness of the membranes used in the firing mechanism, changed pressure conditions in the barrel from previous firing, or the fact that the shots were fired manually causing the pressure to vary slightly.

A comparison of all pressures for sensor 1 can be shown in Figure 33:

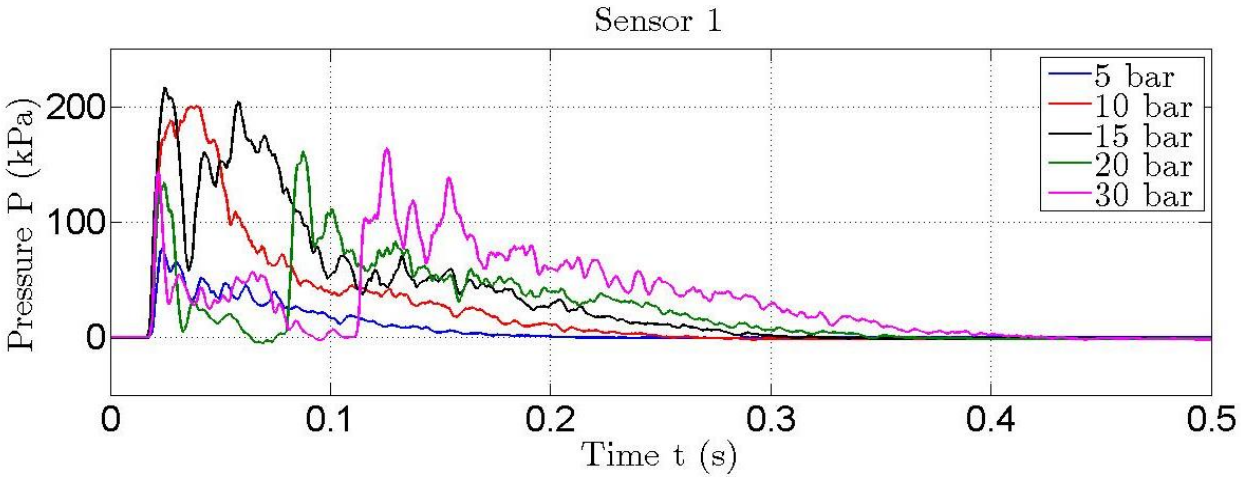

Figure 33: All pressure loads - sensor 1

All load curves have a pressure drop after the initial peak, however the 10 bar peak pressure is maintained over a wider time frame than the rest of the pressure loads, shown in Figure 34:

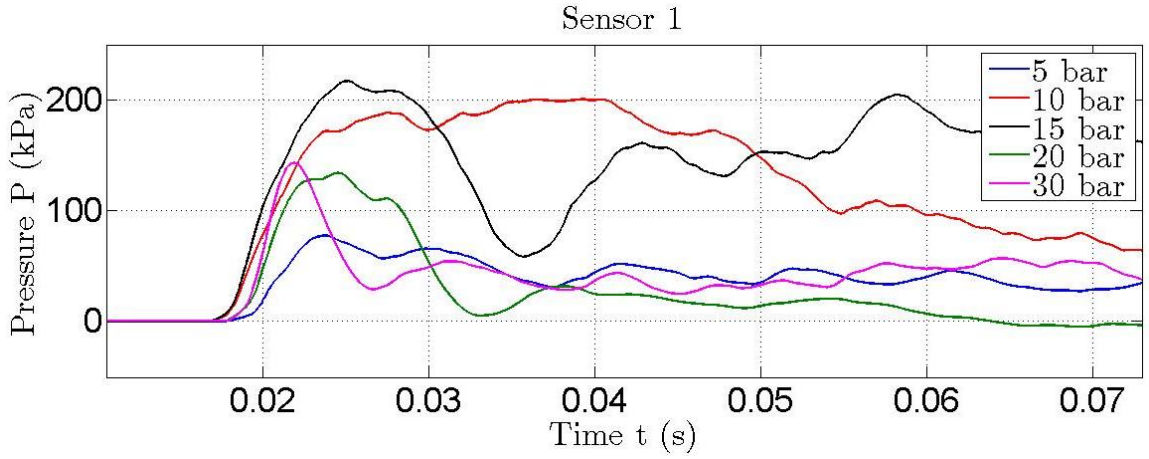

Figure 34: The initial peaks - all pressure loads

The 5 bar test corresponds well to the 10 bar test, since the pressure is about twice as big in the 10 bar test. It is interesting to see that the 20 and 30 bar tests have a smaller initial peak pressure. The reason to this may be that too much pressure tries to evacuate the pipe at the same time, which causes a "choke effect" of the airflow. A pressure load of more than 10-15 bar will therefore become choked through the nozzle, and will cause less dynamic pressure than for ideal pressure waves, described in section 2.1.1. This explains why the initial peak values decrease when loading increases. It is also noticeable that the 15 bar test has almost the same initial peak value as the 10 bar test, but it has a larger impulse (Fig. 33). The same tendency is visible for the 20 and 30 bar tests. A larger pressure load gives a larger impulse (Fig. 33) and this will affect the impact on the plates.

Compared to the load curves obtained by Rakvåg [2], a difference in pressure load of about 50-100 kPa is noticeable in Figure 35:

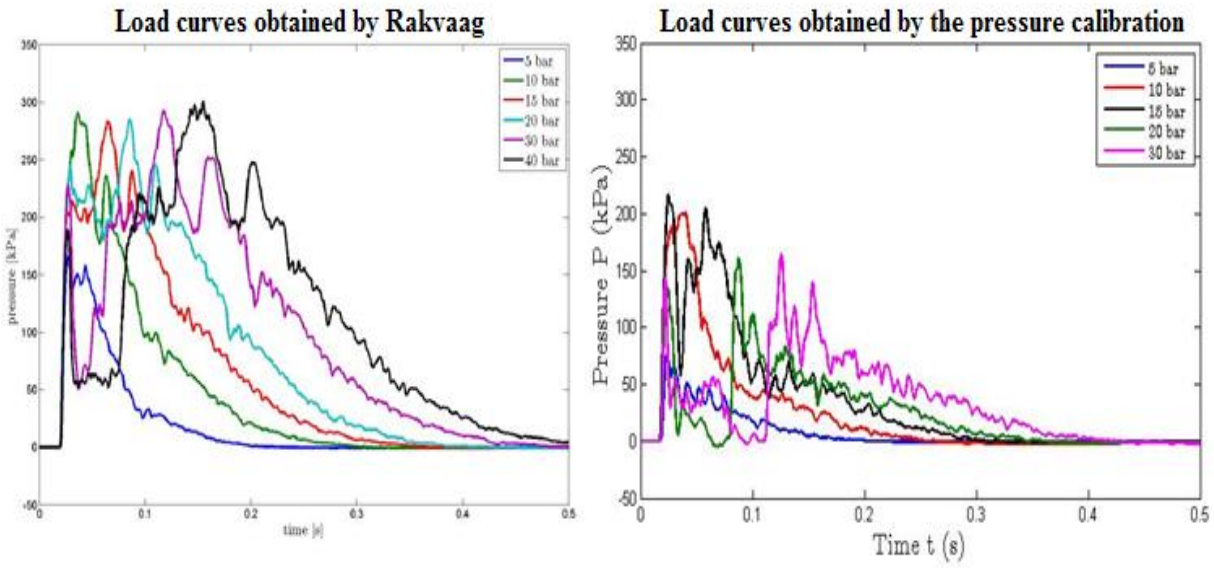

Figure 35: Comparison of sensor 1 load curves – Rakvåg (Left) - Current pressure calibration (Right)

The reason for the reduced load curves obtained by the pressure calibration is probably caused by the funnel at the end of the barrel. The purpose of the funnel is to prevent the air flow from flowing freely in the impact chamber, and to lead the pressure directly to the plate. But it can be assumed that as a consequence of the funnel, the initial air flow is forced back into the funnel after hitting the plate, and this effect slows the rest of the air flow. Both the initial peak pressure and the impulse are therefore lower than the experiments performed by Rakvåg [2]. This is consistent with the findings of Andersen and Hernandez [55], who modeled the entire setup with and without the funnel in LS-DYNA with ALE.

Tests were also performed on the pressure tank and the firing section, individually and together. The purpose was to investigate how the combination of the chambers affects the response of the pressure load, when pressure increased until membrane failure. In these tests, the membranes yielded at approximately 10.3-10.4 bar. The results are shown in Figure 36:

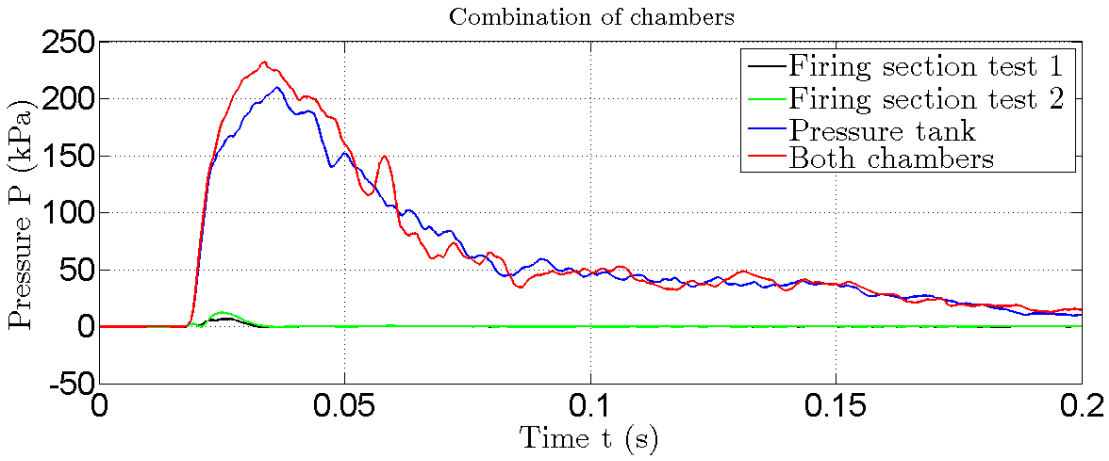

Figure 36: Combination of pressure chambers 10.3-10.4 bar

Compared to the pressure tank, the firing section test gave a minor response and the contribution from the firing section when using both chambers was insignificant. However, a pressure gradient between the two chambers is necessary to launch an air flow of an exact magnitude, and the firing section is therefore a central component of the gas gun.

5.1.2 Boundary conditions

The preliminary numerical simulations in chapter 4 indicated that the boundary conditions of the test plates would determine if plastic deformation was possible. In the experiments several different methods of fastening the test plates were tried out, to determine which boundary conditions that would yield plastic deformation, for 10 and 20 bar tests.

The test plates were initially fastened using bolts through a rigid frame (Fig. 37), however this boundary condition proved to be too rigid as the plates showed no sign of plastic deformation for 10 and 20 bar tests. This is also consistent with the results from the preliminary numerical simulations in chapter 4.

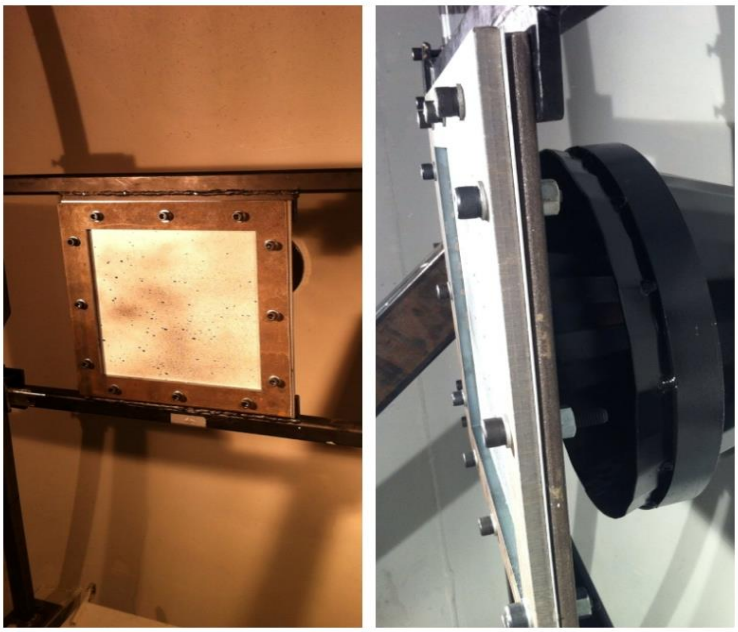

Figure 37: Bolted plate

As the rigid boundary conditions failed to give plastic deformations, it was attempted to let the plate move more frictionless in the rigid frame. The bolt holes were then cut out (Fig. 38) and the threads for the bolts where fastened as loosely as possible.

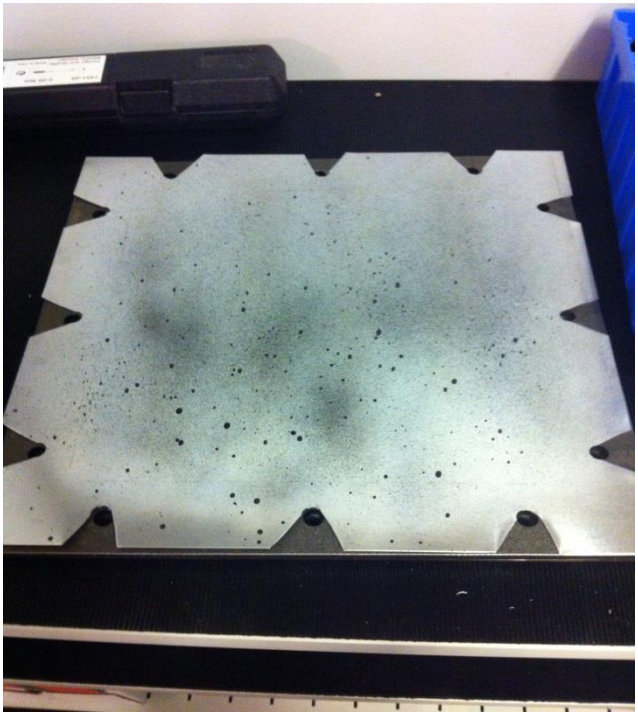

Figure 38: Cut out bolt holes

This boundary condition was able to yield plastic deformation at both 10 and 20 bar.

For the main experiments the plates were modified further, by attaching them to the rigid frame in the corners only, using loosely fastened clamps (Fig. 39). This makes it easier to fasten the plate and eliminates the potential human error when manually cutting pieces out of the plate.

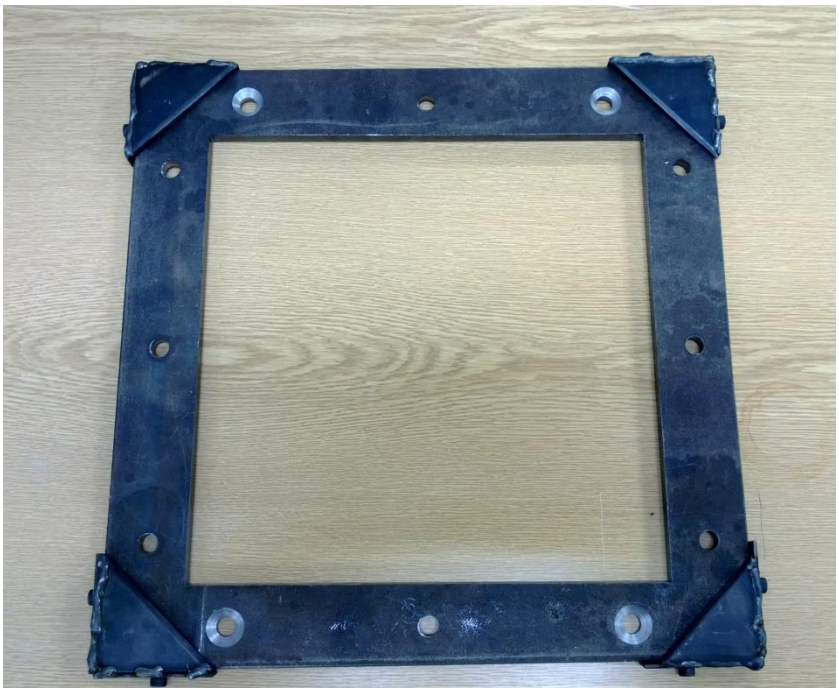

Figure 39: Clamping in corners

5.1.3 DIC calibration

For the initial experiments two high speed motion cameras of the type Photron Fastcam SA4 [56] was placed inside the impact chamber in front of the plates (Fig. 40). To protect the cameras from the pressure, a large transparent Plexiglas was placed in front of them. The Plexiglas was only fastened in the top, so it vibrated slightly when the gas gun was fired.

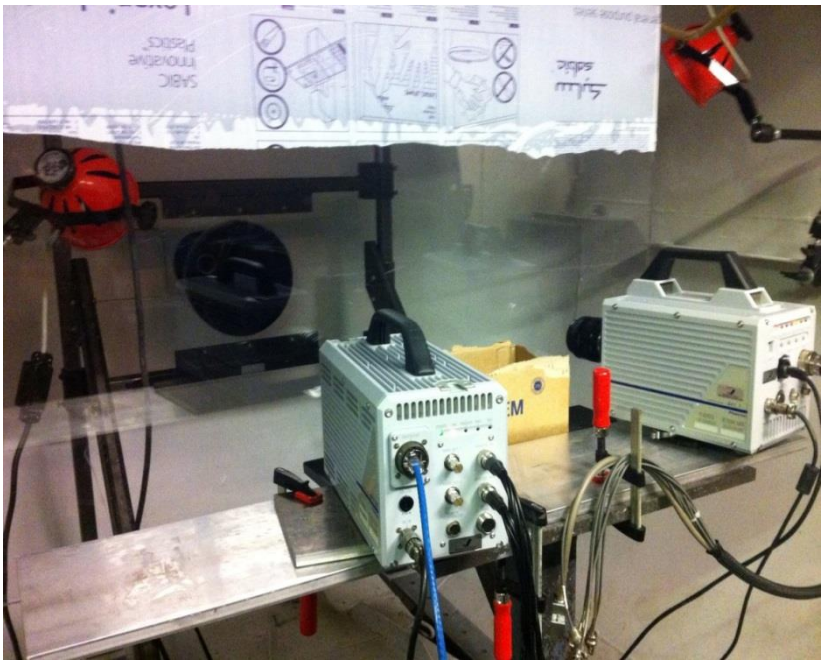

Figure 40: Initial camera setup

When processing the data from the two cameras, it was discovered that the vibrating Plexiglas blurred some of the images. A different setup was then applied by upgrading the cameras to Phantom v1610 [57] and placing them outside the impact chamber (Fig. 41). The higher resolution and accuracy of the new cameras seemed to provide satisfying results and was used in the main experiments.

Figure 41: Final camera setup

The upper half of Figure 41 shows the angle in which the cameras are placed, and the funnel and the frame is visible through the window. One of the benefits of using cameras with higher resolution is that they do not need to be placed directly in front of the object they are recording.

To get the contrast that the cameras need to calculate the grey-scale values [23], the aluminium plates are first painted white and then sprayed lightly with a black paint giving the surface a randomly speckle pattern of black and white paint (Fig. 42). The painting is done manually.

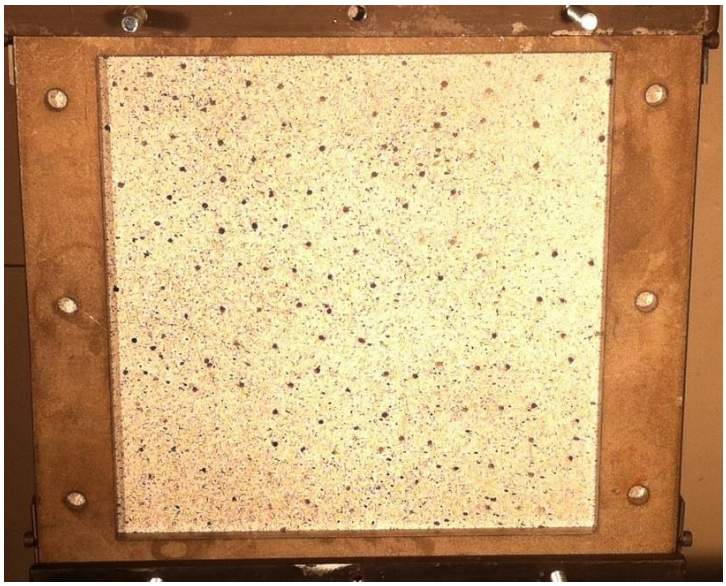

Figure 42: Painting of plate

5.1.4 Loads

As a result of the calibration of the equipment, the pressure that the gas gun was filled with in the main experiments was set to 30 bar, 20 bar and 10 bar. These pressures were used during the calibration of the equipment and yielded plastic deformations on the aluminium plates. Higher pressure was not used because of the risk of having the plates sliding out of the rigid frames. As shown in section 5.1.1, the pressure that actually hits the plates are significantly lower than the pressure loaded in the gas gun. The plates with diamond shaped holes and slits were only tested at 20 bar.

5.2 Results

Several tests were performed on the 1mm 1050A-H14 plates, for 10, 20 and 30 bar blast loading.

All of the tests at 10, 20 and 30 bar yielded plastic deformations. The plates tested at 20 (Fig. 44) and 30 bar (Fig. 43) showed very similar deformations while the plates tested at 10 bar showed a little less deformation (Fig. 47). The plates with slits and diamond-shaped holes (Fig. 50 and Fig. 51) showed similar deformation as the plates without penetration.

It was only possible to extract information from DIC on the plates tested at 20 and 10 bar. There could be several reasons for this, but it is most likely that since the aluminium plates were spray painted manually, the pattern on some of the plates was not distinct enough, so the software was not able to get enough contrast in the image in order to assign enough gray-scale values to register the displacements. For the plates that DIC worked on successfully, the results were impressive.

No crack propagation was seen on any of the tested plates.

5.2.1 Deformations

This chapter illustrates the deformation of the 10, 20 and 30 bar test plates. The DIC-analysis was only able to yield results on the 10 and 20 bar experiments (Fig. 45 and Fig. 48).

30 bar:

For the 30 bar experiment, the deformation of the plate is shown in Figure 43. Most of the buckling localized in a fold on the left side of the plate. The displacement in the center of the plate was measured manually with a caliper and was 37mm.

Figure 43: Deformed plate - 30 bar

20 bar with DIC:

Figure 44: Deformed plate - 20 bar

The deformation of the plate for the 20 bar test is shown in Figure 44, and the DIC-analysis showed a total mid-node displacement of 26.8mm (Fig. 45).

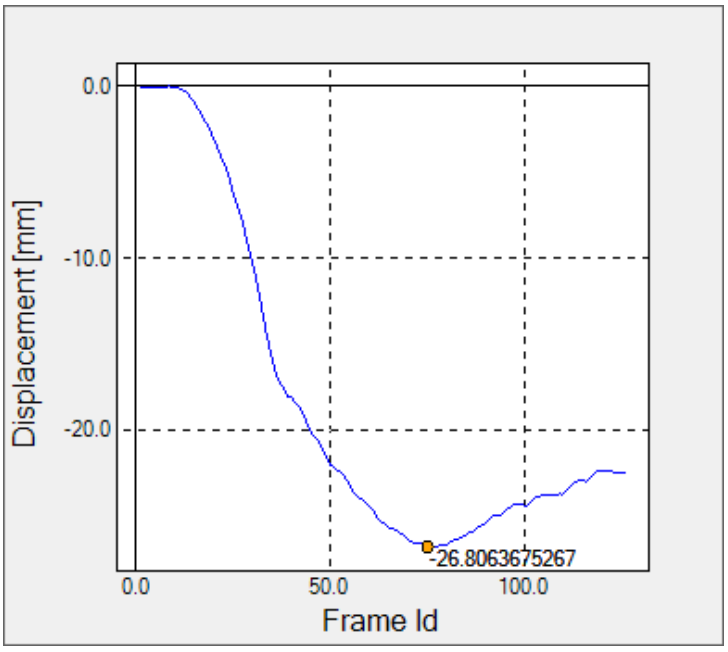

Figure 45: Mid-node displacement DIC-analysis of 20 bar

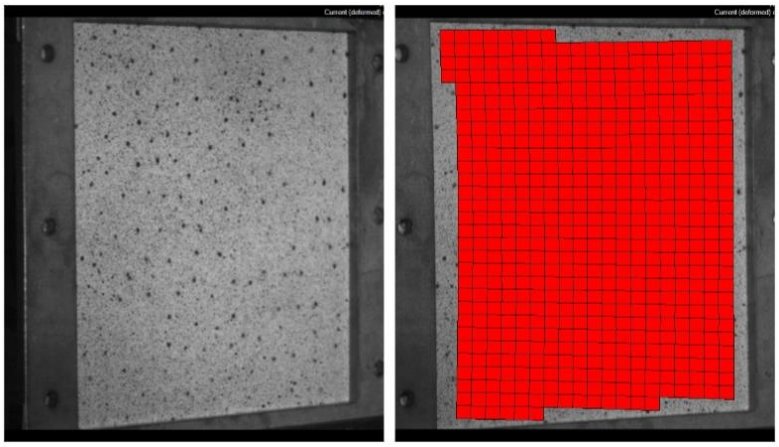

(a) Frame Id = 1

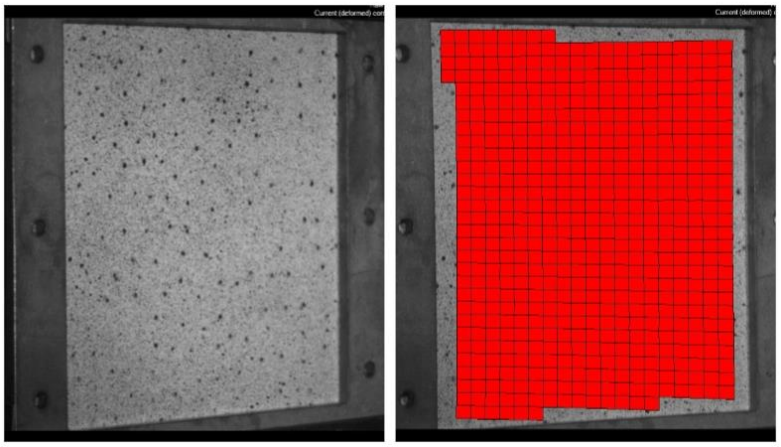

(b) Frame Id = 21

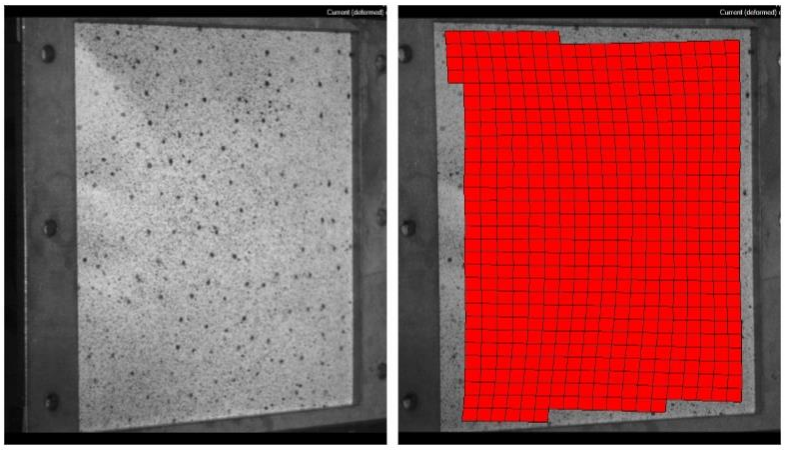

(c) Frame Id = 42

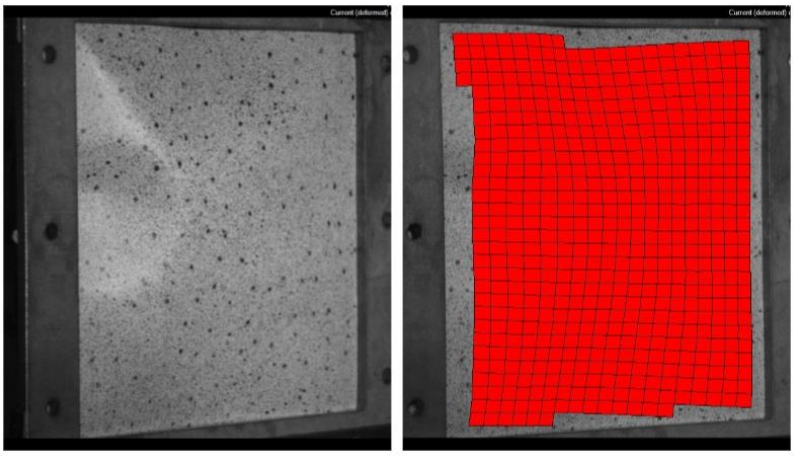

(d) Frame Id = 63

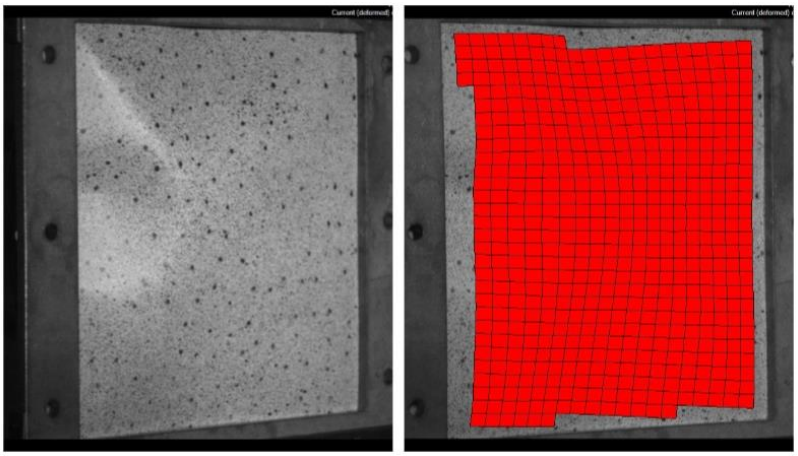

(e) Frame Id = 94

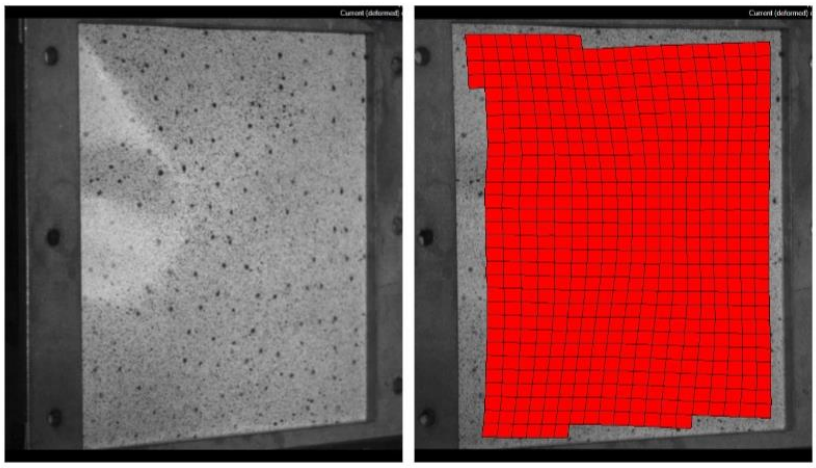

(f) Frame Id = 126

Figure 46: Mesh displacements 20 bar - DIC

10 bar with DIC:

Figure 47: Deformed plate - 10 bar

The maximum displacement for the mid-node of the 10 bar test plate is shown in Figure 47, and the DIC-analysis resulted in a total deformation of 9.4 mm. In the DIC-analysis large displacement values is also noticeable in the *positive* direction, describing that the plate bent backwards towards the air pressure after the initial deformation. When viewing the actual plate it can be seen that the displacement is the opposite of the DIC-analysis. However, further investigation reviled that the recording of the experiment stopped too early to capture the entire displacement history of the plate. The cameras only recorded 0.06 seconds, while loading recorded by the pressure transducers during the calibration in section 5.1.1 lasts for 0.2 - 0.3 seconds.

When viewing the mesh displacement during the DIC-analysis, it can be seen that some elements disappeared during the analysis. This happened because the software was unable to distinguish the gray-scale value from one element to another, as described in section 2.2.6. The cause of this is the lack of a distinct enough painted pattern in that area.

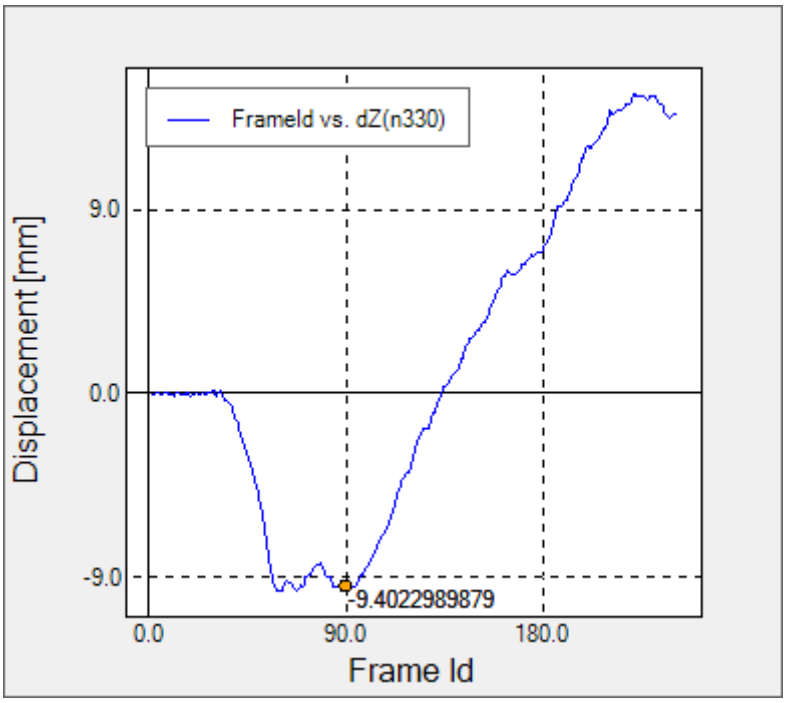

Figure 48: Mid-node displacement DIC-analysis of 20 bar

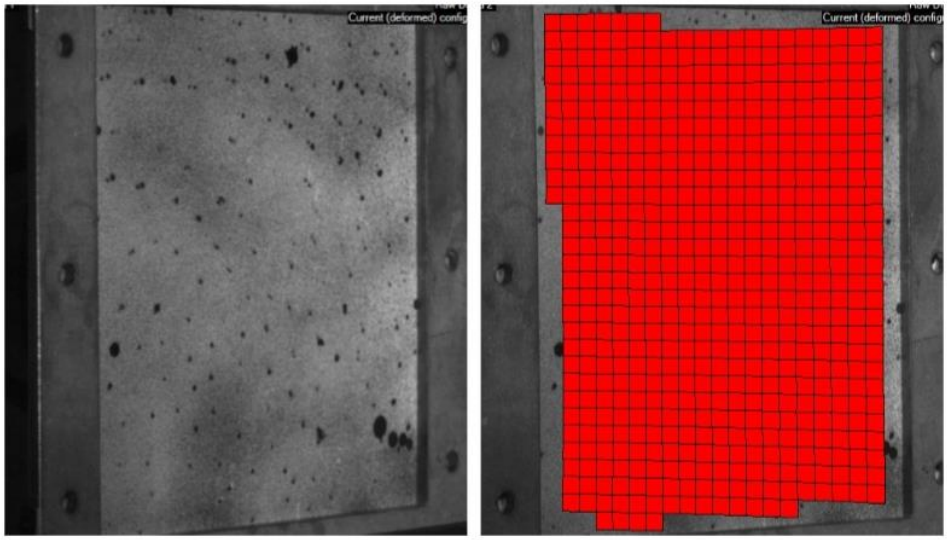

(a) Frame Id = 1

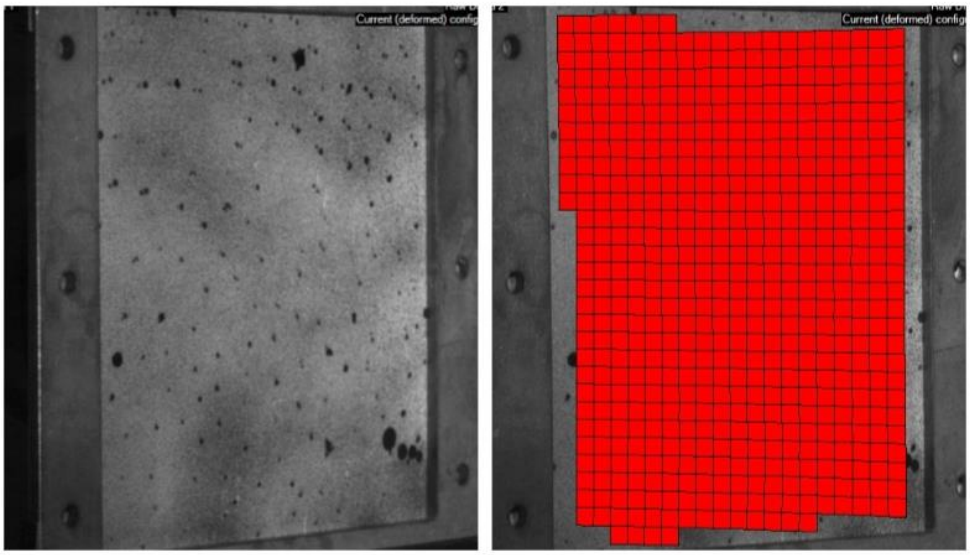

(b) Frame Id = 40

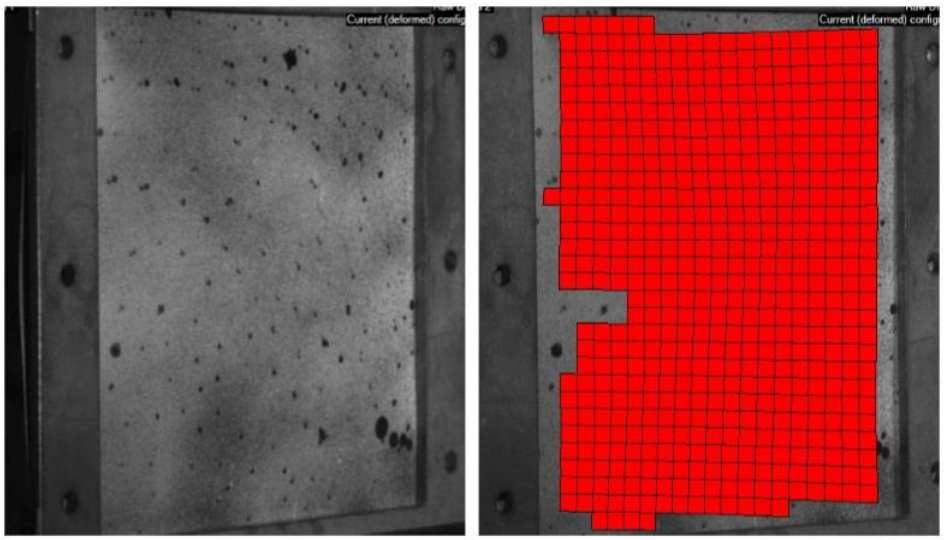

(c) Frame Id = 80

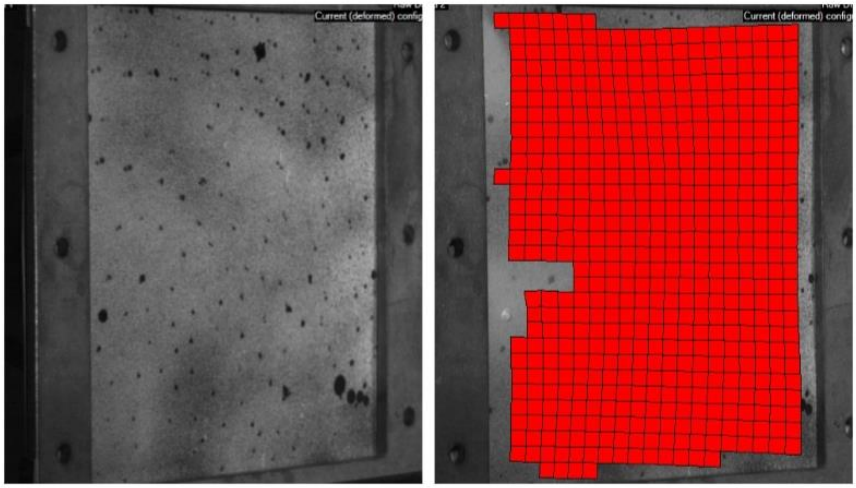

(d) Frame Id = 120

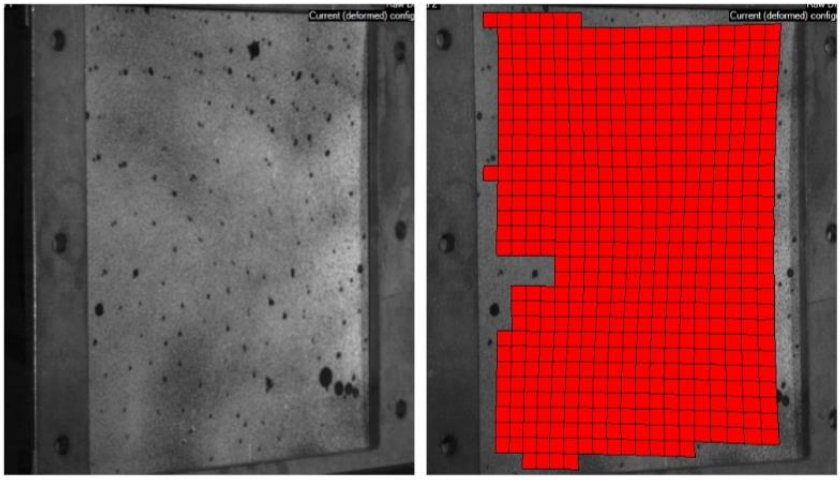

(e) Frame Id = 160

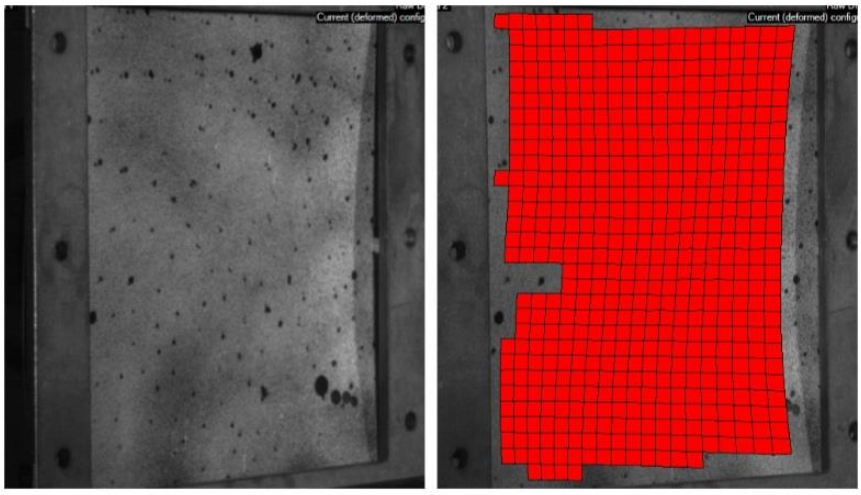

(f) Frame Id = 200

Figure 49: Mesh displacements 10 bar- DIC

In both tests, asymmetric deformation is noticeable, with a local buckle curve on the top side of the plate.

20 bar with diamonds and slits:

The experiments with diamond-shaped holes and slits showed similar displacement as the experiments with non-penetrated plates. When measuring the displacement manually with a caliper the results are 27mm for the plate with slits and 24mm for the plate with diamond-shaped holes.

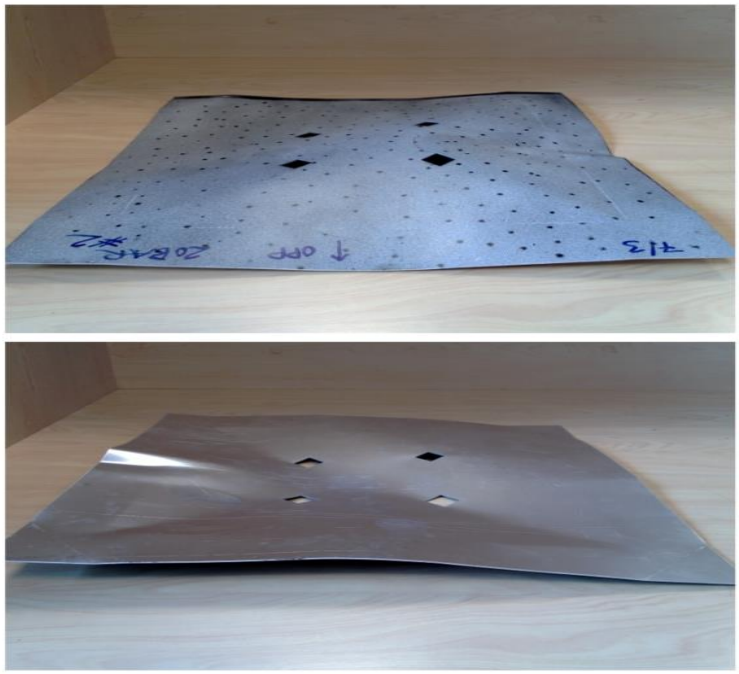

Figure 50: Deformation of plate with diamonds - 20 bar

Figure 51: Deformation of plate with slits - 20 bar

5.3 Discussion

The deformation of the test plates was assumed symmetric. For a perfect symmetric load, it is expected to get a symmetric deformation pattern. However, in the current experiment, an asymmetric tendency is evident. The displacement is largest on the side of the center, and in addition to this, a buckled fold is appearing on the left side of the plates. This shows that local buckling has occurred, caused by asymmetric loading, and that the stresses have gathered in the area where yielding occurred first.

DIC is a well-suited tool for extracting the deformation pattern of these types of experiments in 3D, yet the success of the method depends on correct preparations, such as calibration and adjustments of the cameras and whether the painted pattern on the plate are distinct enough so that the software is able to assign gray-scale values to the entire plate. In the 10 bar DIC-analysis, some elements in the mesh are lost because of lack of distinct painted pattern in that specific area.

The 10 bar results describe that the plate is bent backwards toward the pressure after the initial deformation. This differs from the actual plate deformation because the camera recording was stopped to early. The entire loading occurs over a period of 0.2 seconds, while the camera stopped after 0.06 seconds.

As stated by Rakvåg [2], the gas gun is not well suited to simulate blast loading, and the current experiments are supporting these statements. The pressure-time history obtained from the pressure transducers does not resemble that of a real explosion [13] as described in section 2.1.1.

The actual loading that hits the plate is significantly lower than the pressure in the pressure tank. This applies to both Rakvåg [2] and to the experiments in this thesis, though the current results are about 100kPa lower than those Rakvåg stated. This is caused by the funnel. The funnel that was meant to increase the response by leading the air flow directly to the plate seems counterproductive, as it decreases the response on the plate, as described in 5.1.1. Further modification of the gas gun is necessary to establish a good model of real blast loading.

6 Numerical analyses with LS-DYNA

In order to control-calculate the load curves from the plate testing in chapter 5, a numerical analysis of the experiment was carried out. The analyses were done in LS-DYNA and are Lagrangian. Since DIC could only be applied on the experiments carried out at 10 and 20 bar, the emphasis of the numerical analyses were placed on these loads.

Examples of the keyword files used in LS-DYNA with the load curves can be found in the appendix.

6.1 Numerical Model

The aluminium plate was modeled with shell elements with the size 5 mm while the loose clamps were modeled with volume elements of the same size. In the preliminary study the plate was modeled as a quarter of the actual plate using the double symmetry condition of the experiment, but as the plate experiments showed that the deformations were asymmetric (Fig. 43), the decision was made that the entire plate was to be modeled (Fig. 53).

In order to use the load curves acquired from section 5.1.1, the plate was modeled as six different parts and each assigned a load curve (Fig. 52). The different colors indicate that the parts are loaded by different load curves. Part 1-5 are loaded with the load curves acquired from sensor 1, 2, 3, 4 and 6, while part 6 is the part of the plate that is behind the frame so that part was given no loading. The load curves used are the filtered data.

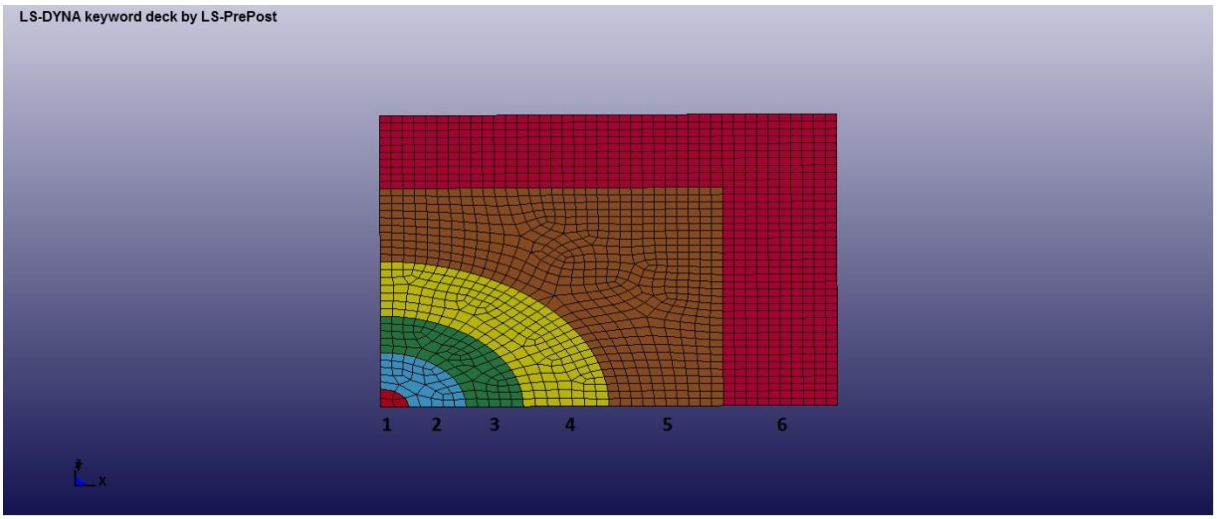

Figure 52: Sectioning of plate

Because the sensors registered up to 500 000 values from the pressure calibration, the numerical analysis would be quite time consuming if all of these where used. To solve this, 100 values were extracted from the filtered data in the interval 0 - 0.2 seconds. The plates were loaded using the *DEFINE_CURVE card.

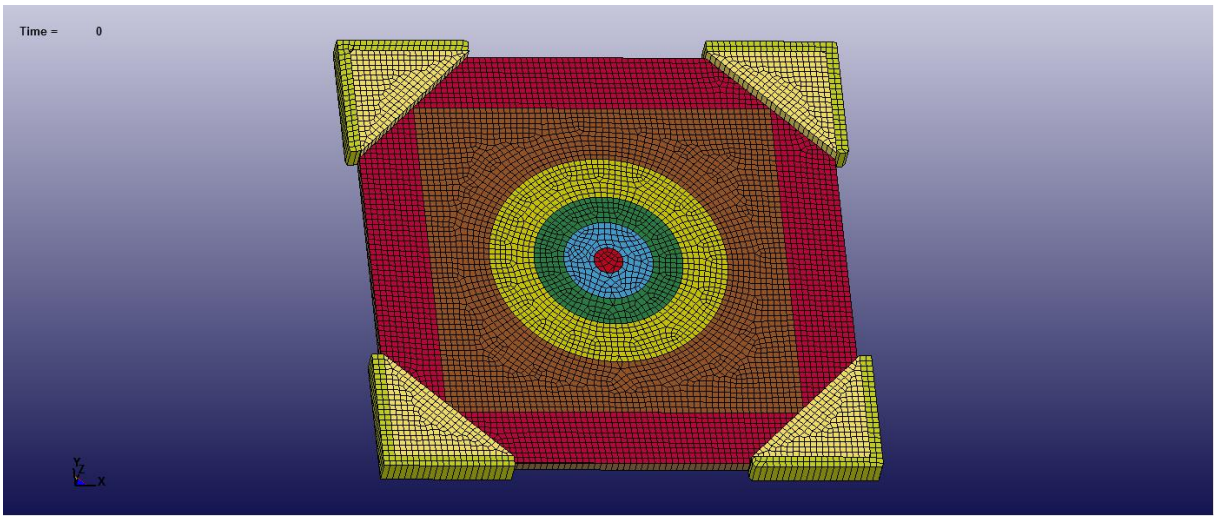

Figure 53: Numerical model of the full frame

The material model used for the aluminium plate is the modified Johnson-Cook, and in LS-DYNA this is represented using the *MAT_107 card:

Table 6: Material card *MAT_107 -1050A-H14

```
$     MID       RO        E        PR      BETA       XSI        CP     ALPHA
        1 2700.0000 7.1000+11 0.3000000 0.0000000 0.9000000  899.0000  1.5000-004
$   E0DOT        Tr        Tm        T0     FLAG1     FLAG2
 1.00000-3 293.00000  922.0000 293.00000 0.0000000 1.0000000
$        A         B         N         C         m
 0.97000+8 0.00000+0 0.0000000 0.0140000 1.0000000
$       Q1        C1        Q2        C2
 22.520,1613.1,5.9553,483.84
$       DC        WC
 1.0000000  5.4140+8
$       TC      TAUC
 829.0000 1.0000+20
```

The frame and the loose clamps were modeled as rigid materials using the *MAT_RIGID card and the parameters for steel:

Table 7: Material card *MAT_RIGID – steel

```
$     MID       RO        E        PR
5 7850.0000 2.1000+11 0.3000000
1, 7, 7
```

6.2 Results

The results from the simulations gave fairly accurate results when comparing the mid-node displacement and physical appearance to the results from the DIC-analysis. The simulation of the experiment with a loading of 10 bar closely resembled the actual deformation (Fig. 54), while the simulation of 20 bar differed substantially and the numerical model had to be modified to get results that resembled the experiments. For comparison with the DIC analysis the displacement histories of the mid-nodes were used.

6.2.1 10 bar

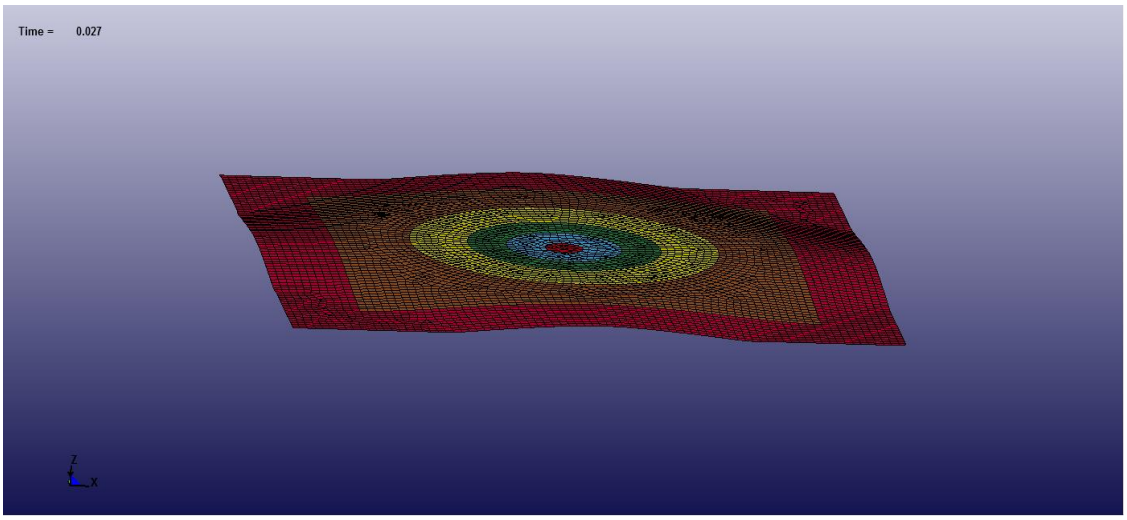

Figure 54: Deformed plate - 10 bar

When comparing the mid-node displacement of the model in LS-DYNA to the displacement depicted by the DIC-analysis it is apparent that the recordings from the high-speed cameras were stopped to early. The recordings only managed to capture the deformation up to 0.06 seconds and do not show the entire displacement history of the plate in LS-DYNA (Fig. 55) which lasts about 0.2 seconds.

When only simulating the same time-period as the DIC-analysis, the displacement history of the plate looks quite similar (Fig. 56). However, when the simulation has run its full term it is evident that the plate fluctuates when hit by the pressure, and the end displacement history looks more like the displacement from the actual experiment. The biggest difference seems to be that in the numerical analysis the load is symmetric and is applied from the center of the plate, while in the actual experiment the load seems to be asymmetric and the pressure seems to hit the plate off center as shown in section 5.2.

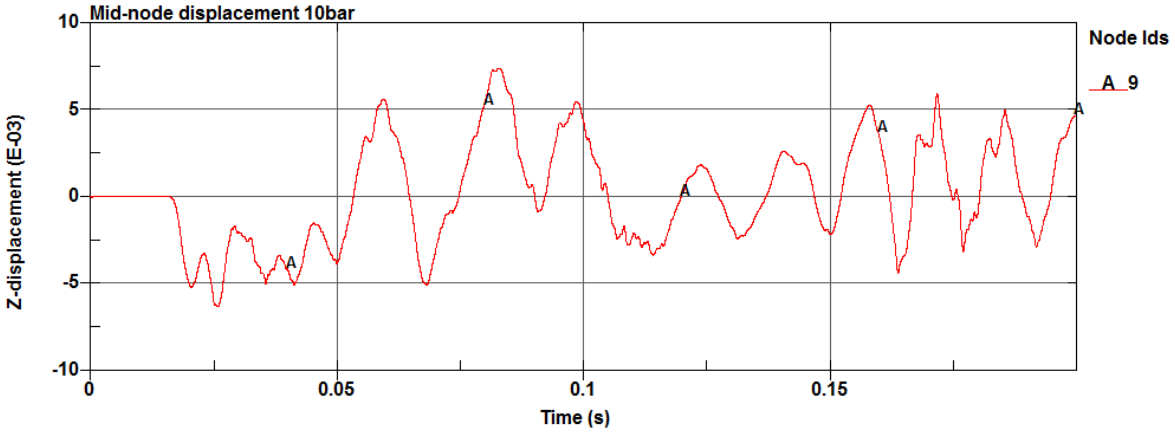

Figure 55: Mid-node displacement - 10 bar

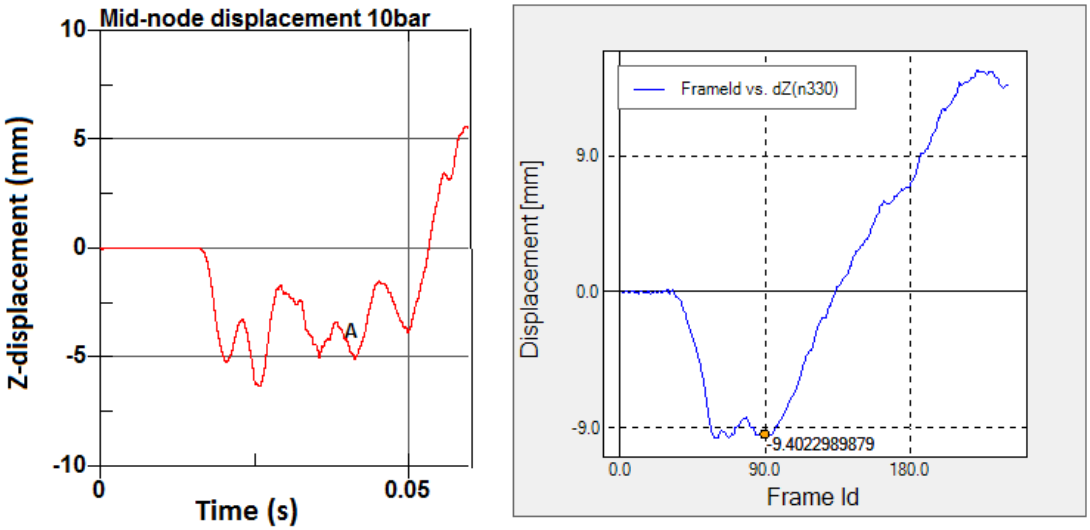

Figure 56: Mid-node displacement comparison between LS-DYNA (left) and DIC (right)

The displacement of the mid-node in the numerical analysis in LS-DYNA has a negative value of 6mm after 0.025 seconds before the plate bends the other way and the displacement ends up at around 7mm after 0.075 seconds. The DIC-analysis had a maximum negative value of 9.4mm before the plate deflects the other way and ends up at 12.6mm (Fig. 56).

6.2.2 20 bar

The numerical simulation of the experiment with a load of 20 bar differed substantially from the actual experiment when using the load curves from the pressure sensors. In the simulation the plate deformed upwards on the z-axis towards the air flow (Fig. 57), while in the experiment the plate deformed downward away from the air flow (Fig. 44).

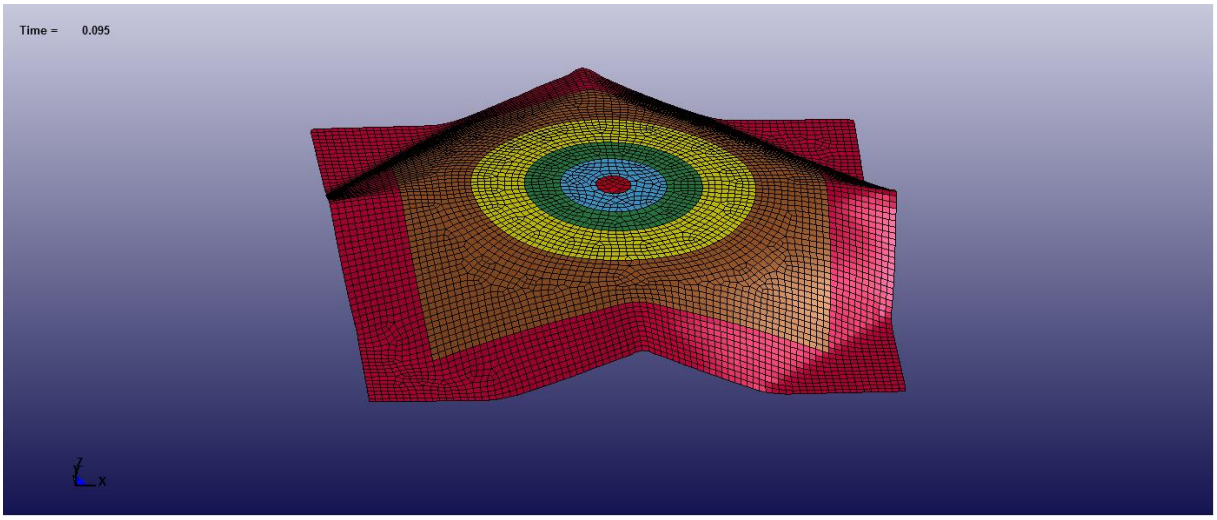

Figure 57: 20 bar - load deformation

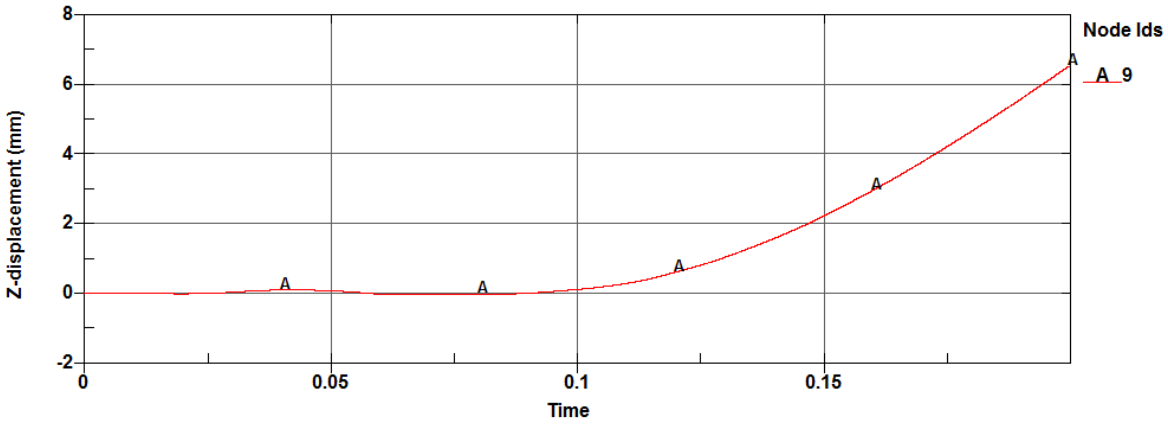

Figure 58: Mid-node displacement - 20 bar

There could be several reasons for the difference in displacement history: The pressure sensors could have had an error when recording the calibration, or the averaging algorithm in

Matlab combined with only using 100 values from each sensor could have led to a loss of values for the peak pressure.

Also, the area in the numerical model representing sensor 6 is rather large compared to the other areas. The data from sensor 6 has negative values so they will lead to a substantial force pulling in the opposite direction than the other parts. It is possible that the data from sensor 6 is only representable for a small part of the plate and not for the entire part 5, so a simulation without any load applied to part 5 was conducted to see how big a difference it made (Fig. 59).

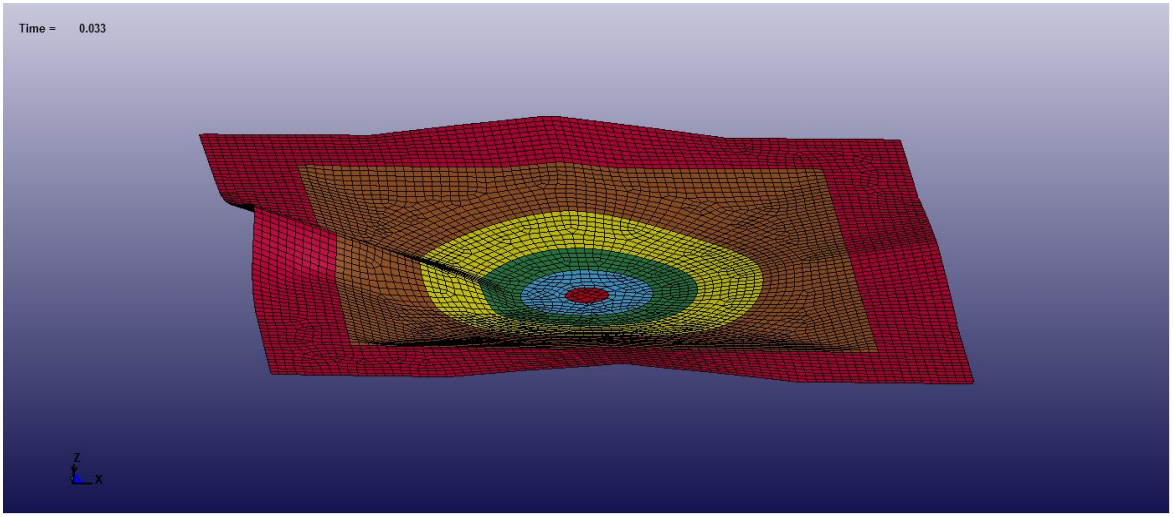

Figure 59: 20 bar - reduced load deformation

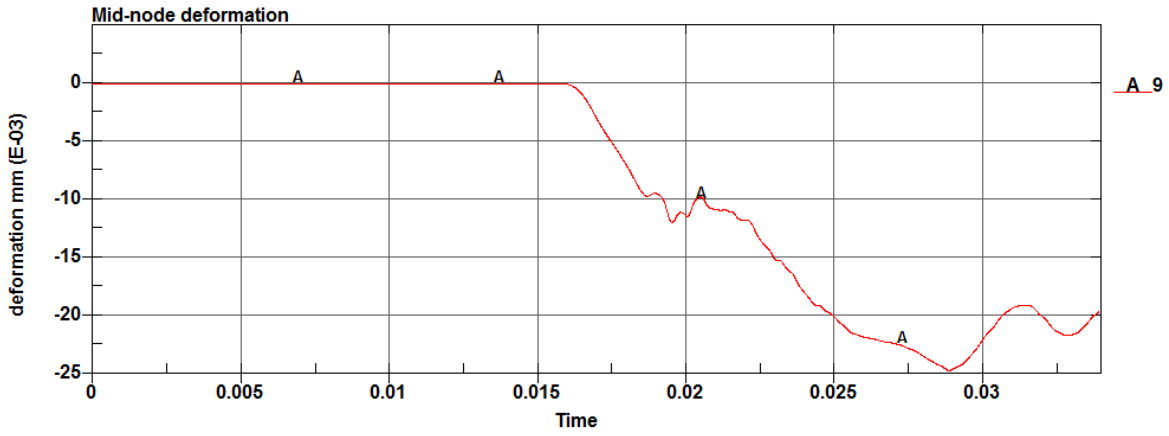

Figure 60: Mid-node displacement - 20 bar - reduced load

Figure 62 shows that the deformation of the plate looks quite similar to the actual plate deformation (Fig. 61). Just like the actual plate the buckling has mostly localized in a fold on the left side of the plate (Fig. 63).

Figure 61: Deformed plate - 20 bar - from different angles

The mid-node displacement of the numerical analysis (Fig. 60) has a maximum displacement of 25mm after about 0.028 seconds. This is very close to the mid-node displacement extracted from the DIC-analysis (Fig. 62) which was 26mm.

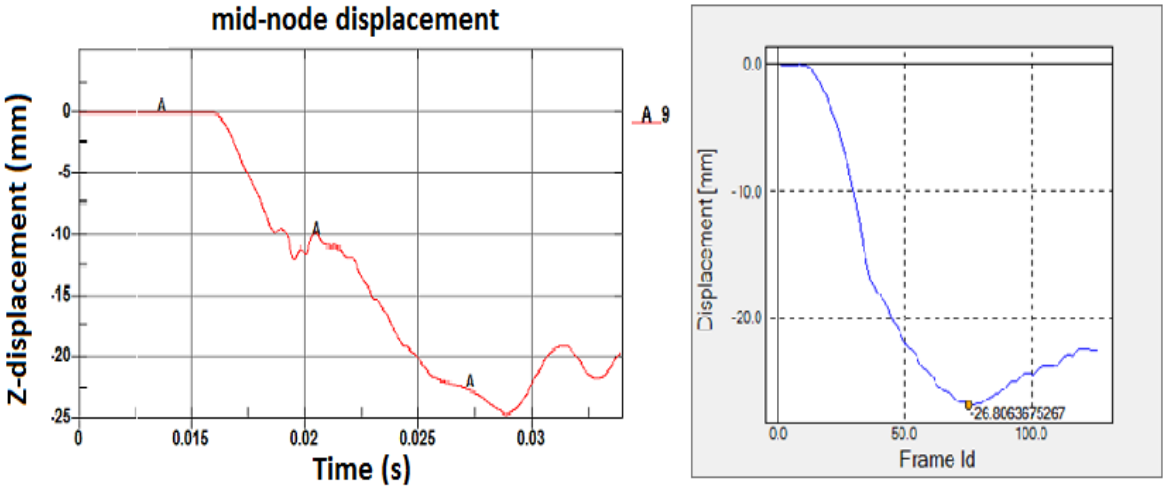

Figure 62: Mid-node displacement - comparison of LS-DYNA (left) and DIC (right)

Figure 63 shows where the plastic strain occurs and the values are largest in the buckle on the left side of the plate.

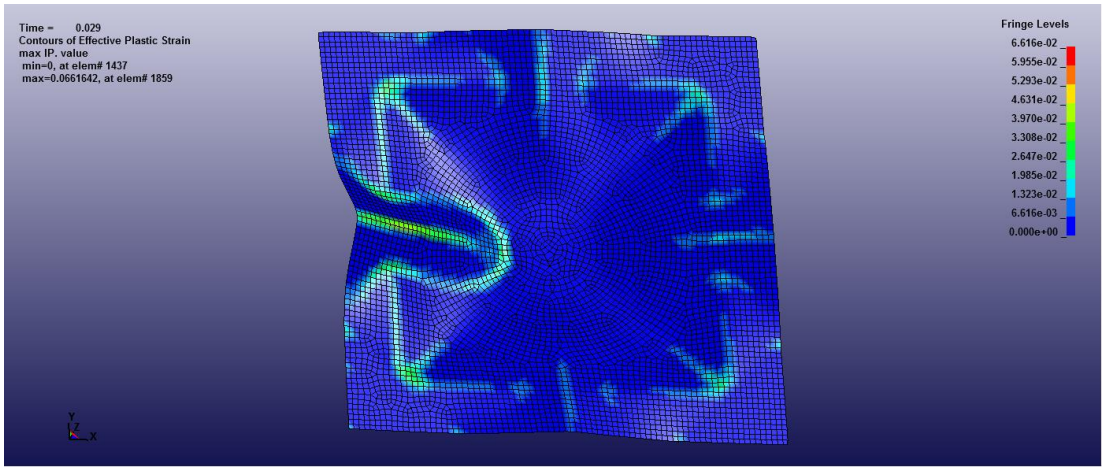

Figure 63: Plastic strain - 20 bar - reduced load

Both the deformation of the numerical plate and the mid-node displacement seems to suggest that the data from sensor 6 is not representable for the load that is actually working on part 5 of the simulation and that the resultant force in this part is close to zero.

6.3 Discussion

The numerical simulations in LS-DYNA differed slightly from the actual experiments and the values obtained from the DIC-analysis. This is especially evident in the 20 bar simulation, where the numerical plate deforms the opposite way of the plate in the actual experiment. The 10 bar simulation resembled the actual plate more closely, and the differences in the displacement history between the numerical analysis and DIC could be accounted for by the fact that the load appears to be not symmetric and that the recording used for the DIC-analysis did not cover the entire time-span of the impact.

When simulating the 20 bar experiment without the load curve from sensor 6 the result resembled the actual deformation, this suggests that the resultant force in part 5 is close to zero. This also suggests that the loading on the plates were asymmetric, and that it would have been interesting to have pressure sensors on the whole plate instead of only in ¼ of the plate as shown in section 5.1.1.

It is evident that simulating the load from the gas gun with each sensor assigned to a part of the plate, does not give an accurate result for all loads. The pressure that hits the plates in the actual experiment seems to hit off center, and vary considerably over the area. To assume that the resultant pressure in part 5 is close to zero seems to be a good approach when simulating the experiment.

7 Numerical analyses with IMPETUS Afea

IMPETUS Afea uses a unique particle method to simulate high explosives [22], as described in section 2.2.

In the gas gun experiments *pressure load* was been measured on the plate. To establish a similar loading condition in IMPETUS Afea, the pressure values have to be converted into high explosives values, for instance the amount of TNT at a certain distance. The tool used to conversion, was the IPhone App, *Blast Calc*, established by CMV Technologies, LLC [58][59]. Blast Calc is an alternative to ConWep [6], used by Rakvåg.

A crucial problem with the gas gun experiment is the fact that the combination of pressure load and impulse is unrealistic for a real blast load, and it is very different from the Friedlander equation described in equation (2.1). The thin barrel of the gas gun increases the time span of the air flow, while the funnel is reducing the initial peak pressure. This corresponds to Rakvåg [2], stating that the existing gas gun is not suited to simulate blast loading. The only way to establish a similar loading situation in IMPETUS Afea is by using an unphysical large amount of TNT at a large distance, demanding an extremely large amount of particles in order to hit the plate, which is very computational expensive to simulate in IMPETUS Afea. Running an analysis of this magnitude on the cluster at SIMLab was tried out, but in this thesis it was experienced several difficulties when running laborious analyses, and running the simulations on the cluster was not successful. The asymmetric loading condition on the plate is also causing difficulties simulating the experiment numerically as described in chapter 6. Therefore, the gas gun experiments will not be simulated in IMPETUS Afea.

Instead there will be performed a parameter study in IMPETUS Afea with a more realistic amount of TNT at a suitable distance, in order to determine how the different numerical parameters in IMPETUS Afea impact the response of the aluminium plate 1050A - H14. The response in IMPETUS Afea will be compared to a similar numerical simulation in LS-DYNA.

The dimension of the plate is 400x400x1 mm. The material parameters of the plate used in these analyses is the 1050A – H14. The explosives used in all the analyses have a mass of 7.3

kg TNT, and are placed at a distance of 1.9 meters from the plate. In the parameter study it will be focused on mesh sensitivity, geometry of the explosive charge, and the total number of particles used in the model.

The material model used in the numerical simulation is the Johnson-Cook material model. Temperature effects are not included in the analysis, because it is assumed that because of the strain rate, temperature will not affect the results significantly.

Examples of the keyword files used in this chapter can be found in the appendix.

7.1 Mesh sensitivity study

IMPETUS Afea uses volume element formulations, and the cubic 64-noded hexahedron elements have been chosen for these analyses, to provide sufficient accuracy in plasticity [26]. The higher order elements are more computationally expensive, but elements with a lower polynomial order than three, may express a too stiff plastic behavior [26]. A spherical charge is used in the mesh-sensitivity study.

The distance between nodes for each mesh is shown in Table 8:

Table 8: Meshes used in the mesh sensitivity study

	1	**2**	**3**	**4**
Mesh	6 x 6	16 x 16	30 x 30	40x40
Element size [mm]	66.67	25	13.33	10
Distance between nodes [mm]	22.22	8.33	4.44	3.33

The element division is shown in Figure 64:

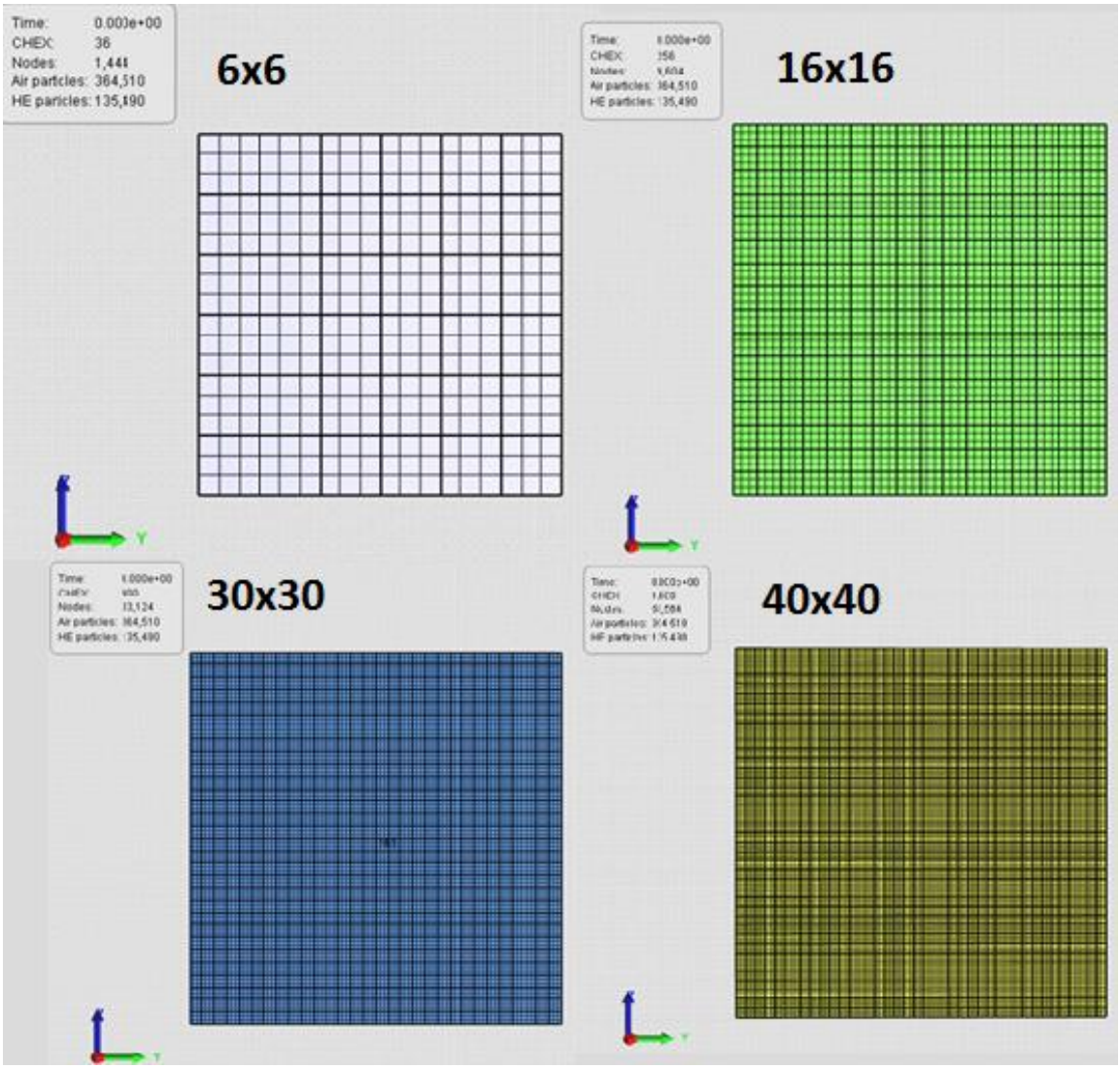

Figure 64: Element division of different meshes

The deformation of the 1050A-H14 plate is shown in Figure 65:

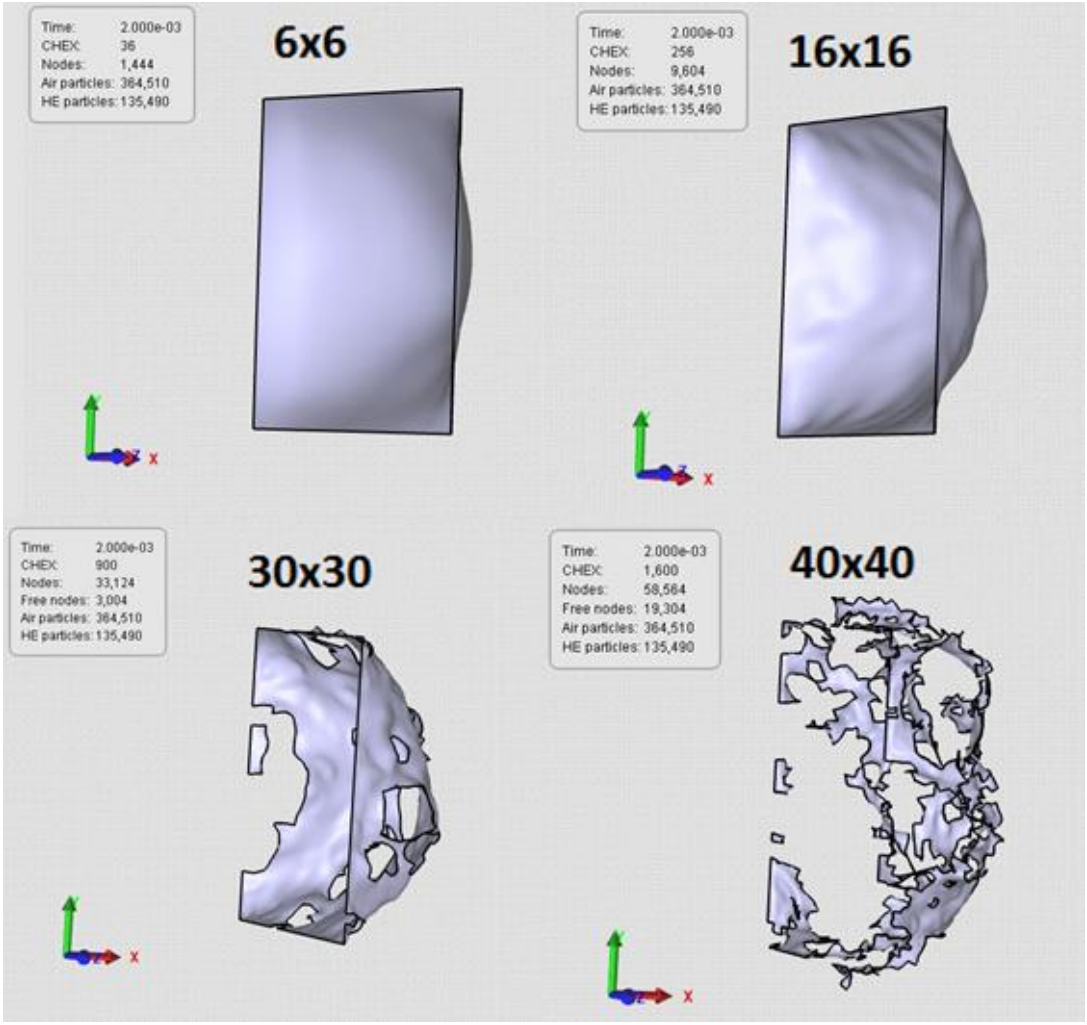

Figure 65: Deformation for different meshes

The out of plane displacements for the mid nodes in each analyses are shown in Figure 66:

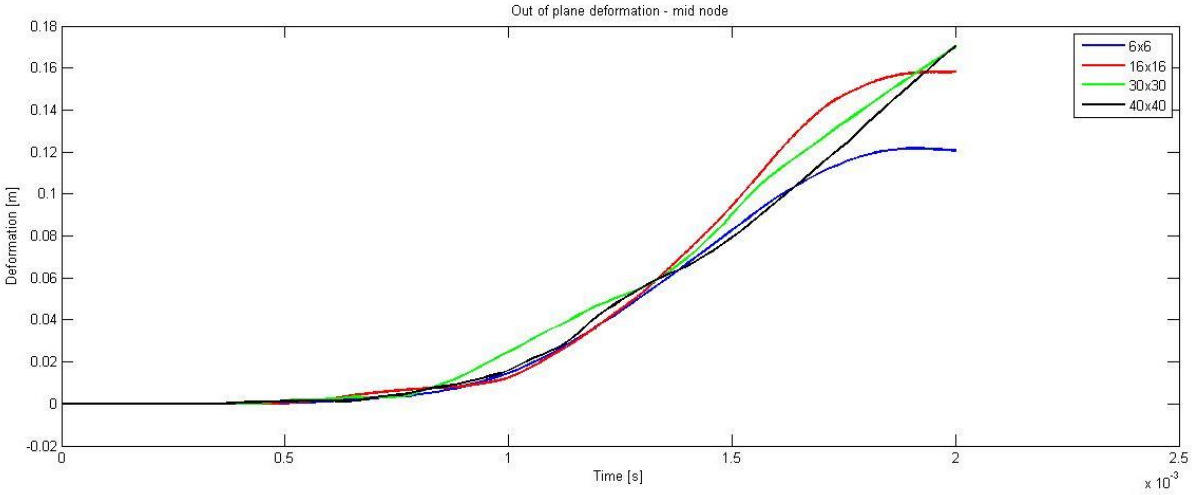

Figure 66: Mid-node displacement on aluminium plate for different mesh

A finer element division will describe the deformation more accurate, and it is evident that the 30x30 and 40x40 meshes describe a different deformation path than the 6x6 and 16x16 meshes. It seems like the 30x30 mesh division is a minimum requirement to describe the failure mode in a correct manner. The plate is torn to pieces (Fig. 65), but this effect does not occur when simulating the 6x6 and 16x16 meshes.

The internal and kinetic energy for the plate are given in Figure 67:

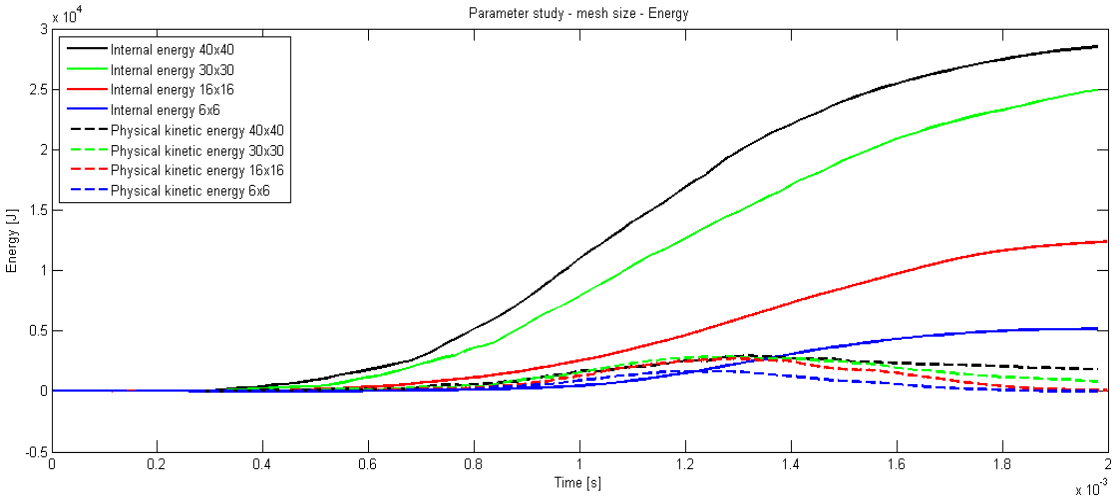

Figure 67: Energies for various meshes

A finer mesh division gives an increase in internal energy, while the kinetic energy is about at the same level. There are signs of convergence, and there seems to be little to gain by using even finer meshes.

Table 9: Elapsed time for the analyses with different mesh

	6x6	**16x16**	**30x30**	**40x40**
[hh:mm:ss]	01:43:42	02:23:17	04:53:34	13:15:42

The difference in elapsed time for the analyses is shown in Table 9. A SIMLab-cluster at NTNU has been used for calculation. The cluster used running the mesh sensitivity study is a HP Z800 workstation Intel Xeon X5650 @ 2.67 GHz with two penta-cores [60].

The computational time may be reduced using GPU, as explained in section 2.2.5. The elapsed time for the 30x30 mesh analysis at the same cluster, using NVIDIA GPU Quadro 4000 [60] is shown in Table 10. The computational time is almost halved when using the GPU.

Table 10: Computational time of analysis running on CPU and GPU

	30x30 CPU	**30x30 GPU**
[hh:mm:ss]	04:53:34	02:34:20

The computational time (Tab. 9) for the 30x30 mesh analysis is about twice as large as for the 16x16 mesh analysis, and about 1/3 of the 40x40 mesh analysis time. A mesh division of 30x30 or 40x40 is as mentioned above necessary to describe the failure mode correctly. There seem to be little to gain in deformation by increasing the mesh division to 40x40, but there is a lot to gain in computational time by using the 30x30 mesh. Therefore, the 30 x 30 mesh is used in further analyses.

7.2 Charge geometry

IMPETUS Afea uses both high explosive (HE) – and air particles when simulating blast loading. The amount of TNT is decided by the volume of the charge [61]. TNT has a predefined density of 1630 $\frac{kg}{m^3}$ [61] and to describe an amount of 7.3 kg TNT, the charge volume has to be modeled with a value of $4.478527*10^{-3}$ m^3. But the geometry of the charge might have a great impact on the result, and a study of different charge geometries is therefore performed below. A total amount of 500 000 particles has been used in this study.

The geometries used are shown in Figure 68, Figure 69, and Figure 70.

1) Sphere

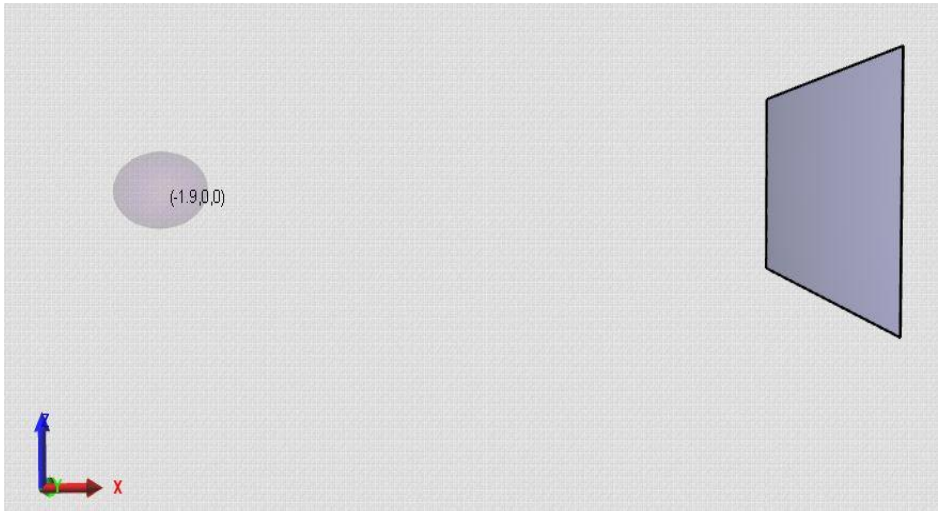

Figure 68: Spherical charge

2) Box:

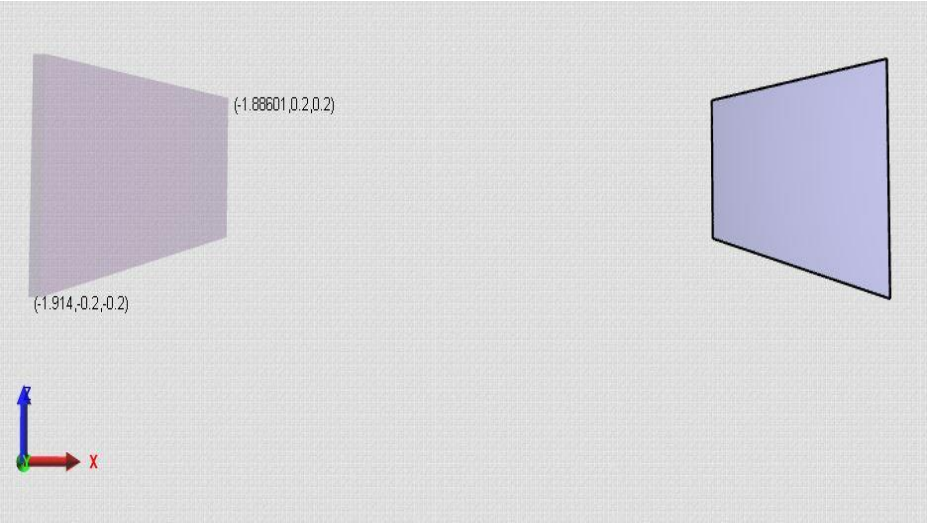

Figure 69: Box charge

3) Cylinder:

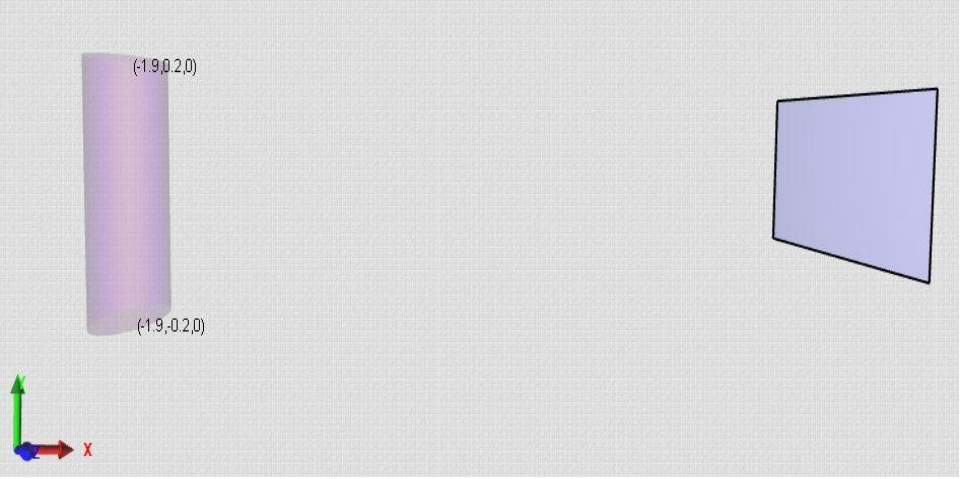

Figure 70: Cylinder charge

For a rigid plate, the impulse from high explosive particles and air particles for different charge geometries are shown in Figure 71:

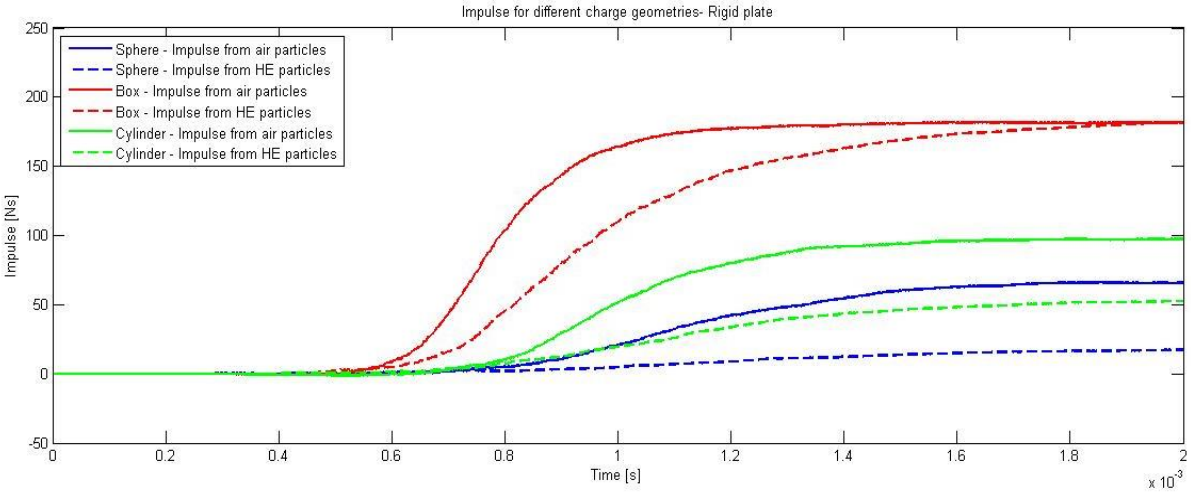

Figure 71: Impulse on rigid plate for different charge geometries

The impulse is lower for both the cylinder- and sphere-shaped charge than for the box-shaped charge, which is expected since the sphere and the cylinder will have a larger spread of high explosive particles.

For the 1050A – H14, the mid-node displacements are shown in Figure 72:

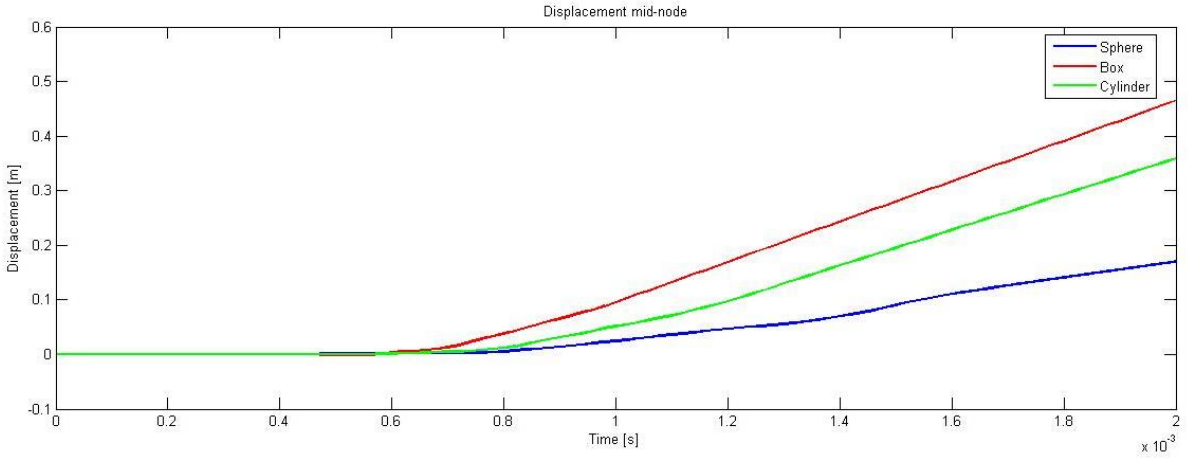

Figure 72: Mid-node displacement on aluminium plate for different charge geometries

The displacement of the aluminium plate subjected to a sphere-shaped charge is about 1/3 of

the plate subjected to the box-shaped charge. The geometry of the charge is obviously of importance to the loading situation, which coincides with the studies of Zakrisson [62].

The impulse for the 1050A-H14 plate subjected to different geometries is shown in Figure 73:

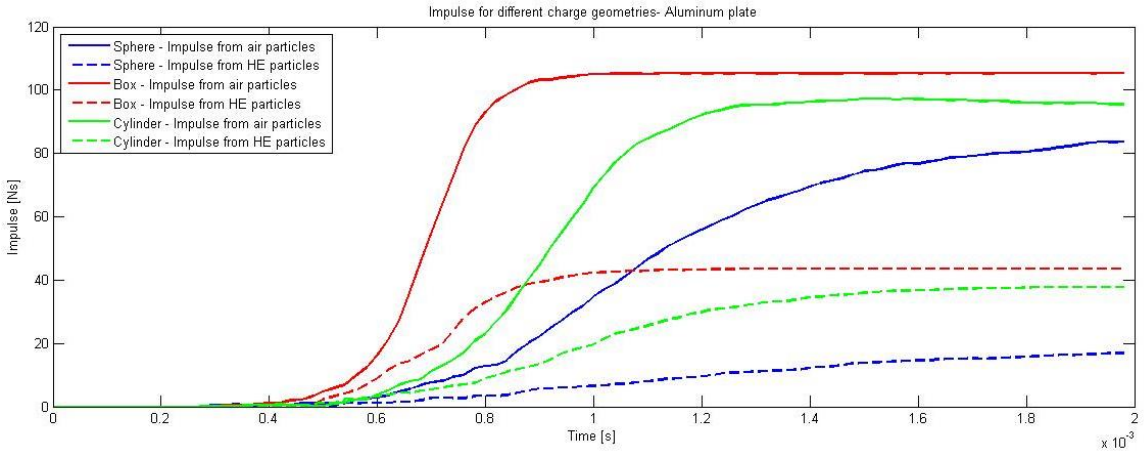

Figure 73: Impulse on 1050A - H14 plate for different charge geometries

The box-shaped charge gives larger impulse than the spherical and cylinder-shaped charges. The tendency of the blast impulse on the deformable 1050A – H14 plate is similar to the impulse on a rigid plate, but the values are lower. The impulse on a rigid plate gives a more accurate description on the loading situation on the plate, since the impulse is not affected by the plastic deformation of the aluminium plate.

7.3 Particle study

IMPETUS Afea is automatically calculating the ratio of air – and high explosive particles in an analysis. In reality, air and detonation products consist of different types of molecules. However, the air and detonation products have on average about the same molar mass. Lightweight molecules have a higher average thermal velocity than the heavy ones, described in equation (2.21) in section 2.2.4. To establish correct gas dynamics, the air particles and high explosive particles need to be given about the same particle mass. When calculating the ratio of air particles and high explosive particles, IMPETUS Afea makes sure the velocity distribution is correct, resulting in accurate gas dynamics [61].

The number of high explosive particles has been calculated to be about 27 % of the total number of particles in the current analyses. The *total* amount of particles on the other hand, is changeable. A study of the total number of 200 000, 500 000 and 800 000 particles has been performed, and presented in this subsection. A spherical charge is used in the particle study.

The deformation for different amount of particles is shown in Figure 74:

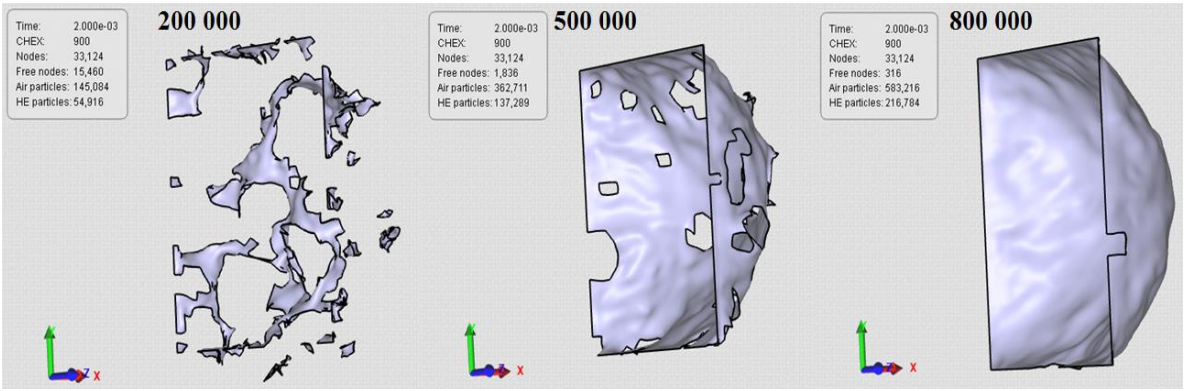

Figure 74: Deformation for a particle number of 200 000 (left), 500 000 (middle), and 800 000 (right)

It is evident from Figure 74 that the number of particles has a significant matter when it comes to deformation and impact on the plate. A higher number of particles will behave more like an evenly distributed load, since the energy is divided between many particles. A smaller amount of particles, i.e. 200 000, means more energy to each particle. The large content of energy may be enough to penetrate the plate. Another reason for this failure may be the fact that that small amount of particles causes large local deformations, reducing the incremental time step below the critical time step, as explained in section 2.2.1. The consequence is that IMPETUS Afea is eroding the elements.

This effect is also visible when comparing the mid-node displacements in Figure 75:

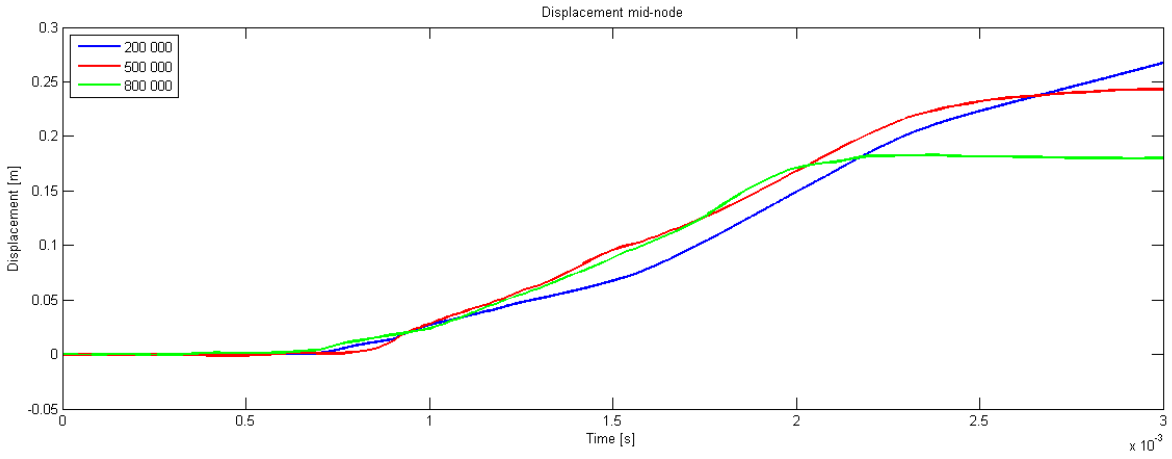

Figure 75: Mid-node displacement on aluminium plate for different amount of particles

An amount of 200 000 particles will tear the plate to pieces, and the mid-node displacement path will therefore differ from the rest of the displacement curves.

The impulse from both high explosive particles and air particles is shown in Figure 76:

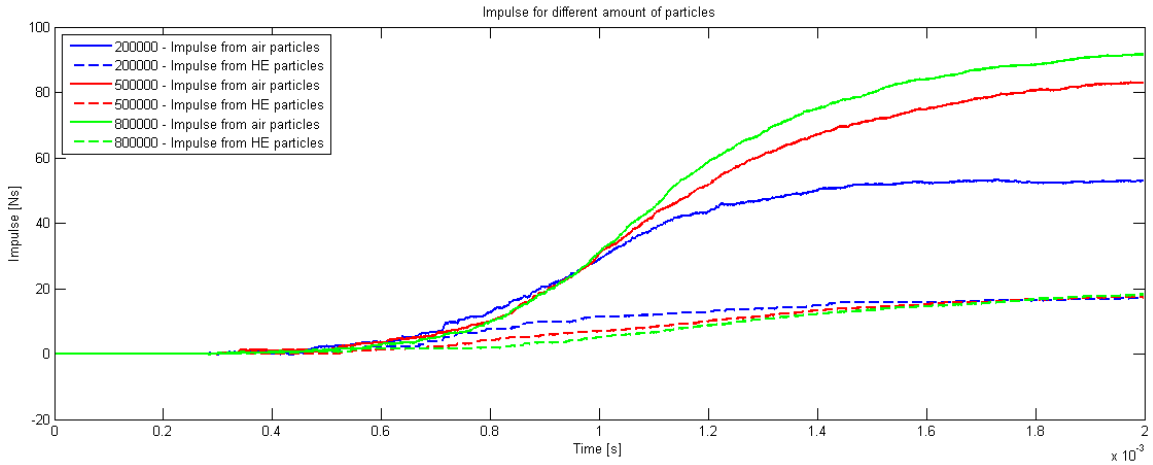

Figure 76: Impulse on aluminium plate for different amount of particles

The impulse for different amount of particles seems convergent. A small amount of particles, i.e. 200 000, describes the impulse - and displacement values inaccurately. For an amount of 500 000 and 800 000 the difference in total impulse is 9.65 Ns. There seems to be little to gain in increasing the number of particles further.

A comparison of the computational time of the particle study on the SIMLab – cluster is shown in Table 11:

Table 11: Elapsed time for analyses with different amount of particles

	200 000	500 000	800 000
[hh:mm:ss]	11:02:16	02:42:03	02:36:04

Large deformations are reducing the time step, and the analysis will become very time-consuming. This is evident for the analysis using 200 000 particles.

For a higher amount of particles the deformation is smaller as the energy is divided between many particles, as shown in Figure 74, and the elapsed time of analysis will be considerably lower. For a higher amount of particles than 800 000 it seems like the deformation of the plate is about the same, and the elapsed time of analysis will increase steadily as the amount of particles increases. For a higher amount of particles, the elapsed time of analysis is shown in Table 12:

Table 12: Elapsed time for higher amount of particles

	1 400 000	2 000 000
[hh:mm:ss]	03:34:34	05:11:02

7.4 IMPETUS Afea and LS-DYNA

The deformation pattern of the 1050A - H14 plate subjected to a blast load for IMPETUS Afea is shown in Figure 77. The charge still consists of 7.3 kg TNT at a distance of 1.9 meters, and has a spherical geometry. A 30x30 mesh with cubic 64-noded hexahedron elements are used, and the total number of particles is 800 000.

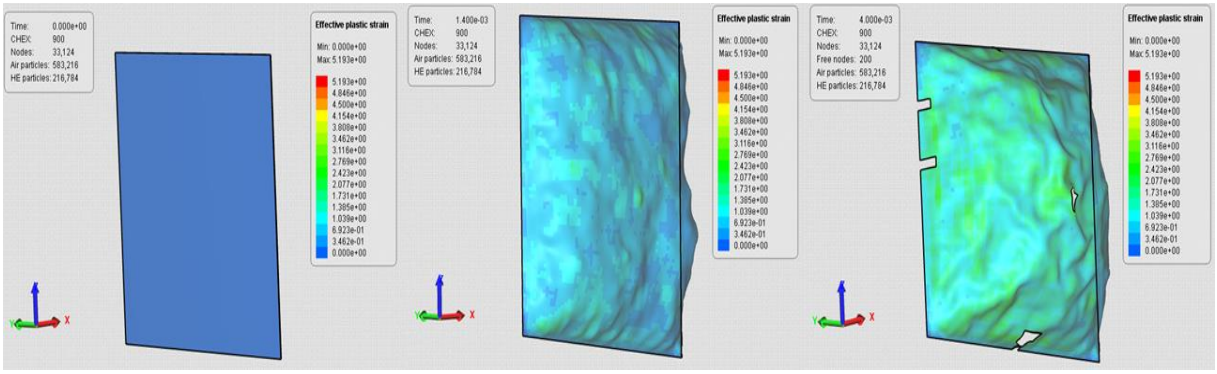

Figure 77: Deformation in IMPETUS Afea

Figure 78 shows the same simulation in LS-DYNA. The plate is fixed along the edges in both LS-DYNA and IMPETUS Afea. 5mm shell elements are used in LS-DYNA. Blast loading is implemented in the LS-DYNA model by using the *LOAD_BLAST card.

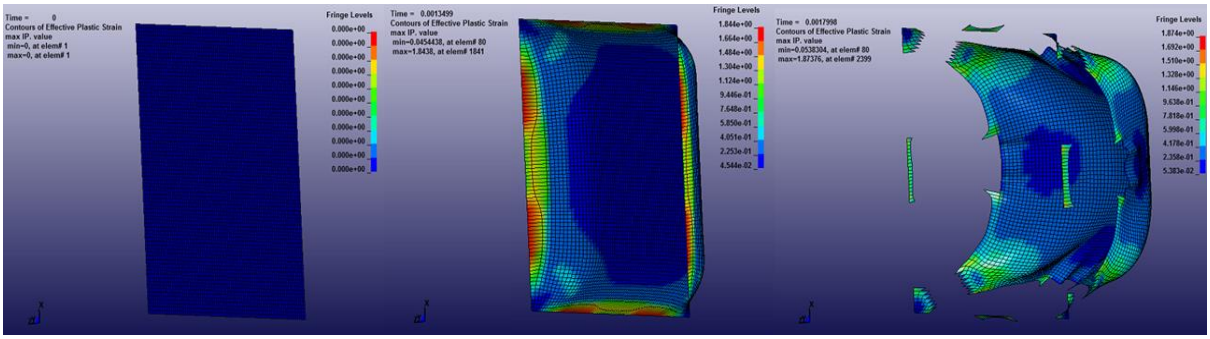

Figure 78: Deformation in LS-DYNA

The IMPETUS Afea model extracts a failure mode similar to the failure mode I described in section 2.1.3, while LS-DYNA extracts failure mode IIa.

Examples of the keyword files for the LS-DYNA simulation of blast loading can be found in the appendix.

7.5 Discussion

The IMPETUS Afea software and the discrete particle approach are obviously including some effects that LS-DYNA does not. In IMPETUS Afea, particles will tear out pieces from the aluminium plate if the amount of particles is low, and the displacement pattern as well as the impulse will therefore differ a lot from the LS-DYNA model. The failure seen in IMPETUS Afea is not seen in LS-DYNA. The fact that IMPETUS Afea exclusively uses volume elements instead of shell elements is also of importance to the results.

It is interesting to see how large impact the amount of particles has on the results. A larger amount of particles gives a smoother deformation and less failure, since the energy is divided between many particles.

When it comes to the explosive charge, the box geometry gives a lower spread of particles than the cylinder and spherical geometry, and will therefore give a larger impulse and deformation on the plate. It is interesting to see how important the geometry of the charge is to the loading situation, and this coincides with the studies of Zakrisson [62].

The solution method in IMPETUS Afea is based on explicit time integration, described in section 2.2.1. For a small amount of particles, large local deformations will happen, and the time step will be reduced quickly, as defined in equation (2.12). It may be speculated that when the time step is reduced below the critical time step for the smallest element length in the model, elements will be eroded in IMPETUS Afea. This may be a numerical technique to avoid computational expensive elements, or to avoid the issue with negative mass caused by large deformation, explained in section 2.2.3.

It was experienced several difficulties with an unstable cluster when running laborious analyses, i.e. sudden shutdowns with a corrupted analysis as outcome. It is uncertain if these problems were caused by the cluster or the IMPETUS Afea software.

When increasing the amount of particles and decreasing the element size, which was necessary to establish accurate results, the computational time increased significantly. Though, the elapsed time of running an analysis was almost halved when the GPU was used.

IMPETUS Afea was unable to reproduce the correct load curve obtained from the experiments in chapter 5, and was therefore not suited to simulate the gas gun experiments.

It is evident that the particle based approach in IMPETUS Afea is not suitable simulating long-range blast loading, but it seems to be suitable simulating close-range blast loading.

8 Concluding remarks

- The need for lightweight blast protective materials is increasing. This has led to the increased search of alternative materials to use instead of traditional concrete structures. Aluminium and steel seem like good alternatives and more research into the behavior of these materials subjected to blast loading has been conducted.

- New finite element software is being developed to better simulate the effects of blast loading. IMPETUS Afea is an example of such a software program and uses the Corpuscular method.

- A Lagrangian analysis in LS-DYNA of the experiments conducted with the gas gun, gave results with varying degree of accuracy. The simulation of the 10 bar load resembled the actual experiment quite good, but the 20 bar simulation had to be modified to get the same deformation as the gas gun experiment. It seems that the loading applied from the gas gun is asymmetric and varies over the plate. Because the pressure transducers were placed on only $1/4$ of the plate, they did not obtain the actual load distribution, and the numerical analysis showed that these values were not representative for the loading that occurred on the entire plate

- The aluminium plates with diamond shaped holes and slits showed similar behavior as the plates without holes.

- IMPETUS Afea with the particle based approach seems to be a good method to simulate blast loading, because it includes effects that LS-DYNA does not. IMPETUS Afea is very sensitive to mesh size, amount of particles and the geometry of the explosive charge. When simulating the same experiment in IMPETUS Afea and LS-DYNA, using shell elements and a Lagrangian approach in LS-DYNA, it is apparent that IMPETUS Afea is considerably more computational expensive. IMPETUS Afea with the particle based approach is not suitable to simulate the gas gun experiments. IMPETUS Afea is not suitable for long-range blast simulations.

- Digital Image Correlation (DIC) gives an accurate description of the plate deformation and makes it easy to compare results from the numerical simulations and the gas gun experiment. It is however crucial that the pattern painted on the plates is distinct, and there is currently no standardized way of doing so.

- The 1050A - H14 material clearly shows anisotropic behavior, but numerical simulations imply that the different specimen orientations have minimal impact on the plate deformation. This makes it sufficient to use the modified Johnson-Cook material model.

- The gas gun showed good repeatability, but the load curve obtained from the experiments were not representable for a proper blast wave in terms of impulse and peak pressure. The gas gun is not suited for blast loading.

9 Further work

During the work with this thesis, light has been shed on some of the problems with blast protective materials and blast load simulation. Below is a list of suggestions for further work:

- Perform real experiments with explosives in order to collect sufficient, accurate and relevant data on the topic.
- Perform experiments with fragments.
- Use MMALE analyses to better simulate the effect of holes in the plate caused by fragmentation.
- Compare analyses done with ALE in LS-DYNA to the particle based approach used in IMPETUS Afea.
- Perform experiments with and without the funnel to investigate the effect it has on the pressure history.
- A shock tube is expected to be made completed at SIMLab at NTNU in 2013. Compare results from similar experiments conducted on the new shock tube to the results obtained with the gas gun.
- Investigate the effect of temperature on the material properties of 1050A – H14.
- Develop a standardized method to paint a distinct pattern for grey-scale values on plates used in DIC-analyses.

Bibliography

1. U.Nystrøm and K. Gylltoft., Numerical studies of the combined effects of blast and fragment loading. *International Jounal of Impact Engineering*,2009;36:995-1005
2. Knut G. Rakvåg, "Combined blast and fragment loading on plates", master thesis, NTNU, 2009
3. Department of the Army, Technical Manual TM 5-885-1. *Fundamentals of Protective Design for Conventional Weapons*. Headquarters, Washington DC, 1986.
4. L. Olovsson, A.G. Hanssen, T. Børvik, M. Langseth, «A particle-based approach to close-range blast loading». European Journal of Mechanics A/Solids, 2009.
5. T. Børvik, "*Response of structures to planer blast load – a finite element engineering approach*". Computers and Structures, volume 87, pages 507-520, 2009
6. USACE PDC. *ConWep*,: https://pdc.usace.army.mil/software/conwep/. 05.04.2013.
7. Wikipedia contributors, «*Explosion*» Wikipedia, the free encyclopedia, http://en.wikipedia.org/wiki/Explosion. 25.january, 2013
8. P.D Smith, J.G Heatherington, "*Blast and Ballistic Loading of Structu*res", Butterworth Heinemann, 1995.
9. T. Scheve, "*How Blast-resistant Clothing Works*", HowStuffWorks, http://science.howstuffworks.com/blast-resistant-clothing1.htm. 25.january, 2013
10. P.S. Bulson, "*Explosive Loading of Engineering Structures*", E and FN SPON, 1992
11. Wikipedia contributors, "*Shock Wave*" Wikipedia, the free encyclopedia, http://en.wikipedia.org/wiki/Shock_wave. 28.january, 2013
12. S.Hiermaier. *Structures under Crash and Impact*. Springer, 2008
13. Wilfred E. Baker. "*Explosions in air*". Wilfred Baker Engineering, San Antoniom, 1983.
14. S. Mannan. *Lees Loss Prevention in the process industries – Hazard Identification, Assessment and Control*. Volume 2. Third edition. Elsevier Butterworth – Heinemann, 2005.
15. S. R. Brinkley, J. G. Kirkwood. "*Theory of the Propagation of Shock Waves*". Department of chemistry, Cornwell University, Ithaca, New York. 1987

16. Kambouchev, N, Noels, L,. and Radovitzky, R. 2006, "*Nonlinear Compressibility Effects in Fluid-Structure Interaction and their Implications on the Air-Blast Loading of Structures*". J. Appl. Phys, 100, p 063519.
17. S.B Menkes and H.J Opat. "*Broken Beams – Tearing and shear failure in explosively loaded clamped beams*." Experimental Mechanics, 13:480,486. 1973
18. W.E Baker, P.A Cox, P.S Westine, J.J. Kulesz, R.A Strehlow, "*Fundamental Studies in Engineering 5 – Explosion Hazards and Evaluation*." Elsevier Scientific Publishing Company, Amsterdam 1983
19. Backmann, M.E. and Goldsmith, W. (1978). The mechanics of penetration of projectiles into targets. *Int. J. Eng. Sci.*, 16, pp. 1-99.
20. D.R. Curran. *Simple fragment size and shape distribution formulae for explosively fragmenting munitions*. International Journal of Impact Engineering, 1997;20:197-208.
21. Wikipedia contributors, "LS-DYNA" Wikipedia, the free encyclopedia, http://en.wikipedia.org/wiki/LS-DYNA (accessed 31.january, 2013)
22. IMPETUS Afea AS. *IMPETUS Afea Solver User Documentation*.http://manual.impetus-afea.com/pdf/solver/v2.0/manual.pdf. Version: 2.0.303 beta. February 16, 2012
23. E. Fagerholt. "*Field Measurements in Mechanical Testing Using Close-Range Photogrammetry and Digital Image Analysis*". NTNU, 2012:95
24. Cook, Robert D., Malkus, David S., Plesha, Michael E., Witt, Robert J., "*Concepts and applications of finite element analysis* ", fourth edition, John Wiley & Sons, INC., United States, 2002
25. Mathisen KM, lecture on eksplisitte methods, NTNU, 02.oktober 2012
26. L.Olovsson. Lecture on IMPETUS_Afea. NTNU, 12.03.13
27. Livermore Software Technology Corporation. *LS-DYNA Theory Manual*, http://www.lstc.com/products/ls-dyna, 2006
28. FEA Information Inc, *LS-DYNA Support*, available at: http://www.dynasupport.com/tutorial/ls-dyna-users-guide/time-integration. 04.05.2013
29. Belytschko, T., Liu, W.K., Moran, B., "*Nonlinear Finite Elements for Continua and Structures*". John Wiley & Sons, LTD., England, 2000.
30. Wikiversity, *Nonlinear finite elements/Lagrangian and Eulerian desciptions*, available at: http://en.wikiversity.org/wiki/Nonlinear_finite_elements/Lagrangian_and_Eulerian_descriptions (accessed 05.february, 2013).

31. L. Olovsson. "*Corpuscular method for airbag deployment simulations in LS-DYNA*". IMPETUS AFEA Technical publications, 2007. http://www.impetus-afea.com/resources/corp.pdf (acsessed 27.05.2013)
32. A.Knutsen. *Verdensledende på fysikksimulering*. http://www.tu.no/it/2010/09/21/verdensledende-pa-fysikksimulering. (acsessed 10.04.2013
33. E. Fagerholt, T.Børvik , O.S.Hopperstad. *Measuring discontinuous displacement fields in cracked specimens using digital image correlation with mesh adaptation and crack-path optimization*. Optics and Lasers in Engineering, Volume 51, Issue 3, March 2013, Pages 299–310
34. E. Fagerholt. Mail correspondence. 28.05.2013
35. B. Pan,* D. Wu,Liping Yu, *Optimization of a three-dimensional digital image correlation system for deformation measurements in extreme environment*. 2012.
36. M.Langerholc, J.Slavic, M.Boltezar: *Absolute Nodal Coodinates in Digital Image Correlation*. Experimental Mechanics, Vol 53 (5) p 807-818, 2013.
37. M.A. Sutton, S.R. McNeill, J.D. Helm, Y.I. Chao, *Advances in two-dimensional and three-dimensional computer vision*, Topics Appl. Phys. 77 (2000) 323-372
38. G. Besnard, F. Hild, S. Roux, *'Finite-element' displacement fields analysis from digital images: application to Portevin-le Châtelier bands*, Exp. Mech. 46 (2006) 789-804
39. E.Fagerholt, E. Østby, T. Børvik, O.S Hopperstad. (2012) *Investigation of fracture in small-scale SENT tests of a welded X80 pipeline steel using Digital Image Correlation with node splitting*. Engineering Fracture Mechanics. 2012; volum 96.
40. E.Fagerholt. *Field Measurements in Mechanical Testing Using Close-Range Photogrammetry and Digital Image Analysis.* NTNU. 2013.
41. F. Grytten a, T. Børvik, O.S. Hopperstad, M. Langseth , "*Low velocity perforation of AA5083-H116 aluminium plates*", International Journal of Impact Engineering 36 (2009) 597–610 – kap 2.3.1
42. Aalco Metals Ltd, *Technical Information. Accessed from* http://www.aalco.co.uk/datasheets/Aluminium-Alloy_1050-H14_57.ashx. 25.05.2013.
43. Smith Metal. *Sheet Metalwork; Data Sheet*. Acsessed from http://www.smithmetal.com/downloads/1050A.pdf. 03.06.2013
44. , J. E. Hatch, "*Aluminum –Properties and physical metallurgy*", American Society for Metals.1984.

45. *O.G Lademo, forelesning on plastic properties of aluminium, NTNU, 6.september 2012 – kap. 3.2.1*
46. Wikipedia contributors. *Necking.* Acessed from: http://en.wikipedia.org/wiki/Necking_(engineering) 28.02.13 – kap 3.2.2
47. R.Cadell. *Forming Limit Diagrams. Acsessed from* http://www.globalspec.com/reference/70324/203279/chapter-15-forming-limit-diagrams, 01.03.12
48. Coudert, T. "*MatPrePost, Material parameter identification and model visualization*" NTNU. 20.02.2013
49. Matweb. *1050-H14*. Acessed from http://www.matweb.com/search/data sheet.aspx?matguid=b1aa69c0528a40729478403 542a8c94a&ckck=1.2013
50. Astrup AS. *Legeringer, kvaliteter, mekaniske verdier og toleranser*. Acessed from www.astrup.no/asset/1080/1/1080_1.pdf.17.04.2013
51. Simlab. Compressed gas gun. http://www.ntnu.edu/simlab/testing/gasgun, 05.03.13
52. Wikipedia Contributors: *Bar*.http://en.wikipedia.org/wiki/Bar_(unit), Acessed 05.03.12
53. T Børvik, J. Leinumb, J.l Solbergb, O.Hopperstada, M. Langsetha.*Observations on shear plug formation in Weldox 460 E steel plates impacted by blunt-nosed projectiles*. International Journal of Impact Engineering.Volume 25, Issue 6, July 2001, Pages 553–572
54. K. O. Hauge, Forsvarsbygg, mail correspondance. 13.03.13
55. K.Andersen, F. Hernandez, *Numerical Simulations of Steel Plates Subjected to Blast Loading*. NTNU. 2013
56. PhotronUSA. *Photron.* http://www.photron.com/index.php?cmd =product_general&product_id=28&product_name=FASTCAM+SA4. Acessed 01.02.2013
57. Vision Research Inc. *Photron.*http://www.visionresearch.com/Products/High-Speed-Cameras/v1610/) Acessed 05.05.2013.
58. CMV-TECH. *Blast Calc*, http://www.cmv-tech.com/blastcalc.html, Acessed 02.04.2013.
59. Apple inc, *Blast Calc*. https://itunes.apple.com/us/app/blast-calculator/id458990074?mt=8. Acessed 04.06.2013
60. T. Berstad, mail correspondance. 10.04.2013

61. L. Olovsson. Mail correspondance. 10.04.13
62. B. Zakrisson, B.t Wikman, H. Häggblad. *Numerical simulations of blast loads and structural deformation from near-field explosions in air*, International Journal of Impact Engineering.Volume 38, Issue 7, July 2011, Pages 597–612.

Appendices

LS DYNA KEYWORD FOR CHAPTER 3

```
*KEYWORD
*INCLUDE
mesh.k
*CONTROL_TERMINATION
2
*CONTROL_ENERGY
2
*CONTROL_ACCURACY
1,4
*CONTROL_SHELL
 , , , 1
*MAT_107
$     MID       RO        E       PR     BETA      XSI       CP     ALPHA
       1 2700.0000 7.1000+11 0.3000000 0.0000000 0.9000000  899.0000  1.5000-004
$   E0DOT       Tr        Tm       T0     FLAG1     FLAG2
 1.00000-3 293.00000  922.0000 293.00000 0.0000000 1.0000000
$       A         B         N         C         m
 0.97000+8 0.00000+0 0.0000000 0.0140000 1.0000000
$      Q1        C1        Q2        C2
 22.520,1613.1,5.9553,483.84
$      DC        WC
 1.0000000  4.1800+8
$      TC      TAUC
 829.00000 1.0000+20
*MAT_RIGID
$     MID       RO        E       PR
       5 7850.0000 2.1000+11 0.3000000
1, 7, 7


*MAT_RIGID
$     MID       RO        E       PR
       6 7850.0000 2.1000+11 0.3000000
1, 5, 5


*SECTION_SHELL
1, , ,5
$ Plate Thickness
1
*SECTION_SHELL
2, , ,
1
*PART
plate
$Part, Section, Material id
```

```
1,1,1
*PART
fast_bolt
$Part, Section, Material id
2,2,5
*PART
bevegelig_bolt
$Part, Section, Material id
3,2,6
*SET_PART
56
1, 2
*CONTACT_TIED_SHELL_EDGE_TO_SURFACE
1, 3, 3, 3



*CONTACT_TIED_SHELL_EDGE_TO_SURFACE
1, 2, 3, 3



*BOUNDARY_PRESCRIBED_MOTION_RIGID
3, 1, , 10, , , ,
*DEFINE_CURVE
10
0.0,0.0
0.05,2
2,2
*DATABASE_GLSTAT
1e-5
*DATABASE_MATSUM
1e-5
*DATABASE_BINARY_D3PLOT
1e-3, 0
*DATABASE_NODOUT
1e-5
*DATABASE_RCFORC
1e-3
*DATABASE_HISTORY_SHELL_ID
1
*DATABASE_ELOUT
1e-3
*DATABASE_EXTENT_BINARY
,10
*END
```

MATLAB-SCRIPT USED IN CHAPTER 3

```
clc
clear all


nodespecimen=csvread('nodespecimen.txt'); % read node text file for the specimen
nnodespecimen=size(nodespecimen); % number of nodes
nodecyl=csvread('nodetop.txt');% read node text file for the cylinder
nnodecyl=size(nodecyl);% number of nodes


elementspecimen=csvread('elementspecimen.txt');% read element text file for the specimen
nelementspecimen=size(elementspecimen);% number of element


elementtop=csvread('elementtop.txt'); % read element text file for the cylinder
nelementtop=size(elementtop);% number of element


%%%%%%%%%%%%%%%%%%%%%%%%%%%%%%%%%%%%%%%%%%%%%%%%%
%%%%%%%%%%%%%%%%%%%%%%%%%%%%%%%%
disp('ecriture');
%%%%%%%%%%%%%%%%%%%%%%%%%%%%%%%%%%%%%%%%%%%%%%%%%
%%%%%%%%%%%%%%%%%%%%%%%%%%%%%%%%
fich=fopen(['mesh.k'],'w'); % name of the input file
%%%%%%%%%%%%%%%%%%%%%%%%%%%%%%%%%%%%%%%%%%%%%%%%%
%%%%%%%%%%%%%%%%%%%%%%%%%%%%%%%%
fprintf(fich,['*PART\n']);% write the part name and so on
fprintf(fich,['$# title\n']);
fprintf(fich,['top\n']);% the name
fprintf(fich,['$#     pid     secid     mid     eosid     hgid     grav   adpopt     tmid\n']);
fprintf(fich,'%g,%g,%g,%g,%g,%g,%g,%g\n',2,0,0,0,0,0,0,0); % part number (pid), section id (secid),
material id (mid) here secid and mid are not defined...
%%%%%%%%%%%%%%%%%%%%%%%%%%%%%%%%%%%%%%%%%%%%%%%%%
%%%%%%%%%%%%%%%%%%%%%%%%%%%%%%%%
fprintf(fich,['*PART\n']);
fprintf(fich,['$# title\n']);
fprintf(fich,['specimen\n']);
fprintf(fich,['$#     pid     secid     mid     eosid     hgid     grav   adpopt     tmid\n']);
fprintf(fich,'%g,%g,%g,%g,%g,%g,%g,%g\n',1,0,0,0,0,0,0,0);
%%%%%%%%%%%%%%%%%%%%%%%%%%%%%%%%%%%%%%%%%%%%%%%%%
%%%%%%%%%%%%%%%%%%%%%%%%%%%%%%%%
fprintf(fich,['*PART\n']);
fprintf(fich,['$# title\n']);
fprintf(fich,['bottom\n']);
fprintf(fich,['$#     pid     secid     mid     eosid     hgid     grav   adpopt     tmid\n']);
fprintf(fich,'%g,%g,%g,%g,%g,%g,%g,%g\n',3,0,0,0,0,0,0,0);
```

```
%%%%%%%%%%%%%%%%%%%%%%%%%%%%%%%%%%%%%%%%%%%%%%%%%%%%
%%%%%%%%%%%%%%%%%%%%%%%%%%%%%%%%%%
fprintf(fich,['*NODE\n']);% write the node keyword
fprintf(fich,['$#   nid              x              y              z      tc      rc\n']);


for i=1:nnodespecimen(1,1)
fprintf(fich,'%g,%6d,%6d,%6d,%g,%g\n',nodespecimen(i,1),nodespecimen(i,2),nodespecimen(i,3),no
despecimen(i,4)+10,0,0);% write the node number and coordinates + translation of the specimen
end
shift=nnodespecimen(1,1); % a shift in the node numbers is required when going abaqus from LS-
DYNA
for i=1:nnodecyl(1,1)
fprintf(fich,'%g,%6d,%6d,%6d,%g,%g\n',nodecyl(i,1)+shift,nodecyl(i,2),nodecyl(i,3),nodecyl(i,4),0,0)
;% write the node number and coordinates of the 'top' cylinder

end

shift2=shift+nnodecyl(1,1);
for i=1:nnodecyl(1,1)
fprintf(fich,'%g,%6d,%6d,%6d,%g,%g\n',nodecyl(i,1)+shift2,nodecyl(i,2)+150,nodecyl(i,3),nodecyl(i,
4),0,0);% write the node number and coordinates of the 'bottom' cylinder which is just a copy of the
top one

end
%%%%%%%%%%%%%%%%%%%%%%%%%%%%%%%%%%%%%%%%%%%%%%%%%%%%
%%%%%%%%%%%%%%%%%%%%%%%%%%%%%%%%%%
disp('node done');
%%%%%%%%%%%%%%%%%%%%%%%%%%%%%%%%%%%%%%%%%%%%%%%%%%%%
%%%%%%%%%%%%%%%%%%%%%%%%%%%%%%%%%%%%%%%%%%%%%%%%%%%%
%%%%%%%%%%%%%%%%%%%%%%%%%%%%%%%%%%%%%%%%%%%%%%%%
% If solid elements are required just uncomment this part
%fprintf(fich,['*ELEMENT_SOLID\n']);
%fprintf(fich,['$#   eid     pid      n1      n2      n3      n4      n5      n6      n7      n8\n']);
%elementcyl(:,2:9)=elementcyl(:,2:9)+shift;
%for i=1:ncyl(1,1)
%fprintf(fich,'%g,%g,%g,%g,%g,%g,%g,%g,%g,%g\n',elementcyl(i,1),7,elementcyl(i,2),elementcyl(i,
3),elementcyl(i,4),elementcyl(i,5),elementcyl(i,6),elementcyl(i,7),elementcyl(i,8),elementcyl(i,9));
%end
%%%%%%%%%%%%%%%%%%%%%%%%%%%%%%%%%%%%%%%%%%%%%%%%%%%%
%%%%%%%%%%%%%%%%%%%%%%%%%%%%%%%%%%
disp('volume element done');
%
%%%%%%%%%%%%%%%%%%%%%%%%%%%%%%%%%%%%%%%%%%%%%%%%%%%%
%%%%%%%%%%%%%%%%%%%%%%%%%%%%%%%%%%%%%%%%%%%%%%%%%%%%
%%%%%%%%%%%%%%%%%%%%%%%%%%%%%%%%%%%%%%%%%%%%%%%%
fprintf(fich,['*ELEMENT_SHELL\n']); %keyword for shells
fprintf(fich,['$#   eid     pid      n1      n2      n3      n4      n5      n6      n7      n8\n']);
for k=1:nelementspecimen(1,1)
```

```
fprintf(fich,'%g,%g,%g,%g,%g,%g\n',elementspecimen(k,1),1,elementspecimen(k,2),elementspecimen(k,3),elementspecimen(k,4),elementspecimen(k,5));
end
shiftel1 = nelementspecimen(1,1); % the element numbers have to be shifted too.
for k=1:nelementtop(1,1)
fprintf(fich,'%g,%g,%g,%g,%g,%g\n',elementtop(k,1)+shiftel1,2,elementtop(k,2)+shift,elementtop(k,3)+shift,elementtop(k,4)+shift,elementtop(k,5)+shift);

end

shiftel2 = shiftel1 + nelementtop(1,1);
for k=1:nelementtop(1,1)
fprintf(fich,'%g,%g,%g,%g,%g,%g\n',elementtop(k,1)+shiftel2,3,elementtop(k,2)+shift2,elementtop(k,3)+shift2,elementtop(k,4)+shift2,elementtop(k,5)+shift2);

end
%%%%%%%%%%%%%%%%%%%%%%%%%%%%%%%%%%%%%%%%%%%%%%%%%
%%%%%%%%%%%%%%%%%%%%%%%%%%%%%%%%
fprintf(fich,['*END\n']);
disp('shell element done');
fclose(fich);

% that's all :)
```

LS-DYNA KEYWORD FOR CHAPTER 4

```
*KEYWORD
*INCLUDE
plate_1mmesh.k
support1.k
bolt_ekte.k
*CONTROL_TERMINATION
2
*CONTROL_ACCURACY
1,4
*CONTROL_SHELL
 , , , 1
*DEFINE_CURVE
10
0.0,0.0
0.006,3e5
0.2, 0.0
*SET_SHELL_GENERAL
11
Part, 1
*LOAD_SHELL_SET
11, 10
*MAT_107
$     MID       RO        E        PR      BETA       XSI        CP     ALPHA
         1 2700.0000 7.1000+11 0.3000000 0.0000000 0.9000000  452.0000  1.2000-5
$   E0DOT        Tr        Tm        T0     FLAG1     FLAG2
 1.00000-3 293.00000 922.00000 293.00000 0.0000000 1.0000000
$        A         B         N         C         m
 1.1000+8 1.5000+80 0,0014000 0.0000000 1.0000000
$       Q1        C1        Q2        C2
  00000000   0000000 000000 000000
$       DC        WC
 1.0000000  7.3400+8
$       TC      TAUC
 829.00000 1.0000+20
*SECTION_SHELL
1, , ,5
$ Plate Thickness
1e-3
*PART
exposed_loaded_area
$Part, Section, Material id
1,1,1
*PART
unexposed_unloaded_area
$Part, Section, Material id
```

```
2,1,1
*MAT_RIGID
$     MID        RO         E        PR
         5 7850.0000 2.1000+11 0.3000000
1, 7, 7

*SECTION_SOLID
5
*PART
clamping_plate
$Part, Section, Material id
6,5,5
*PART
support_plate
$Part, Section, Material id
7, 5, 5
*PART
$# title
Bolter
$#     pid     secid       mid     eosid      hgid      grav    adpopt      tmid
         5         5         5         0         0         0         0         0
*SET_PART
76
7, 6
*CONTACT_AUTOMATIC_SURFACE_TO_SURFACE
2, 76, 3, 2


*DEFINE_BOX
23, -1e-4, 1e-4, 0, 0.2, -1, 1
*DEFINE_BOX
24, 0, 0.2, -1e-4, 1e-4, -1, 1
*SET_NODE_GENERAL
30
Part, 2
*SET_NODE_GENERAL
33
Box, 23
*SET_NODE_GENERAL
34
Box, 24
*BOUNDARY_SPC_SET
$SYMMETRY
33, , 1, 0, 0, 0, 1, 1
$SYMMETRY
34, , 0, 1, 0, 1, 0, 1
*DATABASE_GLSTAT
1e-5
```

```
*DATABASE_MATSUM
1e-5
*DATABASE_BINARY_D3PLOT
1e-3, 0
*DATABASE_NODOUT
1e-5
*DATABASE_HISTORY_NODE
931
*END
```

MATLAB SCRIPT USED IN CHAPTER 5

```
%
%   Master Thesis "Blast loaded aluminums plates"
%   By Hilde Eide and Emil Melby
%   2.order Butterworth low pass filter – 100 Hz cut off frequency
%
close all
clear all
clc
%
%   Pressure Histories
%
MaxP = 350;
MinP = -50;
set(0,'defaulttextinterpreter','latex')
set(0,'DefaultAxesFontSize', 25)
%
%   Position # 1
%
load bar10smalltest2.txt
load bar10smalltest2F.txt
S2(:,1) = bar10smalltest2(:,1);
S2(:,2) = bar10smalltest2(:,2);
S2F(:,1) = bar10smalltest2F(:,1);
S2F(:,2) = bar10smalltest2F(:,2);
cutF = 100;                         % Cutoff frequency [Hz]
samplR = 500000;                    % Sampling rate [Hz]
cutN = cutF*2/samplR;               % Normalized cutoff frequency [-]
[b,a]=butter(2,cutN);
filt=filter(b,a,S2);
h=plot(S2(:,1),S2(:,2),'b:',filt(:,1),filt(:,2),'k');
grid on;xlabel('Time t (s)');title('10 Bar small chamber test 2');
ylabel('Pressure P (kPa)');axis([0 0.5 MinP MaxP]);
test=legend('Raw data','Filtered data');
set(h(1),'linewidth',0.5)
set(h(2),'linewidth',2)
A=trapz(filt(:,1),filt(:,2))
B=trapz(S2(:,1),S2(:,2))
C=trapz(S2F(:,1),S2F(:,2))
figure(2);plot(S2(:,1),S2(:,2),'b',S2F(:,1),S2F(:,2),'k');
grid on;xlabel('Time t (s)');title('10 Bar small chamber test 2');
ylabel('Pressure P (kPa)');axis([0 0.5 MinP MaxP]);
legend('Raw data','Filtered data');
```

LS-DYNA KEYWORD FOR CHAPTER 6

*KEYWORD
*INCLUDE
plate.k
support.k
rammeny.k
*CONTROL_TERMINATION
0.2
*CONTROL_ENERGY
2
*CONTROL_ACCURACY
1,4
*CONTROL_SHELL
, , , 1
*DEFINE_CURVE

10	11	12	13	14
0,0	0,0	0,0	0,0	0,0
0.001,0.0016	0.002,0.0024	0.0008,0	0.001,0	0.001,0
0.0036,0.0033	0.0036,0.0025	0.0036,0	0.0036,0.0017	0.0036,-0.0032
0.0067,0.0045	0.0067,0.0033	0.0067,0	0.0067,0.0024	0.0067,-0.0016
0.0098,0.0050	0.0098,0.0028	0.0098,0.0028	0.0098,0.0016	0.0098,0
0.0128,0.0046	0.0128,0.0059	0.0128,0.0027	0.0128,0.0017	0.0128,0
0.0157,0.0054	0.0157,0.0060	0.0157,0.0028	0.0157,0.0017	0.0157,0
0.0187,50	0.0187,8.6616	0.0187,7.5006	0.0187,7.8908	0.0187,4.6208
0.0217,114.0203	0.0217,53.2083	0.0217,10.3857	0.0217,-8.8409	0.0217,-6.5169
0.0247,133.2615	0.0247,49.4738	0.0247,2.1770	0.0247,-17.4034	0.0247,-9.3362
0.0277,109.1675	0.0277,26.5830	0.0277,-9.0076	0.0277,-22.1842	0.0277,-10.6939
0.0307,33.5172	0.0307,7.4665	0.0307,-5.2230	0.0307,-13.6811	0.0307,-6.5859
0.0337,5.6375	0.0337,-0.7788	0.0337,-7.1853	0.0337,-16.7413	0.0337,-6.2032
0.0367,27.9308	0.0367,10.9967	0.0367,1.6823	0.0367,-8.8225	0.0367,-4.8726
0.0397,25.3776	0.0397,11.8391	0.0397,5.9965	0.0397,-1.6985	0.0397,-1.3027
0.0427,23.3259	0.0427,24.1934	0.0427,19.4164	0.0427,7.4277	0.0427,-2.5323
0.0457,16.2381	0.0457,15.5141	0.0457,12.9485	0.0457,4.7436	0.0457,-2.8389
0.0487,11.7556	0.0487,9.6782	0.0487,9.8508	0.0487,9.6485	0.0487,2.7707
0.0517,16.9412	0.0517,17.1577	0.0517,18.2780	0.0517,16.0553	0.0517,2.5415
0.0547,19.7674	0.0547,17.0760	0.0547,12.4936	0.0547,8.5822	0.0547,4.4555
0.0577,14.0705	0.0577,12.9654	0.0577,8.6997	0.0577,5.4345	0.0577,3.6214
0.0607,4.5261	0.0607,9.9902	0.0607,12.4698	0.0607,7.6781	0.0607,4.3879
0.0637,0.1064	0.0637,6.8116	0.0637,10.3204	0.0637,11.7550	0.0637,6.0777
0.0667,-4.0821	0.0667,0.2990	0.0667,4.6172	0.0667,10.9903	0.0667,9.7516
0.0697,-5.0993	0.0697,1.4614	0.0697,6.2865	0.0697,9.1857	0.0697,10.8636
0.0727,-3.6540	0.0727,7.8301	0.0727,12.1870	0.0727,9.3110	0.0727,5.4890
0.0757,1.0074	0.0757,5.4481	0.0757,6.2863	0.0757,5.9244	0.0757,3.6933
0.0787,2.9454	0.0787,2.5380	0.0787,0.9405	0.0787,0.6694	0.0787,1.6830
0.0817,46.4049	0.0817,19.7504	0.0817,4.6313	0.0817,-6.6515	0.0817,-2.9535
0.0847,146.1006	0.0847,61.0720	0.0847,7.9186	0.0847,-16.1518	0.0847,-12.8375
0.0877,161.1239	0.0877,42.6422	0.0877,2.6678	0.0877,-15.7175	0.0877,-13.2412
0.0907,118.6925	0.0907,11.6000	0.0907,-2.8455	0.0907,-13.5471	0.0907,-9.7246
0.0937,81.8672	0.0937,6.4985	0.0937,-5.9396	0.0937,-14.2920	0.0937,-9.3663

0.0967,89.8768	0.0967,1.2977	0.0967,-6.3042	0.0967,-15.2646	0.0967,-9.3562
0.0997,105.5369	0.0997,2.0189	0.0997,-5.6746	0.0997,-15.6624	0.0997,-7.5264
0.1027,97.6024	0.1027,13.9233	0.1027,-4.5882	0.1027,-14.4234	0.1027,-8.0311
0.1057,75.0786	0.1057,14.1442	0.1057,-5.8358	0.1057,-15.8818	0.1057,-9.0650
0.1087,74.3438	0.1087,7.4331	0.1087,-6.3603	0.1087,-15.2358	0.1087,-8.9946
0.1117,63.1158	0.1117,4.7099	0.1117,-6.6951	0.1117,-15.5861	0.1117,-9.9943
0.1147,62.0628	0.1147,18.3189	0.1147,-3.5785	0.1147,-13.5130	0.1147,-7.4429
0.1177,59.2885	0.1177,17.6956	0.1177,-0.7719	0.1177,-10.5320	0.1177,-5.8140
0.1207,63.8707	0.1207,14.5595	0.1207,1.3542	0.1207,-11.7661	0.1207,-8.0644
0.1237,70.0260	0.1237,16.2218	0.1237,0.4703	0.1237,-12.1977	0.1237,-7.1928
0.1267,72.6726	0.1267,18.8302	0.1267,-1.6299	0.1267,-12.5533	0.1267,-7.6605
0.1297,83.1482	0.1297,13.2009	0.1297,0.7014	0.1297,-13.4897	0.1297,-6.9964
0.1327,73.3126	0.1327,10.8360	0.1327,-2.5891	0.1327,-11.7888	0.1327,-7.0838
0.1357,72.0604	0.1357,17.0103	0.1357,-3.8355	0.1357,-13.1761	0.1357,-6.8120
0.1387,54.4568	0.1387,7.1249	0.1387,-2.7633	0.1387,-12.2507	0.1387,-7.3836
0.1417,61.1464	0.1417,13.5887	0.1417,-2.8997	0.1417,-11.7894	0.1417,-6.6576
0.1447,57.8791	0.1447,15.9293	0.1447,-3.6185	0.1447,-11.9661	0.1447,-7.1176
0.1477,53.9841	0.1477,11.1687	0.1477,-3.1189	0.1477,-11.4045	0.1477,-7.7113
0.1507,51.1530	0.1507,11.0739	0.1507,-3.1851	0.1507,-11.7682	0.1507,-8.7344
0.1537,52.1377	0.1537,13.4976	0.1537,-1.7076	0.1537,-11.0818	0.1537,-6.6309
0.1567,42.1077	0.1567,14.4037	0.1567,-0.4154	0.1567,-9.3806	0.1567,-5.0203
0.1597,36.9869	0.1597,10.0633	0.1597,0.4963	0.1597,-8.4055	0.1597,-5.4226
0.1627,55.6078	0.1627,17.3686	0.1627,-0.8879	0.1627,-11.0468	0.1627,-6.6460
0.1657,53.6871	0.1657,10.8862	0.1657,-3.3379	0.1657,-12.0903	0.1657,-6.5796
0.1687,46.5711	0.1687,12.6150	0.1687,-2.1922	0.1687,-9.5651	0.1687,-5.4961
0.1717,48.1892	0.1717,12.8257	0.1717,-0.8701	0.1717,-9.9352	0.1717,-6.7557
0.1747,48.2051	0.1747,14.5270	0.1747,0.0483	0.1747,-9.1934	0.1747,-3.9527
0.1777,50.8397	0.1777,13.0553	0.1777,-1.7760	0.1777,-9.5602	0.1777,-5.3352
0.1807,50.5231	0.1807,10.5774	0.1807,-3.2197	0.1807,-9.7678	0.1807,-5.2811
0.1837,47.3453	0.1837,14.7478	0.1837,-0.1152	0.1837,-7.9799	0.1837,-5.1349
0.1867,39.8701	0.1867,20.2680	0.1867,6.8951	0.1867,-7.1193	0.1867,-5.7773
0.1897,37.9744	0.1897,14.2276	0.1897,4.1070	0.1897,-6.8869	0.1897,-5.7594
0.1927,35.1817	0.1927,5.4348	0.1927,-2.5628	0.1927,-8.3857	0.1927,-4.4006
0.1957,39.8776	0.1957,6.6420	0.1957,-2.8577	0.1957,-9.3044	0.1957,-3.9623
0.1987,39.7847	0.1987,10.8536	0.1987,-1.8430	0.1987,-8.0939	0.1987,-4.1817
0.2017,39.3836	0.2017,8.3861	0.2017,-1.1993	0.2017,-7.5296	0.2017,-4.6282
0.2047,41.8596	0.2047,10.8668	0.2047,0.5835	0.2047,-6.5616	0.2047,-4.8777
0.2077,34.0014	0.2077,8.5085	0.2077,-0.5415	0.2077,-6.4713	0.2077,-4.2523
0.2107,30.6886	0.2107,7.4251	0.2107,-1.8175	0.2107,-7.0766	0.2107,-4.2475
0.2137,28.4868	0.2137,9.4685	0.2137,-1.7860	0.2137,-7.9328	0.2137,-3.0154
0.2167,30.4526	0.2167,11.4586	0.2167,-1.6913	0.2167,-7.1775	0.2167,-3.0891
0.2197,31.0997	0.2197,8.8443	0.2197,-1.8451	0.2197,-6.6494	0.2197,-4.4659
0.2227,38.1731	0.2227,9.5351	0.2227,-0.9952	0.2227,-6.6150	0.2227,-3.8012
0.2257,35.1937	0.2257,10.1464	0.2257,0.6779	0.2257,-5.9962	0.2257,-3.3756
0.2287,32.6371	0.2287,11.5675	0.2287,-0.1457	0.2287,-6.0667	0.2287,-3.8627
0.2317,30.5722	0.2317,9.6622	0.2317,-0.2333	0.2317,-5.8290	0.2317,-4.2179
0.2347,30.7209	0.2347,9.3708	0.2347,-0.0738	0.2347,-6.0168	0.2347,-3.2672
0.2377,30.1170	0.2377,5.7996	0.2377,-0.7033	0.2377,-6.2253	0.2377,-3.1618
0.2407,26.9845	0.2407,6.3477	0.2407,-0.9460	0.2407,-5.1917	0.2407,-3.1103
0.2437,30.1336	0.2437,7.9361	0.2437,-1.0774	0.2437,-5.2366	0.2437,-3.2065
0.2467,26.9183	0.2467,10.8121	0.2467,-0.2979	0.2467,-5.1060	0.2467,-2.9004
0.2497,23.0310	0.2497,7.4311	0.2497,-0.1570	0.2497,-4.7598	0.2497,-2.9956
0.2527,21.2263	0.2527,6.4891	0.2527,0.7216	0.2527,-4.3966	0.2527,-2.7715
0.2557,21.1840	0.2557,6.6972	0.2557,0.6018	0.2557,-4.2294	0.2557,-2.8774
0.2587,19.4401	0.2587,3.4649	0.2587,-1.0714	0.2587,-4.8637	0.2587,-2.5142

0.2617,20.1632	0.2617,4.0687	0.2617,-1.2455	0.2617,-5.3333	0.2617,-2.7426
0.2647,16.0188	0.2647,5.0284	0.2647,-0.7009	0.2647,-4.9062	0.2647,-2.4708
0.2677,16.1933	0.2677,4.9251	0.2677,-0.3811	0.2677,-4.2993	0.2677,-2.5997
0.2707,15.5047	0.2707,4.3871	0.2707,-0.9104	0.2707,-4.2272	0.2707,-2.0379
0.2737,12.1573	0.2737,3.0551	0.2737,-0.8896	0.2737,-4.2992	0.2737,-2.3782
0.2767,12.2963	0.2767,2.5261	0.2767,-0.9950	0.2767,-3.9485	0.2767,-2.2937
0.2797,9.8520	0.2797,2.8550	0.2797,-0.9670	0.2797,-4.2542	0.2797,-2.2769
0.2827,8.1579	0.2827,3.5133	0.2827,-0.5348	0.2827,-4.1600	0.2827,-2.2476
0.2857,12.4388	0.2857,5.4687	0.2857,-0.1905	0.2857,-4.0290	0.2857,-1.9032
0.2887,12.0857	0.2887,3.3404	0.2887,-0.6700	0.2887,-3.8153	0.2887,-2.2755
0.2917,8.4660	0.2917,4.9268	0.2917,0.2935	0.2917,-3.6140	0.2917,-1.5985
0.2947,8.2740	0.2947,3.5525	0.2947,-0.1442	0.2947,-3.2837	0.2947,-1.8303
0.3,0	0.3,0	0.3,0	0.3,0	0.3,0

```
*set_shell_general
1
PART,1
*set_shell_general
2
PART,2
*set_shell_general
3
PART,3
*set_shell_general
4
PART,4
*set_shell_general
5
PART,5
$
$ ***** Load set x with load curve x *****
$
*load_shell_set
1,10,1000
*load_shell_set
2,11,1000
*load_shell_set
3,12,1000
*load_shell_set
4,13,1000
*load_shell_set
5,14,1000
*MAT_107
$     MID       RO        E       PR     BETA      XSI       CP     ALPHA
        1 2700.0000 7.1000+11 0.3000000 0.0000000 0.9000000  899.0000  1.5000-004
$   E0DOT        Tr        Tm       T0     FLAG1     FLAG2
 1.00000-3 293.00000  918.0000 293.00000 0.0000000 1.0000000
$         A         B         N         C         m
```

```
 0.97000+8 0.00000+0 0.0000000 0.0140000 1.0000000
$       Q1        C1        Q2        C2
 22.520,1613.1,5.9553,483.84
$       DC        WC
 1.0000000  5.4140+8
$       TC      TAUC
 829.00000 1.0000+20
*SECTION_SHELL
1, , ,5
$ Plate Thickness
1e-3
*PART
plate1
1,1,1
*PART
plate2
2,1,1
*PART
plate3
3,1,1
*PART
plate4
4,1,1
*PART
plate5
5,1,1
*PART
plate6
6,1,1
*MAT_RIGID
$      MID        RO         E        PR
         5 7850.0000 2.1000+11 0.3000000
1, 7, 7

*SECTION_SOLID
5
*PART
clamping_plate
$Part, Section, Material id
9,5,5
*PART
support_plate
$Part, Section, Material id
10, 5, 5
*PART
ramme
14, 5, 5
*SET_PART
```

```
76
10, 9
*CONTACT_AUTOMATIC_SURFACE_TO_SURFACE
6, 76, 3, 2


*CONTACT_AUTOMATIC_NODES_TO_SURFACE
6, 14, 3, 3


*DATABASE_GLSTAT
1e-5
*DATABASE_MATSUM
1e-5
*DATABASE_BINARY_D3PLOT
1e-3, 0
*DATABASE_NODOUT
1e-5
*DATABASE_HISTORY_NODE
9
*END
```

IMPETUS KEYWORD FOR CHAPTER 7

```
*UNIT_SYSTEM
SI
#*INCLUDE
#node.k
*PARAMETER
Lx=0.4          #Plate width
Ly=0.4          #Plate height
Pt=0.001        #Plate thickness
Std=0.3         #Standoff
Bd=0.052        #Diameter barrel
*GEOMETRY_BOX
10
-0.05,-0.21,-0.21,0.05,0.21,-0.1999
*SET_NODE
10,10
*BC_MOTION
NS,10,XYZ
*GEOMETRY_BOX
20
-0.05,-0.21,0.1999,0.05,0.21,0.21
*SET_NODE
20,20
*BC_MOTION
NS,20,XYZ
*GEOMETRY_BOX
30
-0.05,-0.21,-0.1999,0.05,-0.1999,0.1999
*SET_NODE
30,30
*BC_MOTION
NS,30,XYZ
*GEOMETRY_BOX
40
-0.05,0.1999,-0.1999,0.05,0.21,0.1999
*SET_NODE
40,40
*BC_MOTION
NS,40,XYZ
*COMPONENT_BOX
"PLATE"
1,1,1,30,30,0
0,-0.2,-0.2,0.001,0.2,0.2
*PART
1,1
2..8,2
```

```
*OUTPUT_NODE
N,962
*OUTPUT
0.000002,0.000002
*MAT_JC
1,2700,71e9,0.3,1
0.97e8,0.8e8,0.36,0.014,1,293,918
899,0.9
*PROP_DAMAGE_CL
1,1
4.16e8
*MAT_RIGID
2,7850
*SET_PART
1
1
*GEOMETRY_SPHERE
"CHARGE GEOMETRY"
1,0
-1.9,0,0,0.1022544
*CONTACT
1
ALL,1,ALL,2,0.4,,0,0.003
2
*GEOMETRY_BOX
"GLOBAL GEOMETRY"
2,0,
-3,-1,-1,1,1,1
*PBLAST
ALL,0,1,0,tnt,500000,
0
2,0,1,-1.9,0,0,0,0.1
*GPU
1,1,1
*TIME
0.002
*CHANGE_P-ORDER
ALL,0,3
*END
```

LS-DYNA KEYWORD FOR CHAPTER 7

```
*KEYWORD
*INCLUDE
platehel.k
*CONTROL_TERMINATION
0.01
*CONTROL_ENERGY
2
*CONTROL_ACCURACY
1,4
*CONTROL_SHELL
 , , , 1
*DEFINE_CURVE
1
0,0
0.001,1
*DEFINE_CURVE
2
0,0
1,0
*LOAD_BLAST
7.3,0,0,1.9

*set_shell_general
1
PART,1
*load_shell_set
1,-2
*MAT_107
$     MID       RO        E        PR      BETA       XSI        CP     ALPHA
         1 2700.0000 7.1000+11 0.3000000 0.0000000 0.9000000  899.0000  1.5000-004
$    E0DOT        Tr        Tm        T0     FLAG1     FLAG2
 1.00000-3 293.00000  918.0000 293.00000 0.0000000 1.0000000
$         A         B         N         C         m
 0.97000+8 0.00000+0 0.0000000 0.0140000 1.0000000
$        Q1        C1        Q2        C2
 22.520,1613.1,5.9553,483.84
$        DC        WC
 1.0000000  5.4140+8
$        TC      TAUC
 829.00000 1.0000+20
*SECTION_SHELL
1, , ,5
$ Plate Thickness
1e-3
*PART
```

```
exposed_loaded_area
$Part, Section, Material id
1,1,1
*DATABASE_SECFORC
0.4e-5
*DATABASE_NODOUT
0.4e-5
*DATABASE_ELOUT
0.4e-5
*DATABASE_GLSTAT
0.4e-5
*DATABASE_MATSUM
0.0001
*DATABASE_RCFORC
0.0001
*DATABASE_BINARY_D3PLOT
0.000025,0
*END
```